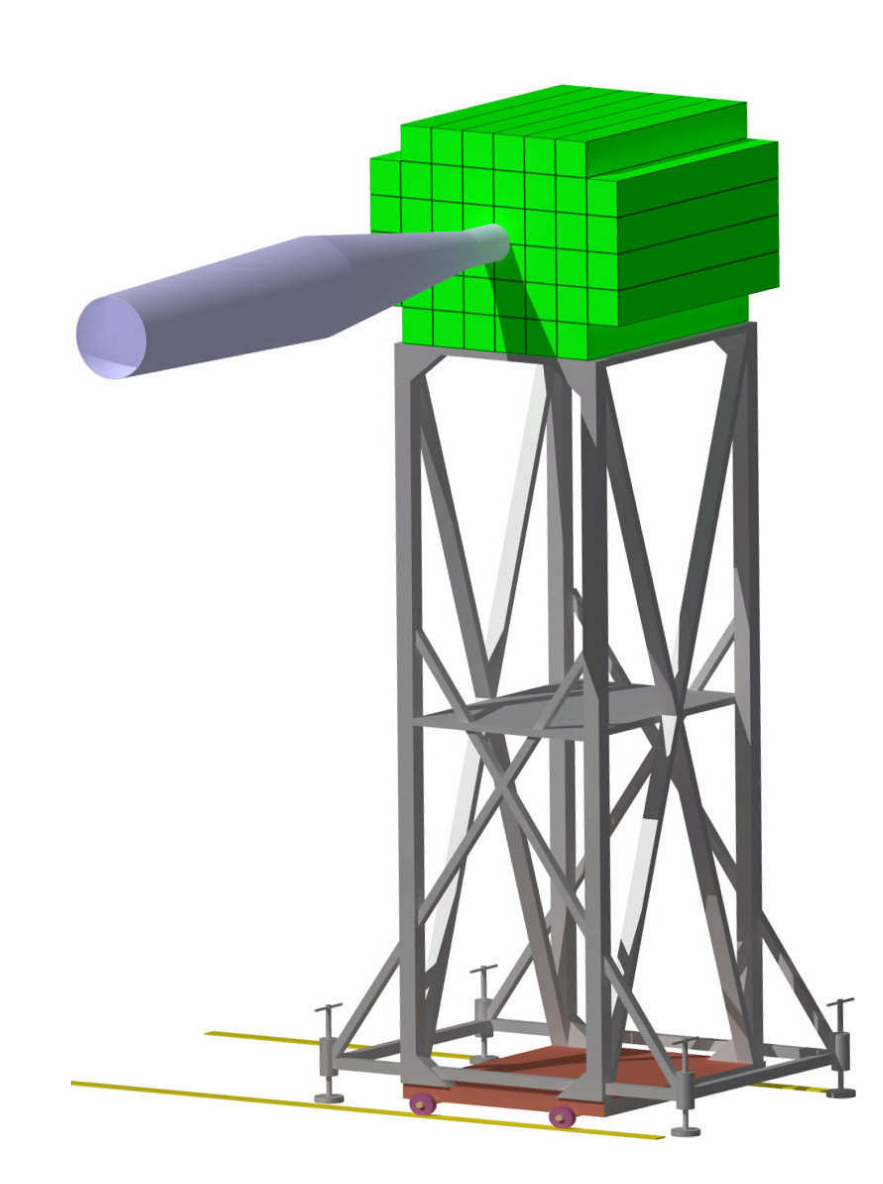


Technical Design Report for the CBM Experiment

Projectile spectator detector (PSD)

The CBM Collaboration



July 2015

CBM home page: http://www.fair-center.eu/for-users/experiments/cbm.html Acknowledgements We acknowledge support by the Bundesministerium für Bildung und Forschung (BMBF), Germany, the GSI Helmholtzzentrum für Schwerionenforschung GmbH, Germany, the Helmholtz Graduate School

HIRe for FAIR, the Helmholtz Research School H-QM, the Technische Universität Darmstadt, Germany, the Institute for Nuclear Research of Russian Academy of Science (INR), Moscow, Russia, the State Atomic Energy Corporation of Russia (ROSATOM), the Nuclear Physics Institute, Academy of Sciences of the Czech Republic, Řež, Czech Republic, and the Ministery of Education, Youth and Sports of Czech

Republic (MEYS).

TECHNICAL DESIGN REPORT FOR THE CBM EXPERIMENT





July 21, 2015

Projectile spectator detector (PSD)

J. Bielcik⁴, T. Galatyuk², M. Golubeva³, F. Guber³, A. Ivashkin³, W. Koenig¹, A. Kugler⁵, A. Kurepin³, V. Kushpil⁵, A. Maevskaya³, V. Mikhaylov⁴, J. Pietraszko¹, V. Petráček⁴, O. Petukhov³, S. Seddiki¹, A. Sadovsky³, I. Selyuzhenkov¹, A. Senger¹, O. Svoboda⁵, P. Tlustý⁵, E. Usenko³

- ¹ GSI Helmholtz Center for Heavy Ion Research GmbH, Darmstadt, Germany
- ² Institut für Kernphysik, Technische Universität Darmstadt, Darmstadt, Germany
- ³ Institute for Nuclear Research of Russian Academy of Science (INR), Moscow, Russia
- ⁴ Czech Technical University (CTU), Prague, Czech Republic
- ⁵ Nuclear Physics Institute, Academy of Sciences of the Czech Republic, Řež, Czech Republic

Contents

1	Executive summary			3		
2 Introduction						
3	CBN	CBM experiment at FAIR				
	3.1	CBM 1	physics program	5		
	3.2	CBM o	detector subsystems	7		
		3.2.1	Dipole magnet	7		
		3.2.2	Micro-vertex detector	7		
		3.2.3	Silicon tracking system	8		
		3.2.4	Ring imaging Cherenkov detector	8		
		3.2.5	Transition radiation detector	8		
		3.2.6	Time of Flight detector	9		
		3.2.7	Projectile spectator detector	9		
		3.2.8	Muon chamber system	9		
		3.2.9	Online data processing	9		
4	Proj	ectile s _l	pectator detector (PSD)	11		
	4.1	Design	requirements	11		
	4.2	Detect	or concept	11		
5	PSD	perfor	mance	13		
	5.1	Heavy	-ion collision modeling	13		
	5.2	CBM o	detector geometry modeling	13		
	5.3	Collisi	on fragment detection	16		
	5.4	Collisi	on centrality determination	18		
	5.5	Reaction	on plane reconstruction	21		
		5.5.1	Event plane correction for detector non-uniformity	22		
		5.5.2	Event plane resolution	24		
		5.5.3	Comparison with other CBM detector subsystems	26		
		5.5.4	Elliptic flow performance	26		
6	PSD	compo	nents	29		
	6.1	Modul	e structure	29		

		6.1.1	Mechanical design	30
		6.1.2	Scintillator tiles, wave-length shifting fibers, and lead plates	31
		6.1.3	Light readout with micropixel avalanche photodiodes	32
	6.2	Reado	ut electronics	34
		6.2.1	Amplifier	34
		6.2.2	Charge digitization	35
		6.2.3	Time-to-digital converter	36
	6.3	Energy	calibration techniques	37
		6.3.1	Radioactive source	37
		6.3.2	LED light	37
		6.3.3	Cosmic muons	37
		6.3.4	Secondary decay muons	40
	6.4	Contro	and cooling systems	41
	6.5	Mecha	nical support	43
7	PSD	compo	nents R&D	44
	7.1	Modul	e prototype tests	44
		7.1.1	Small module response	44
		7.1.2	Supermodule response to high energy pions	47
		7.1.3	Supermodule response to low energy pions	52
		7.1.4	Large module response to low energy protons	52
	7.2	Perform	mance of the NA61 calorimeter	57
	7.3	Test of	avalanche diodes	61
		7.3.1	Radiation induced degradation of micropixel avalanche photodiodes	64
	7.4	Detect	or radiation hardness	65
8	Part	icipatin	ng institutes	67

1 Executive summary

The technical design report describes the main requirements, detector layout, and expected performance of the Projectile Spectator Detector (PSD) for the CBM experiment at the future FAIR facility in Darmstadt, Germany. The main purpose of the PSD is to provide an experimental measurement of a heavy-ion collision centrality and orientation of its symmetry plane. Precise event-by-event estimate of these basic observables is crucial for many physics phenomena studies to be performed by the CBM Collaboration.

The PSD is a compensating lead-scintillator calorimeter designed to measure the energy distribution of the projectile nuclei fragments (spectators) and forward going particles produced close to the beam rapidity. The main design requirements of the PSD are (i) forward rapidity coverage and sufficient energy resolution to allow for precise collision centrality determination and consequently of the number of participating nucleons and (ii) granularity in the plane transverse to the beam direction which is needed for the collision symmetry plane reconstruction. The proposed 44 module design of the PSD covers large transverse area around the beam spot position such that most of the projectile spectator fragments deposit their energy in the PSD. The elongated transverse geometry of the PSD in horizontal direction takes into account the deflection of the fragments by the magnetic field of the CBM Dipole magnet.

A lead-scintillator prototype of the PSD module with scintillator light readout by micropixel avalanche photodiodes and the PSD front-end electronics were tested with the proton and pion beams and cosmic muon rays. Radiation hardness and possible degradation of the PSD were studied with the FLUKA simulation of the CBM detector geometry.

A sample of simulated heavy-ion collisions with realistic modeling of nuclei fragment production, directed and elliptic flow of produced particles transported through the GEANT Monte-Carlo of the CBM detector geometry has been used to demonstrate the desired performance of the PSD. By grouping the PSD modules into subevents according to their radial position in the transverse plane, we showed that the PSD can be used standalone for the centrality determination. Depending on the collision energy, the PSD has a comparable impact parameter resolution to that of the CBM silicon tracking system (STS). Thus, the PSD provides an independent method in the CBM experiment of the centrality determination with spectator multiplicity. When used in a combination with the STS, the PSD helps to improve the overall centrality determination in the centrality range of 0-40% and allows for centrality determination in narrow centrality classes with a width of at least 5%.

The PSD event plane resolution varies in the range of 30-40 degrees depending on the distance from the target and the collision energy. With the proposed elongated geometry, and after correction for the detector azimuthal non-uniformity, the resolution of the PSD event plane shows negligible variation with the field strength of the CBM magnet. We compared the PSD event plane resolution with that of STS and an alternative detector setup at forward rapidity such as a forward time of flight (TOF) detector. We concluded that the PSD has significantly better event plane resolution than both STS and forward TOF detector configurations.

We also presented results from the complete data driven analysis (only using information reconstructed by the CBM sub-detectors) of the proton elliptic flow coefficient, v_2 , in Au+Au collisions at $E_b = 10$ AGeV simulated with the UrQMD model. Based on these results we projected the PSD performance for flow measurements of other particle species such as strange and multi-strange hyperons Λ and Ω^- which are included in the CBM physics program. According to the projections, by using the PSD detector for the event plane determination, the v_2 of Λ s and protons can be measured with a precision of better than 1% in the transverse momentum range between $p_T = 0.5 - 2$ GeV/c after a few months of CBM experiment operation at 100 kHz interaction rate.

2 Introduction

Significant experimental and theoretical effort is devoted to the exploration of the phase diagram of strongly interacting QCD matter. The evolution of the early universe a few microseconds after the big bang is governed by the properties of matter at a very high temperature and close to zero net-baryon density. At large net-baryon density (or baryon chemical potential, μ_B) and lower temperature, the QCD phase diagram is expected to have a rich structure (see Fig. 1(left)) which includes a critical point, a first order phase transition from hadronic to partonic (or quarkyonic) degrees of freedom, and transition from the hadronic matter to the phase where chiral symmetry is restored.

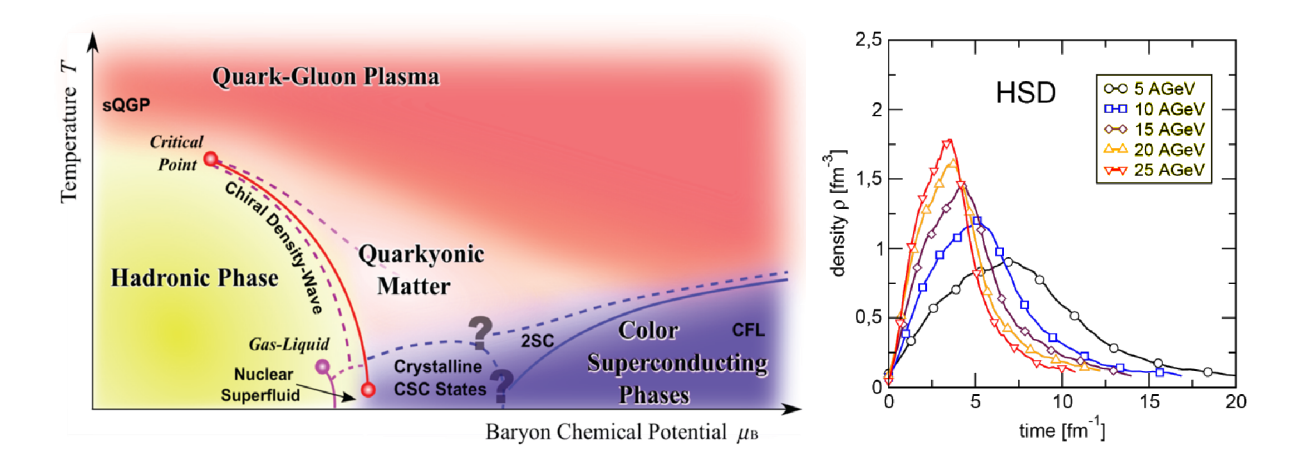


Fig. 1: (left) Phase diagram of the QCD matter depicted in a space of temperature T and baryon chemical potential μ_B (sketch taken from [1]). (right) The HSD transport model calculations of the baryon density as a function of elapsed time for central Au+Au collisions in the beam energy range $E_b = 5 - 25$ GeV (figure taken from [2]).

Different regions of the QCD phase diagram can be explored experimentally with relativistic nucleusnucleus collisions. At the LHC and top RHIC energies, the QCD phase diagram is probed at temperature and net-baryon density typical for the matter of the early universe. The region of high net-baryon density can be accessed with collisions at the center of mass energy $\sqrt{s_{\rm NN}}$ in the range from a few GeV up to several tens of a GeV. Transport model calculations for central Au+Au collisions [2] shows that a very high density can be already reached at a beam energy of about 5 AGeV (see Fig. 1(right)).

Several experimental programs are focused on exploration of this collision energy range. The RHIC beam energy scan program covers the energy range of $\sqrt{s_{\rm NN}} \sim 7-40$ GeV. However, due to a rapid decrease of luminosity with decreasing beam energy, the experimental results from RHIC at low collision energy around $\sqrt{s_{\rm NN}} = 7$ GeV (which corresponds to $E_b \sim 30$ AGeV for a fixed target experiment) have limited statistical precision [3]. The data precision of the NA61 experiment (upgraded NA49 detector) at the CERN-SPS is also limited due to the slow response of the Time-Projection Chamber [4].

3 CBM experiment at FAIR

The future Facility for Antiproton and Ion Research (FAIR) in Darmstadt, Germany [5] is designed to provide a high-intensity heavy-ion beams with SIS100/SIS300 accelerator ring (see Fig. 2). FAIR will

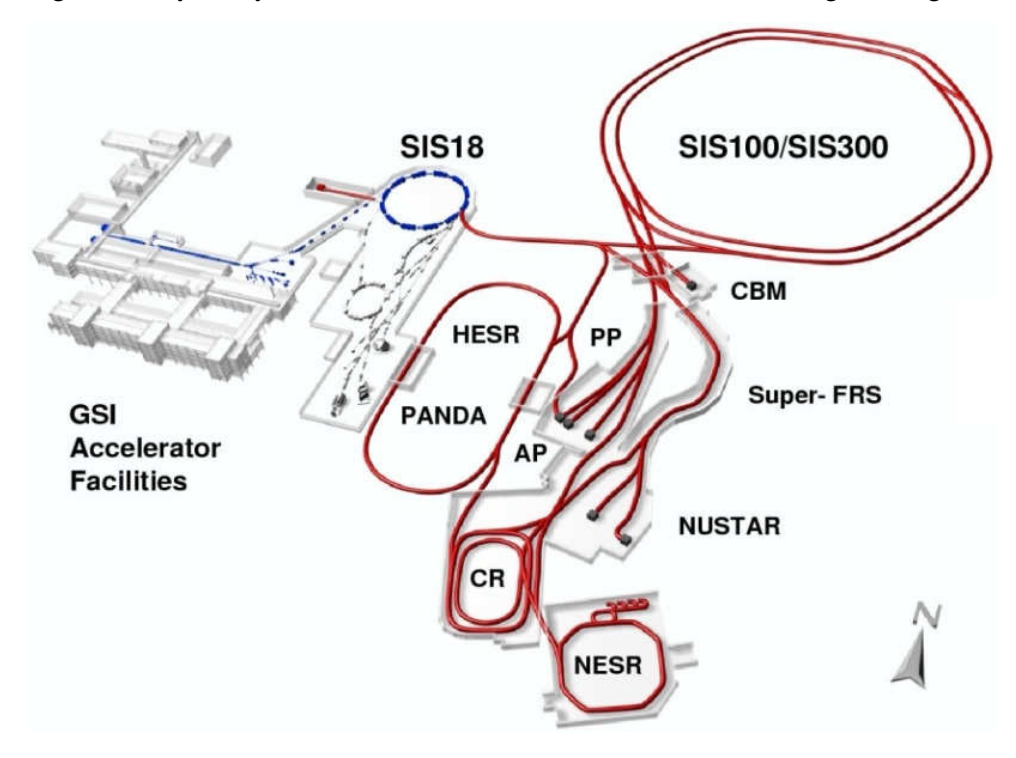


Fig. 2: Layout of the future Facility for Antiproton and Ion Research (FAIR).

allow for unique research opportunities in the fields of nuclear, hadron, atomic and plasma physics. The Compressed Baryonic Matter (CBM) experiment at FAIR is designed to work in a high luminosity environment and will allow for precision measurements in the collision energy range of $\sqrt{s_{\rm NN}} \sim 4-7$ GeV and multi-differential analysis of many physics observables including the yield and correlation of particles with very low production cross section.

Operation of the CBM experiment will start with primary beams delivered by the SIS100 synchrotron which is capable of accelerating proton beam up to $E_b \approx 29$ GeV, gold nuclei up to $E_b \approx 11$ AGeV, and nuclei with Z/A = 0.5 up to $E_b \approx 14$ AGeV. At the latter stage the operation will continue with the beams provided by the SIS300 synchrotron at the beam energies up to $E_b \approx 90$ GeV for protons, $E_b \approx 35$ AGeV for gold ions, and $E_b \approx 45$ AGeV for nuclei with Z/A = 0.5.

3.1 CBM physics program

A comprehensive review of the CBM program can be found in the CBM Physics Book [6]. This review describes the physics and theoretical concepts of compressed baryonic matter, the available experimental results, and theoretical predictions relevant to the heavy-ion collisions at FAIR energies of SIS100 ($E_b = 2-11~\text{AGeV}$) and SIS300 ($E_b = 11-45~\text{AGeV}$). The planned measurements at SIS100 energies, detector performance study with Monte-Carlo simulations, and particle production rate estimates are presented regularly in the CBM annual reports (for year 2013 see [7]). Most of the dense matter diagnostic probes such as production of multi-strange hyperons, particles with charm quark content, and lepton pair yields will be measured for a first time in the FAIR energy range by the CBM experiment. This builds a unique discovery potential of the CBM experiment at both SIS100 and SIS300 energies.

The CBM physics program is focused on a number of physics topics and corresponding observables

which are briefly highlighted below. A number of physics observables can be addressed already with beams energies of the SIS100 while some of them are fully accessible only at higher SIS300 energies.

The pressure gradients in the initial energy density result in a collective anisotropic expansion of the matter created in a heavy-ion collision. The generated anizotropic transverse flow is in particular sensitive to details of the QCD equation of state which governs this expansion. Subthreshold production of multistrange hyperons (Ξ and Ω) in Au+Au and C+C collisions at the SIS100 energies occur via sequential interaction between kaons and Λ hyperon which makes their production sensitive to the density of the matter created in a collision.

The in-medium modification of hadron properties in a dense baryonic matter serves as a signature for the chiral phase transition. It can be studied experimentally by measuring the mass distribution of vector mesons decaying into lepton pairs for heavy-ion collisions at SIS100 and SIS300 energies and for different collision systems. Leptons serve a role of unique penetrating probe which carries the information about evolution of the dense matter created in a heavy-ion collision.

An energy density of about seven times larger than that of a normal matter is reached in central heavy-ion collisions already at SIS100 energies. Under these conditions the participating nucleons overlap, and theory predicts a transition to a mixed phase of baryons and quarks, the so-called quarkyonic matter. A discontinuity or a strong variation with the heavy-ion collision beam energy of lepton pair production and event-by-event fluctuations of conserved quantities (e.g. baryon or strange number) at SIS100 and SIS300 energies will be a signature for such transition.

A coalescence model calculations predict that a maximum production yield of single and double strange hypernuclei, strange dibaryons, and heavy short-lived multi-strange particles in heavy-ion collisions should be reached at the collision energies covered by SIS100. A chain of single and double hypernuclei decay and strange dibaryons, and heavy short-lived multi-strange particle production in heavy-ion collisions at SIS100 energies can be studied by identifying hadrons from their weak decay products using the CBM detector subsystems.

A charm quark production properties can be accessed via open charm (e.g. D meson) and charmonium (J/Ψ) measurements. A measurement of the D meson production cross section and transverse momentum spectra for target nuclei of different size and in proton-nucleus collisions at SIS100 energies together with the transparency ratio $T_A = (\sigma_{pA} \to DX)/(A\sigma_{pN} \to DX)$ will allow to study the in-medium properties of charm quarks. A subthreshold production cross section and momentum spectra of charmonium (J/Ψ) in nucleus-nucleus collisions should be also accessible at SIS100 energies.

3.2 CBM detector subsystems

The CBM experiment plans to perform a systematic measurement of production yields, phase-space distributions, correlations, and fluctuation observables for various particle species produced in nuclear collisions with unprecedented precision provided by the high luminosity beams of FAIR. The experiment is designed to operate without hierarchical trigger system which is a paradigm change in data taking by high-energy heavy-ion experiments. A high-speed data acquisition system with self-triggered read-out electronics together with the radiation hard detector subsystems are mandatory for successful operation of the experiment in a high luminosity environment. The collision interaction rate (event statistics) together with online tracking and the high combinatorial background rejection power of the reconstruction algorithms (good signal to background ratio) determine the precision of the topological reconstruction and selection of events with rare signals such as multi-strange hyperons, hypernuclei, particles with charm quark content, and vector meson decay into lepton pairs.

An overview of the CBM experiment with particle identification detectors and the muon detection system is shown in Fig. 3(left) and Fig. 3(right), respectively.

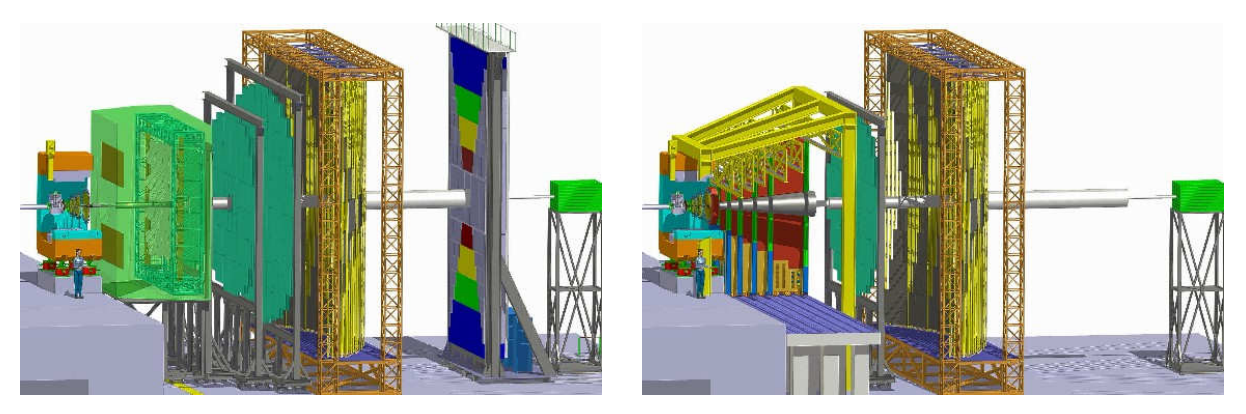


Fig. 3: The CBM experiment setup with (left) the particle identification detectors, and (right) the muon identification system.

The main CBM detector components and their purpose are described below.

3.2.1 Dipole magnet

The H-type superconducting dipole magnet with large polar angle acceptance ($\pm 25^{\circ}$) will provide an integrated magnetic field up to 1 Tm.

3.2.2 Micro-vertex detector

The micro-vertex detector (MVD) will provide a high spatial resolution to reconstruct the decay vertices of short lived particles such as D^0 (D^{\pm}) mesons which has a very small decay length $c\tau=124$ (314) μ m. The MVD is designed to have a very low material budget in order to reduce multiple scattering inside the detector by particles emitted from the collision vertex.

The MVD consists of 3 layers of monolithic active pixel sensors (MAPS) located 5, 10, and 15 cm downstream the target in the vacuum. A 4th MAPS station might be located at 20 cm behind the target. The transverse pixel size of the MAPS will be about $18-20~\mu$ m which allows for a spatial decay vertex resolution of $50-100~\mu$ m along the beam axis.

The total thickness of the detector is between $300 - 500 \mu m$ silicon equivalent for sensors and support structures, depending on the size of the stations.

3.2.3 Silicon tracking system

The task of the STS is to provide track reconstruction and momentum determination of charged particles. The multiplicity of charged particles is up to 600 per event within the detector acceptance. The STS consists of up to 8 tracking layers of silicon detectors. They are located downstream of the target at distances between 30 cm and 100 cm inside the magnetic dipole field. The required momentum resolution is of the order of $\Delta p/p = 1\%$. This performance can only be achieved with an ultra-low material budget of the stations, imposing particular restrictions on the location of power-dissipating front-end electronics in the fiducial volume. The concept of the STS tracking is based on silicon microstrip detectors on lightweight ladder-like mechanical supports. The sensors will be read out through multi-line micro-cables with fast electronics at the periphery of the stations where cooling lines and other infrastructure can be placed. The micro-strip sensors will be double-sided with a stereo angle of 0/7.5 degree, a strip pitch of 60 μ m, strip lengths between 20 and 60 mm, and a thickness of 300 μ m of silicon. The micro-cables will be built from sandwiched polyimide-Aluminum layers of several 10 μ m thickness.

3.2.4 Ring imaging Cherenkov detector

The RICH detector is designed to provide identification of electrons and suppression of pions in the momentum range below 8-10 GeV/c. This will be achieved using a gaseous RICH detector build in a standard projective geometry with focusing mirror elements and a photodetector. CO₂ with a pion threshold for Cherenkov radiation of 4.65 GeV/c will be used as radiator gas. The detector will be positioned behind the dipole magnet about 1.6 m downstream of the target. It will consist of a 1.7 m long gas radiator (overall length approximately 2 m) and two arrays of mirrors and photodetector planes. The mirror plane is split horizontally into two arrays of spherical glass mirrors, each 4×1.5 m². The 72 mirror tiles have 3 m radius of curvature, 6 mm thickness and a reflective AL+MgF₂ coating. Rings will be projected onto two photodetector planes of 2×0.6 m² each being located behind the CBM dipole magnet and shielded by the magnet yokes. The design of the photodetector plane is based on MAPMTs (e.g. H8500 from Hamamatsu) in order to provide high granularity, high geometrical efficiency, high detection efficiency of photons also in the near UV region and a reliable operation. In-beam tests with a RICH prototype being real dimension in its length could show that 22 photons are measured per electron ring. On the order of 100 rings are seen in central Au+Au collisions at 25 AGeV beam energy due to the large material budget in front of the RICH detector. Still, due to the high granularity (approx. 55000 channels) and high number of photons per ring, a pion suppression on the order of 500 is expected to be achieved according to simulations.

3.2.5 Transition radiation detector

Three Transition Radiation Detector stations each consisting of 3 detector layers will serve for particle tracking and for the identification of electrons and positrons with momentum p > 1.5 GeV/c ($\gamma > 1000$). The detector stations are located at approximately 5 m, 7.2 m and 9.5 m downstream the target, the total active detector area amounts to about 600 m². At small forward angles and at a distance of 5 m from the target, we expect particle rates of the order of 100 kHz/cm² for 10 MHz minimum bias Au+Au collisions at 25 AGeV. In a central collision, particle densities of about $0.05/\text{cm}^2$ are reached. In order to keep the occupancy below 5% the minimum size of a single cell should be about 1 cm². The TRD detector readout will be realized in rectangular pads giving a resolution of $300 - 500 \,\mu\text{m}$ across and 3-30 mm along the pad. Every second transition radiation layer is rotated by 90 degree. Prototype gas detectors based on MWPC and GEM technology have been built and tested with particle rates of up to 400 kHz/cm² without deterioration of their performance. The pion suppression factor obtained with 9 TRD layers is estimated to be well above 100 at an electron efficiency of 90%. For measurements at SIS100 only one station with 3 detector layers will be used as an intermediate tracker between the STS and the TOF wall.

3.2.6 Time of Flight detector

The time of Flight detector (TOF) consists of an array of multi-gap resistive plate chambers which are used for hadron identification via their time-of-flight measurement. The TOF detector covers an active area of about 120 m² and is located about 6 m downstream of the target for measurements at SIS100, and at 10 m at SIS300. The required time resolution is of the order of 80 ps. For 10 MHz minimum bias Au+Au collisions the innermost part of the detector has to work at rates up to 20 kHz/cm². Prototype MRPCs built with low-resistivity glass have been tested with a time resolution of about 40 ps at 20 kHz/cm². At small deflection angles the pad size is about 5 cm² corresponding to an occupancy of below 5% for central Au+Au collisions at 25 AGeV.

3.2.7 Projectile spectator detector

The PSD is a compensating lead-scintillator calorimeter designed to measure the energy distribution of the projectile nuclei fragments (spectators) and forward going particles produced close to the beam rapidity. The main design requirements of the PSD are (i) forward rapidity coverage and sufficient energy resolution to allow for precise collision centrality determination and consequently of the number of participating nucleons and (ii) granularity in the plane transverse to the beam direction which is needed for the collision symmetry plane reconstruction. The proposed 44 module design of the PSD covers large transverse area around the beam spot position such that most of the projectile spectator fragments deposit their energy in the PSD.

3.2.8 Muon chamber system

The experimental challenge for muon measurements in heavy-ion collisions at FAIR energies is to identify low-momentum muons in an environment of high particle densities. The CBM concept is to track the particles through a hadron absorber system, and to perform a momentum-dependent muon identification. This concept is realized by segmenting the hadron absorber in several layers, and placing triplets of tracking detector planes in the gaps between the absorber layers. The muon detector system (MUCH) is placed downstream of the Silicon Tracking System (STS) which determines the particle momentum. In order to reduce meson decays into muons the MUCH system has to be as compact as possible. The actual design of the MUCH consists of 6 hadron absorber layers (iron plates of thickness 20 cm, 20 cm, 20 cm, 30 cm, 35 cm, 100 cm) and 15-18 gaseous tracking chambers located in triplets behind each iron slab. The definition of a muon depends on its momentum which varies with the mass of the vector mesons and with beam energy. The challenge for the muon chambers and for the track reconstruction algorithms is the very high particle density of up to 0.5 hits/cm² per event in the first detector layers after 20 cm of iron. For a reaction rate of 10 MHz this hit density translates into a hit rate of 5 MHz/cm². Prototype chambers based on GEM technology were operated successfully at rates of about 3 MHz/cm² with pion beams. In total, the muon chambers cover an active area of about 70 m² subdivided into about half a million channels. The low particle multiplicities behind the muon absorber allows to trigger on muon pairs. The trigger concept is based on the measurement of short track segments in the last tracking station triplet, and extrapolation of these tracks to the target. After selection of tracks with good vertices the event rate can be reduced already by a factor of about 600 for J/Ψ measurements in minimum bias Au+Au collisions. For J/Ψ measurements at SIS100 a MUCH start version with 3 chamber triplets is sufficient.

3.2.9 Online data processing

Precision measurement of physics observables for particles with very small production cross section requires high reaction rates. The CBM sub-detectors, the online event selection and the data acquisition systems will be designed for event rates up to 10 MHz, corresponding to a beam intensity of 10^9 ions/s and a 1% interaction target rate. Assuming a bandwidth of the fiber link to the storage element of

1 GByte/s and an average event size for a minimum bias Au+Au collisions of about 10 kByte, an event rate of only 100 Hz can be accepted. A measurement at the 10 MHz rate requires an online (hardware) event selection algorithms with background rejection factor of 100 or more. The event selection system will be based on a fast on-line event reconstruction running on a high-performance computer farm equipped with many-core CPUs and graphics cards (GSI GreenIT cube). Track reconstruction, which is the most time consuming combinatorial stage of the event reconstruction, will be based on parallel track finding and fitting algorithms, implementing the Cellular Automaton and Kalman Filter methods. For open charm production measurements the online trigger will search for secondary vertices which requires high speed tracking and event reconstruction of the STS and MVD systems. The highest suppression factor has to be achieved for J/Ψ mesons where a high-energetic pair of electrons or muons is required in the TRD or in the MUCH detectors. For low-mass electron pairs the online selection is limited due to the large number of rings per event in the RICH detector caused by the material budget of the STS. In the case of low-mass muon pairs some background rejection might be feasible.

4 Projectile spectator detector (PSD)

4.1 Design requirements

Experimental estimate of global event characteristics in nucleus-nucleus collisions such as the centrality of the collision which is related to the number of participating nucleons and the reaction plane orientation are challenging tasks in any high-energy heavy-ion experiment.

In heavy-ion interactions the event-by-event determination of the collision centrality is used to study observables like the collective flow, particle multiplicities and fluctuations which vary strongly with centrality. The collision centrality can be determined either by the multiplicity of produced particles in the participant zone or by measuring energy carried by the non-interacting nucleons (projectile spectators) and detected by forward hadron calorimeter. The measurement of the number of projectile spectators allows to estimate the number of the participants and hence the impact parameter b, which are strongly correlated.

The collective flow of particles produced in a heavy-ion collision is an important observable which provides information about the dynamics of the reaction and the properties of the matter in the fireball [8–10]. The flow is defined with respect to the reaction plane which is spanned by the beam direction and the impact parameter of the collision. The orientation of the impact parameter is reflected by the spectators, i.e. the nucleons and fragments which do not participate in the collision, which are deflected in the direction of the impact parameter. Therefore, the most direct method to determine the reaction plane is to measure the position and energy of the spectators at a certain distance downstream the target. To fulfill such a requirement, the PSD must have both appropriate energy resolution and modular structure with fine azimuthal segmentation to measure the position of the spectators with good resolution.

For event characterization in the CBM experiment it is planned to use a forward hadron calorimeter, the so called Projectile Spectator Detector (PSD). The requirements and the concept of the PSD are described in the following.

The general requirements to the PSD performance can be formulated as follows:

- Spectators detection in the beam energy range of $E_b = 2 35$ AGeV.
- Operation at beam intensities up to 10⁹ Au ions per sec.
- Reaction plane determination with an accuracy better than 40 degree.
- Determination of collision centrality classes with an accuracy better than 10%.

As will be shown in the report, these requirements can be met if the PSD has the following properties:

- Large transverse area (of the order of $1.5 \times 1.5 \text{ m}^2$) to register the collision spectators down to beam energies of a few AGeV.
- Energy resolution of $\sigma_E/E < 60\%/\sqrt{E(\text{GeV})}$
- Transverse granularity of $20 \times 20 \text{ cm}^2$
- Radiation hard photon detectors with high-rate capabilities

4.2 Detector concept

The requirements discussed above can be fulfilled by a compensating hadron calorimeter. The hadron shower produced in absorbers consists in reality of two, electromagnetic (e) and pure hadronic (h) shower

components. The former one is coming from neutral pions produced in nuclear interactions and is the dominant source of the fluctuations. The energy sharing between the e and h components can be very different from event to event, and depends mainly on the nature of the first interaction, which may produce (or not) a π^0 . The equalization of the calorimeter response to the e and h components (e/h = 1), i.e. the compensation condition, eliminates one of the dominant source of the energy fluctuation and hence improves the energy resolution of the calorimeter. The other advantages of compensating calorimeters are linearity and Gaussian shape signal of the detector response. Initially, this concept was applied to the uranium calorimeters [11] and then transformed to the more general principles.

Now this approach is successfully applied to the calorimeters with iron and/or lead absorbers [12]. It was shown that the compensating condition (e/h=1) depends on the relative absorber/active thickness ratio. Compensating condition e/h=1 is fulfilled for Fe/Scintillator sampling ratio equal 20. For lead the absorber sampling ratio Pb/Scintillator should be equal 4. The last case of lead-scintillator calorimeter is rather attractive due to the smaller compensating ratio and consequently smaller sampling fluctuations of the shower.

At present, there are a few performance measurements for the calorimeters with similar structure. One lead-scintillator compensating calorimeter with the resolution of about $58\%/\sqrt{E}$ was used in the WA97 experiment at CERN [13]. This calorimeter has a classical light readout with wave-shifter plates and PMT's. Unfortunately, such a readout suffers from the Cherenkov light in the WLS-plates, and from the nuclear counter effect in PMT's placed behind the active part of the calorimeter. A similar calorimeter prototype [14] with the finer sampling developed for the JLC project has a resolution of about $50\%/\sqrt{E}$ and avoids such drawbacks. It uses fiber-tile readout that ensures efficient light collection in the scintillator layers together with perfect transverse uniformity of the energy resolution. At the same time, the use of a large amount of PMT's for the readout of each scintillator layer leads to a high complexity and high costs of such a calorimeter.

The review of the current experimental situation reveals that a full compensating modular lead-scintillator calorimeter with a sampling ratio 4:1 meets the above requirements, and, hence, was selected for the PSD calorimeter. The proposed calorimeter design of the PSD for the CBM combines the advantages of the fiber-tile readout with the simplicity of the photon detectors. The PSD consists of 44 individual modules with a transverse size of 20×20 cm² each. Each module includes 60 lead-scintillator sandwiches with the total interaction length of about $6\lambda_i$. Every 6 consecutive layers of scintillators are readout by a single photon detector via the WLS-fibers. These ten sections with the individual light readout provide the longitudinal segmentation of PSD modules. The light from the WLS-fibers is readout by Micro-Pixel Avalanche Photodiodes (MAPD's) instead of PMT's. In spite of the relatively recent appearance, this new type of photodiodes starts to be intensively used at modern setups due to their remarkable properties. Good photon detection efficiency and a gain comparable to normal PMT's, the compactness, low cost and simplicity of the operation make these devices very attractive for the different applications including the calorimetry. As shown below, the proposed PSD design fulfills the CBM requirements.

Recently, a full compensating modular lead-scintillator calorimeter with a sampling ratio of 4:1 with fiber-tile readout light collection and readout by Micro-Pixel Avalanche Photodiodes has been constructed for the NA61 experiment at CERN [15–17], and has been used in the Be-Be experiments in 2011-2013. This calorimeter is rather similar to the PSD for the CBM experiment.

5 PSD performance

5.1 Heavy-ion collision modeling

The PSD performance is evaluated for Au+Au collisions with projectile beam energies between 2 and 35 AGeV simulated with a heavy-ion event generator DCM-QGSM [18–28]. The DCM-QGSM generator is developed jointly by the JINR (Dubna) and INR (Troitsk) groups. It is based on a Multi Stage Dynamical Model and includes generation of collision fragments which is a crucial ingredient for the PSD performance study. In addition, a sample of Au+Au collisions simulated with the UrQMD v3.3 [29, 30] event generator was used to evaluate the PSD performance for a measurement of directed and elliptic flow of hadrons.

The accuracy of the collision centrality and the reaction plane determination depends on the multiplicity and the energy distribution of fragments, and on the amount of the directed flow (v_1) that they carry. The transverse momentum of fragments generated by the DCM-QGSM code reveals rather good agreement with the experimental data [18–28]. Figure 4 shows the directed flow of protons generated by the DCM-QGSM and UrQMD event generators for semi-central Au+Au collisions at the projectile beam energy between 2 and 35 A GeV. The directed flow as function of rapidity generated by the DCM-QGSM model shows good agreement with the experimental data provided by the E895 [31] and STAR [32] Collaborations down to the forward rapidity (spectator) region, while UrQMD does not follow the change of measured v_1 with the collision energy. The availability of fragments in the spectator region and the qualitative agreement with the experiment data for directed flow justifies the use of the DCM-QGSM for the PSD performance study.

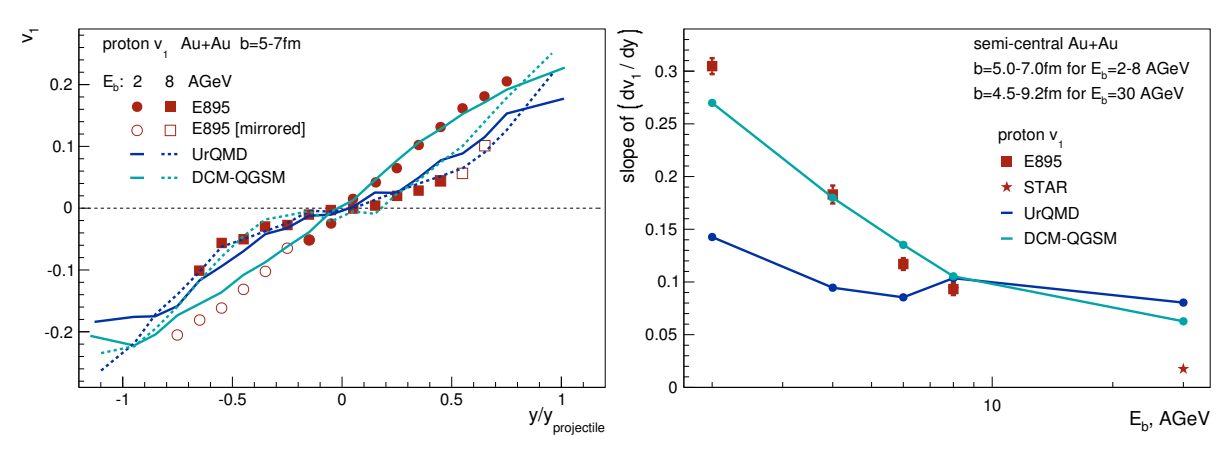


Fig. 4: Directed flow (v_1) of protons produced in semi-central Au+Au collisions. The proton v_1 simulated with the DCM-QGSM [18–28] and UrQMD v3.3 [29, 30] event generators are compared to experimental data from the E895 [31] and STAR [32] Collaborations. (left) Proton v_1 versus rapidity (y) normalized to the projectile rapidity (y) range (y) for Au+Au collisions with the projectile beam energy (y) at midrapidity (y) as a function of projectile beam energy (y) for semi-central Au+Au collisions. The impact parameter range is chosen to be (y) for (y) for

5.2 CBM detector geometry modeling

The CBM detector geometry and its response to particles simulated with heavy-ion event generators are implemented within a GEANT4 [33] Monte-Carlo simulation framework. Hadronic processes, models and cross sections within the GEANT4 package were configured using the physics list FTFP_BERT

which contains all standard EM processes and uses a Bertini-style cascade for hadrons below 5 GeV, and the FTF (Fritiof) model for high energies above 4 GeV. As a cross check an alternative physics list QGSP_BIC_HP (which enables standard EM processes, Bertini cascade for hadrons of energy below 10 GeV, and QGS model for high energies above 20 GeV) was used.

The model of the CBM subsystems used for the PSD performance study is shown in Fig. 5(left). The geometry includes a 250 μ m thick Au target, eight silicon tracking stations (STS) [34] located 30-100 cm far from the target inside the dipole magnet, the aluminum beam pipe with a variable cross section and thickness of a few mm, and the PSD. The optimal PSD location is at 8 (15) meters from the target for collision energies at SIS100 (SIS300). The transverse segmentation of the PSD is illustrated in Fig. 5(right). It is elongated along the lab x direction and includes 44 modules with a 20×20 cm² cross section in the transverse plane and a beam hole formed by the inner corners of the four central modules which in Fig. 5(right) are marked in red color. Simulation studies performed with a smaller (and more expensive) module size of 10×10 cm² showed only marginal improvement of the reaction plane resolution.

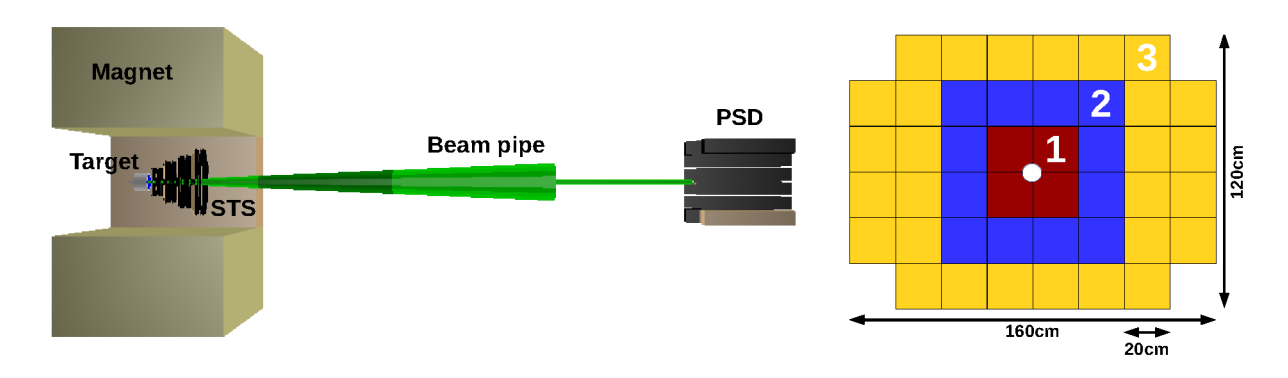


Fig. 5: (left) CBM detector geometry used for the PSD performance study. The simulated geometry includes (i) a 250 μ m thick Au target, (ii) eight silicon tracking stations STS [34] (black), (iii) a magnetic field generated by the CBM dipole magnet (dark yellow), (iv) a few mm thick aluminum beam pipe (green), and (v) the PSD (dark gray). The PSD detector is positioned at 8 (15) m from the target for performance study at SIS100 (SIS300) energies. (right) Transverse segmentation of the PSD. The PSD geometry is elongated in the horizontal direction and has 44 modules with a square cross section of $20\times20~\text{cm}^2$. The central region around the beam hole (6 cm diameter) has a 2×2 segmentation which allows to use the spectators produced very close to the beam rapidity for anisotropic flow studies. The modules used to construct subevents PSD1, PSD2, and PSD3 are marked in red, blue, and yellow color, respectively.

The ion beam is horizontally deflected by the field of the dipole magnet (along the x direction in the laboratory frame) which has a nominal field integral of about 1 Tm. The PSD is shifted by x_{shift} for each collision energy, magnetic field strength, and detector distance to the target, such that the beam always pass the PSD via its beam hole. The magnetic field values used in simulations and the PSD shift along the x direction for different detector distances from the target are shown in Tab. 1 and Fig. 6(left), respectively.

For the performance studies, the PSD modules are grouped into three classes (subevents) according to the illustration in Fig. 5(right). The subevents allow to use the PSD as a standalone detector for centrality and reaction plane determination. In the following we refer to these subevents as PSD1 (red), PSD2 (blue), PSD3 (yellow), and PSD-full in case all modules are used together.

FAIR ring	SIS100	SIS300	
Collision system, beam+target	Au+Au	Au+Au	
Beam kinetic energy E_b , AGeV	2, 4, 6, 10	15, 25, 35	
Heavy-ion event generator	1. DCM-QGSM (includes fragment simulation)		
Heavy-Ion event generator	2. UrQMD (all energies, only optimal distances)		
Simulated geometry, GEANT4	CBM subsystems: Au target, magnet, beam pipe, STS, PSD		
GEANT4 physics list	1. FTFP_BERT		
GEAN14 physics list	2. QGSP_BIC_HP		
	$0.5 (0.1-1.0)$ for $E_b = 2$ AGeV	1.0	
Magnetic field, $B \times \rho$, Tm	$0.6 \text{ for } E_b \text{ of } 4 \& 6 \text{ AGeV}$		
	$1.0 \text{ for } E_b = 10 \text{ AGeV}$		
PSD to target distance, m	8*,10,12,15	8,10,12,15*	
Additional configurations	Forward TOF (charged hadron hits in PSD acceptance)		

Table 1: List of simulated configurations used for the performance study. The PSD distance to the target which is planned to be used during SIS100 and SIS300 running is marked with *.

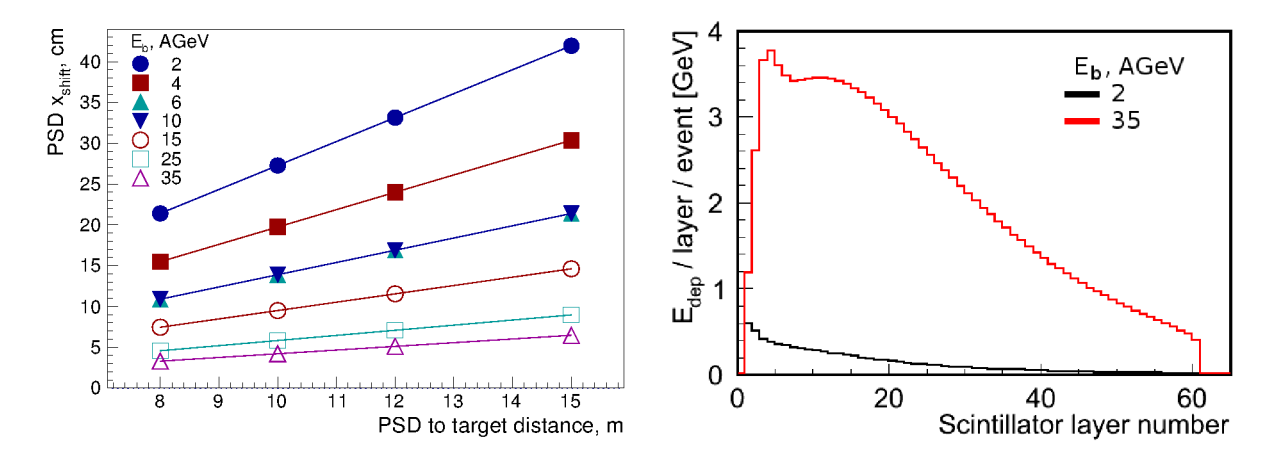


Fig. 6: (left) Horizontal shift, x_{shift} , of the PSD which accounts for the beam spot deflection by the CBM magnet at the location of the PSD. The PSD x_{shift} is presented as a function of the PSD distance to the target for E_b =2, 4, 6, 10, 15, 25, and 35 AGeV. (right) Average energy deposition in the scintillator layers of the PSD for minimum bias Au+Au collisions at E_b = 2 and 35 AGeV.

5.3 Collision fragment detection

To demonstrate that the PSD has a sufficient coverage in the transverse plane to detect most of the collision fragments and is able to reconstruct their energy, we study with Monte-Carlo simulations the particle hit distribution and their energy deposition in the detector at different energies and different distances from the interaction point.

Figure 6(right) shows the longitudinal energy deposition in the individual scintillator layers of the PSD (averaged over all modules). Simulated for minimum bias Au+Au collisions at E_b =2 and 35 AGeV, these distributions show that most of the energy from the hadronic shower generated by spectator fragments is deposited in a first 20-30 layers. Within a few percent the deposited energy distribution is confined in the PSD sensitive volume, which justifies the choice of the detector interaction length of about $5.6\lambda_{int}$ provided by a 60 lead-scintillator sandwich design of each module. This demonstrates that the PSD can reconstruct the energy of the incoming particles.

Figure 7 shows particle yields at different rapidity y (normalized to the beam rapidity, $y_{\text{projectile}}$) in Au+Au collisions simulated with the DCM-QGSM model at E_b =2, 10, and 35 AGeV. The distribution of all generated particles (black) is compared to the PSD1 (blue), PSD2 (magenta), and PSD3 (cyan) subevents, and particles deposited at least four hits in the STS (red). The PSD and each of its subevents cover the region around projectile rapidity $y/y_{\text{projectile}} \approx 1$, while the STS detector is mainly sensitive to the particles produced at midrapidity, $|y/y_{\text{projectile}}| < 0.5 - 0.7$, except in collisions at the lowest SIS100 energy, E_b =2 AGeV, where the acceptance of both PSD and STS is shifted towards beam rapidity.

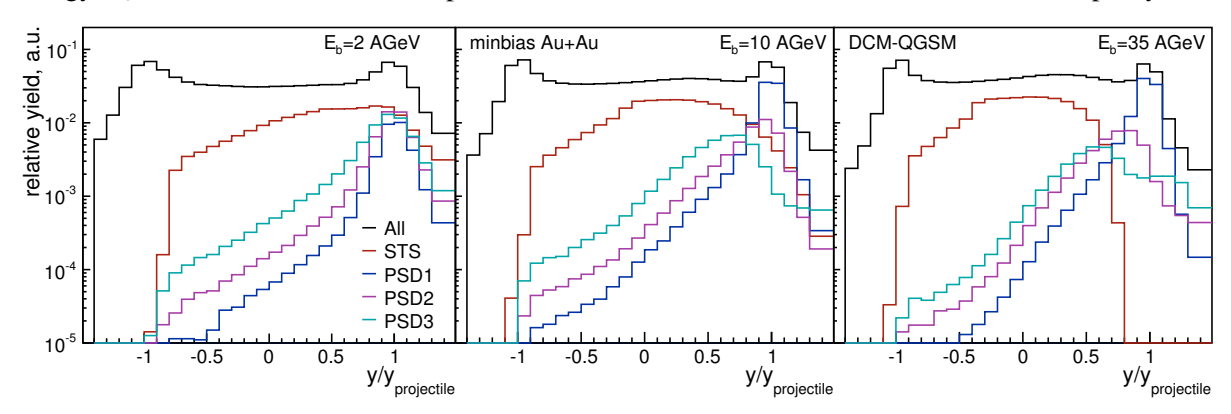


Fig. 7: Simulated particle yields vs. rapidity normalized to the projectile rapidity for minimum bias Au+Au collisions at E_b of 2 AGeV (left), 10 AGeV (middle), and 35 AGeV (right). The full particle phase space, particles which produce at least four hits in the STS detector, and hits the first layer of the PSD subevents are shown. The PSD is positioned at 8 (15) m from the target at $E_b = 2$ and 10 (35) AGeV.

The PSD hit distribution in the transverse (xy) plane to the beam (z) direction is shown in Fig. 8 for minimum bias Au+Au collisions at E_b =2, 10, and 35 AGeV. With a chosen position of the PSD distance to the target (8 m for E_b =2, 10 AGeV and 15 m for E_b =35 AGeV) the collision fragment distributions are well covered by the PSD acceptance. While the hit distribution of charged fragments in a vertical (y) direction is rather symmetric, it is distorted in horizontal (x) direction by the field of the dipole magnet. As can be seen from upper panels of Fig. 8, the elongated geometry of the PSD in x direction compensates for this effect and allows to recover most of the deflected fragments. A small fraction of very forward moving fragments is not registered by the PSD due to the beam hole. This effect is particularly large for heavy ($A \ge 4$) fragments, especially at higher energies ($E_b = 35$ AGeV), as the fragment rigidity is close to that of beam ions. In future, a replacement of the four central modules by a removable higher granularity module without the beam hole would allow to address this issue, though it may limit the allowed beam intensity during the detector operation.

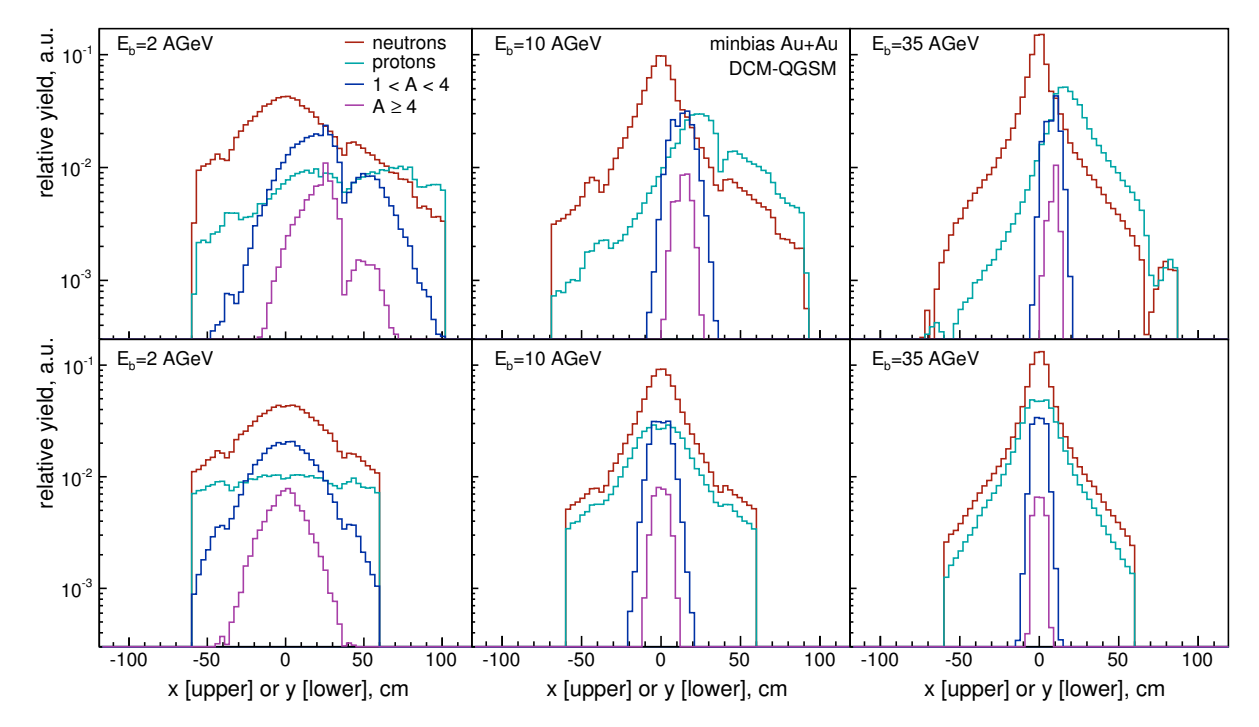


Fig. 8: Particle hit distribution in the transverse (xy) plane of the PSD for minimum bias Au+Au collisions at E_b of 2 AGeV (left), 10 AGeV (middle), and 35 AGeV (right). A value of x = y = 0 corresponds to the beam spot position without magnetic field. The PSD is shifted according to the x-shifts shown in Fig. 6. The distributions of different fragments (neutrons, protons, light fragments with A = 2 and 3, and heavy fragments with $A \ge 4$) are shown separately. The PSD is positioned at 8 (15) m from the target at $E_b = 2$ and 10 (35) AGeV.

5.4 Collision centrality determination

The magnitude of the impact parameter, b, or the number of participating nucleons for a given heavyion collision are not known experimentally. Instead, the multiplicity of the produced particles in the overlap zone of the nuclei is used as an experimental proxy of the b value. Since the b value and particle multiplicity are correlated only on average, the measured multiplicity can be only used to estimate the average impact parameter value, $\langle b \rangle$, and its spread, σ_b , for a given multiplicity (centrality) class of events. In practice, all events are sorted in centrality classes, with most central ($b \approx 0$) being the collisions with highest multiplicity of the produced particles and peripheral ($b \approx 0$) being the radii of the two nuclei) with low multiplicity.

The multiplicity of the spectators (collision fragments) can be also used for collision centrality determination. Spectators provide an independent way to determine centrality which is important for physics studies such as event-by-event fluctuations at midrapidity of various physics observables. In the case of spectator measurements, the most central events correspond to a low spectator multiplicity (or a small energy deposition in the PSD), while peripheral events result in large amount of spectators (and typically in a large energy deposition in the PSD).

In this section we study the PSD performance for the centrality determination as a standalone detector (using the PSD subevent), and in combination with the STS detector which measures the multiplicity of the produced particles.

Figure 9 illustrates the procedure used for the centrality determination for Au+Au collisions at $E_b = 10$ AGeV. The PSD is used standalone by utilizing correlation between energies deposited in the PSD subevents (Fig. 9(d)), and in a combination with the STS detector multiplicity (Fig. 9(a-c)). In the case of the PSD standalone analysis one has to exclude very peripheral collisions when only a few heavy fragments are registered by the PSD, and discriminate these events from very central collisions. Therefore, it was required to have at least 40 GeV of energy in the PSD1 subevent or total energy in two PSD2 and PSD3 subevents of 15 GeV. This requirement was adjusted for different collision energies.

To define the centrality classes based on the correlations shown in Fig. 9 a polynomial (red solid line) was fitted to the average energy in a given PSD subevent vs. STS multiplicity (or PSD1 energy in case of PSD standalone centrality determination). Using these polynomial lines, all events were sorted in centrality classes of 5% with equal (within 1%) number of events in each class. The boundaries between centrality classes are shown by dashed red lines in Fig. 9 (these lines are perpendicular to the polynomial fit). The most right (left) line in panels "a-c" ("d") corresponds to the most central event class.

Figure 10 presents the results of the procedure described above after applying it for different collision energies. The left panels show the average impact parameter value $\langle b \rangle$ (central value) and σ_b (as the error bars) versus centrality estimate from different subevent correlations. The right panels present the same information in terms of impact parameter resolution $\sigma_b/\langle b \rangle$ of different centrality estimators.

The results in Fig. 10 demonstrate that the PSD can be used standalone for the centrality determination and, depending on the collision energy, has a comparable impact parameter resolution $\sigma_b/\langle b \rangle$ to that of the STS, which provides an independent method in the CBM experiment for the centrality determination with spectator multiplicity. When used in a combination with the STS detector, the PSD helps to improve the overall centrality determination in the centrality range of 0-40% and allows for centrality determination in narrow centrality classes with a width of at least 5%.

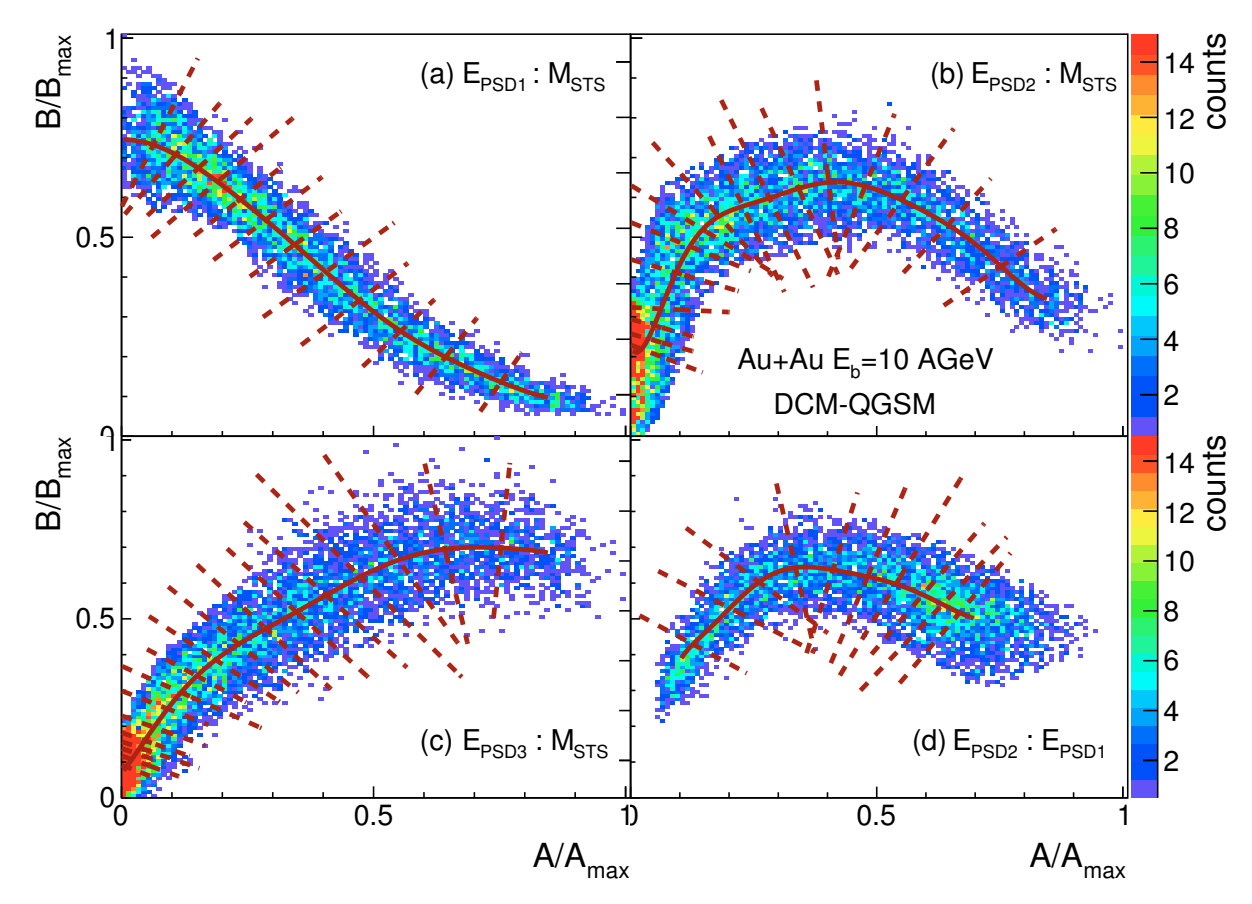


Fig. 9: Correlation between $B/B_{\rm max}$ and $A/A_{\rm max}$ with A (B) being the energy recorded in different PSD subevents or the multiplicity of particle tracks in the STS for Au+Au collisions at $E_b = 10$ AGeV. Both A and B are normalized to their maximum values $A_{\rm max}$ and $B_{\rm max}$. The panels (a,b,c) show the correlation between the energy of the PSD(1,2,3) subevent and STS track multiplicity, while panel (d) shows the correlation between the energy of the PSD2 and PSD1 which is used for PSD standalone centrality determination. Dashed red lines indicate the boundaries between different centrality classes (with most central collisions being on the right hand side of panels (a)-(c) and on the left hand side for panel (d)) and the solid red lines indicate the mean of the correlation at a given slice of $A/A_{\rm max}$ (see text for more details). The PSD is positioned at 8 m from the target.

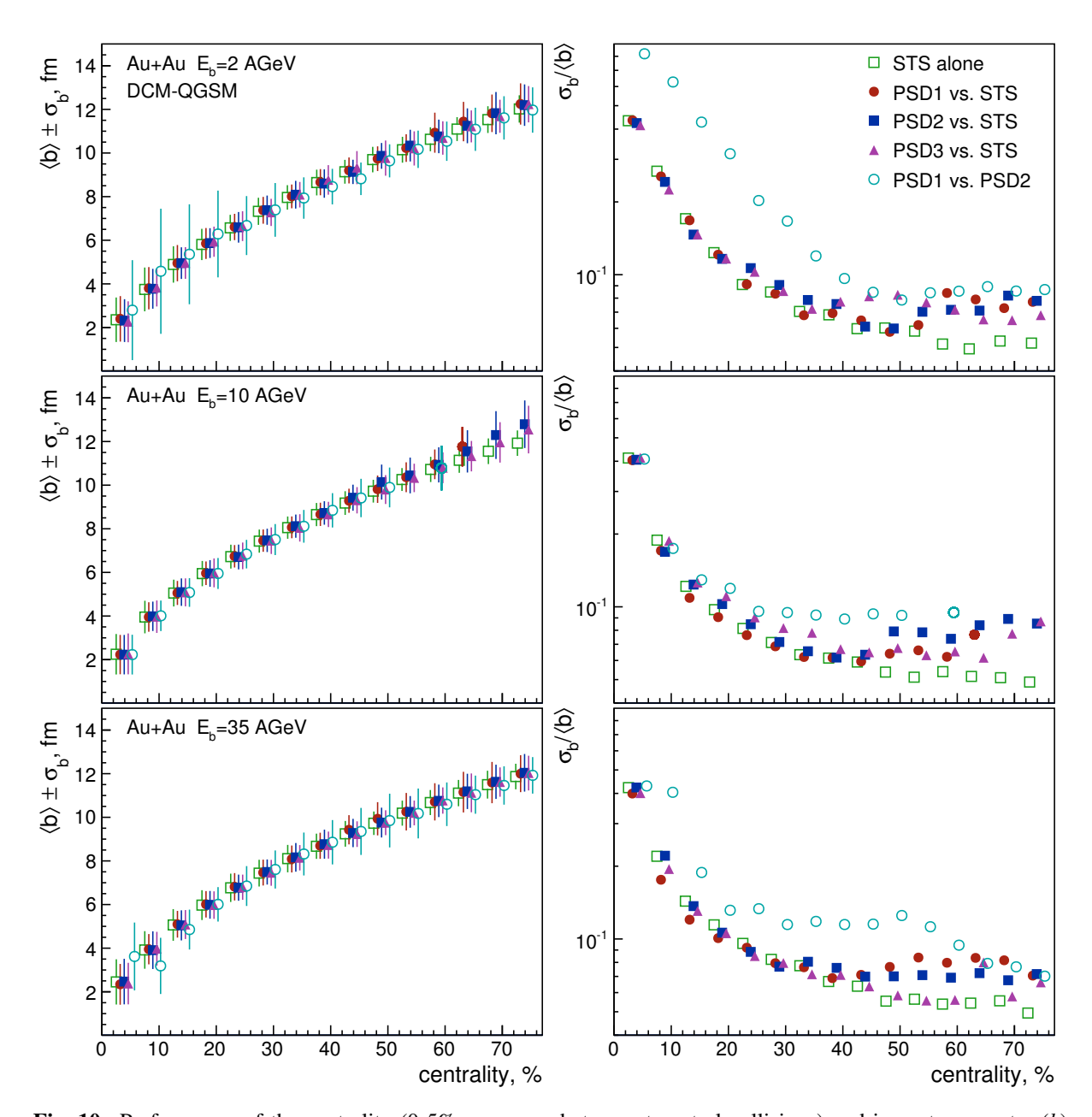


Fig. 10: Performance of the centrality (0-5% corresponds to most central collisions) and impact parameter (*b*) determination with different combinations of PSD subevents and STS track multiplicity. (left) Average $\langle b \rangle$ (central value) and width σ_b (error bars) of the impact parameter distribution for different centrality classes defined with different detector combinations. (right) Impact parameter resolution ($\sigma_b/\langle b \rangle$) vs. centrality. Results are presented for $E_b = 2$ AGeV (upper panels), 10 AGeV (middle panels), and 35 AGeV (bottom panels). The PSD is positioned at 8 (15) m from the target at $E_b = 2$ and 10 (35) AGeV.

5.5 Reaction plane reconstruction

Similar to the magnitude of the impact parameter, its direction (or the orientation of the collision reaction plane spanned by the impact parameter and the beam direction) is not known experimentally. To estimate the reaction plane orientation it is common to use the azimuthal asymmetry of particle production in the transverse plane to the beam direction.

Due to the momentum transfer between participants and spectators, the spectators (collision fragments) are deflected in the course of the collision. For non-central collisions, the asymmetry of the initial energy density in the transverse plane is aligned in the direction of the reaction plane, and the spectator deflection direction is correlated with the impact parameter (or reaction plane) direction. The plane spanned by the directions of the beam and spectator deflection (spectator plane) can be used as an estimate of the reaction plane orientation. In the following the azimuthal angle of the reaction plane in the laboratory frame is denoted as Ψ_{RP} .

The spectator deflection is experimentally accessible. In CBM it can be estimated event-by-event by utilizing the transverse segmentation and energy deposition in each of the PSD modules. In that respect, the PSD is a unique CBM detector which provides information about spectator deflection in the reaction plane. The estimated azimuthal angle of the spectator plane is called the event plane angle, $\Psi_{1,EP}^{-1}$.

The finite number of fragments and the fluctuation of the particle multiplicity from one collision to another at fixed impact parameter orientation result in a difference between the event plane and the reaction plane orientation. This difference is usually quantified in terms of the event plane resolution (a Gaussian width of the $\Psi_{RP} - \Psi_{1,EP}$ distribution).

Given the reaction plane orientation is known, one can study physics observables relatively to the reaction plane orientation. For this, it is convenient to decompose the particle azimuthal distribution relative to the reaction plane in a Fourier series [35]

$$\frac{dN}{d\phi} \sim 1 + 2\sum_{n} v_n \cos n(\phi - \Psi_{\text{RP}}). \tag{1}$$

Here ϕ is the particle azimuthal angle and v_n are called the anisotropic transverse flow coefficients. A first few coefficients have special names, in particular the first, v_1 , and second, v_2 , are called the directed and elliptic flow, respectively. According to the Eq. 1, the v_n can be defined from the equation

$$v_n = \langle \cos n(\phi - \Psi_{RP}) \rangle. \tag{2}$$

where the brackets $\langle ... \rangle$ denote the average over all particles in a given event and over a large ensemble of events. Using the event plane angle, $\Psi_{1,EP}$, an experimental estimate of v_n can be obtained with the event plane method [35]

$$v_n\{\Psi_{1,\text{EP}}\} = \frac{\langle \cos n(\phi - \Psi_{1,\text{EP}}) \rangle}{R_{n,\text{EP}}}.$$
 (3)

The event plane resolution correction factor $R_{n,EP}$ corrects for the finite event plane angle resolution relatively to the reaction plane and is defined as

$$R_{\text{n.EP}} = \langle \cos n(\Psi_{\text{1.EP}} - \Psi_{\text{RP}}) \rangle. \tag{4}$$

 $R_{\rm n.EP}$ value ranges between zero (very poor resolution) and unity (very good resolution).

Below we demonstrate the performance of the PSD for the event plane determination. We compare it with that of other CBM subsystems such as STS, and show the PSD advantages over alternative detector setup at forward rapidity such as a forward time of flight (TOF) detector. For the latter comparison

¹In general, the event plane angle $\Psi_{n,EP}$ can be defined for any harmonic n. Here we reduced the discussion to n=1 because we study spectator deflection which represents the directed flow v_1 of spectators (v_1 is defined below).

we used a simplified simulation setup when only charged fragment hits generated in the transverse area which corresponds to the PSD acceptance are considered (no particle energy reconstruction, no neutral fragments detection). We also present results from the complete data driven analysis (only using information reconstructed by the CBM sub-detectors) of the proton elliptic flow coefficient in Au+Au collisions at $E_b = 10$ AGeV simulated with the UrQMD model. Based on these results we project the PSD performance for flow measurements of other particle species such as strange and multi-strange hyperons Λ and Ω which are included in the CBM physics program.

5.5.1 Event plane correction for detector non-uniformity

The event plane angle is calculated from the energy deposition in a given module of the PSD or with reconstructed particles in the STS by constructing a so-called flow **Q**-vector [35] (two-dimensional vector in the transverse to the beam plane)

$$\mathbf{Q} \equiv (Q_x, Q_y) = \sum_i \omega_i (\cos n\phi_i, \sin n\phi_i). \tag{5}$$

Here ϕ_i is the azimuthal angle of the *i*-th particle reconstructed by the STS or azimuthal angle of the center in the transverse plane of the *i*-th PSD module. w_i is a weight which is used to improve sensitivity of the event plane to the reaction plane. In case of the STS, the weight w_i is the rapidity of the particle *i* with an additional factor '-1' for pions to account for the fact that pion v_1 has an opposite sign to that of protons. Only particles with $y/y_{\text{projectile}} < 0.8$ were used for the event plane estimate with STS. In case of the PSD, the weight w_i was chosen to be the energy in a given module *i*. The event plane angle $\Psi_{1,\text{EP}}$ can be calculated from the **Q**-vector components

$$\Psi_{1,\text{EP}} = \text{atan2}(Q_{y}, Q_{x}). \tag{6}$$

The dipole magnetic field distorts the azimuthal distribution of particles in the PSD (see Fig. 8), which results in off-centered values (mainly in the x direction) of the PSD \mathbf{Q} -vector. To correct for the azimuthal asymmetry of the PSD energy distribution, a \mathbf{Q} -vector recentering procedure is applied

$$Q'_{x,y} = \frac{Q_{x,y} - \langle Q_{x,y} \rangle}{\sigma_{Q_{x,y}}},\tag{7}$$

where $\langle Q_{x,y} \rangle$ and $\sigma_{Q_{x,y}}$ are event averaged mean and Gaussian width of the $Q_{x,y}$ distribution. The $\langle Q_x \rangle$ dependence for a given PSD subevent on the total energy in the same subevent is shown in Fig. 11. The strong energy dependence of $\langle Q_x \rangle$ (solid symbols) is removed after the recentering procedure is applied (open symbols). The same procedure also flattens the event plane distribution which is illustrated in Fig. 12(left). Figure 12(right) shows effect of the recentering on the event plane resolution. Resolution of the full PSD before recentering is strongly distorted by the magnet field and is very bad (red open circles), while after recentering (red solid circles) it is almost twice better than the resolution of the event plane calculated with the STS detector (blue squares).

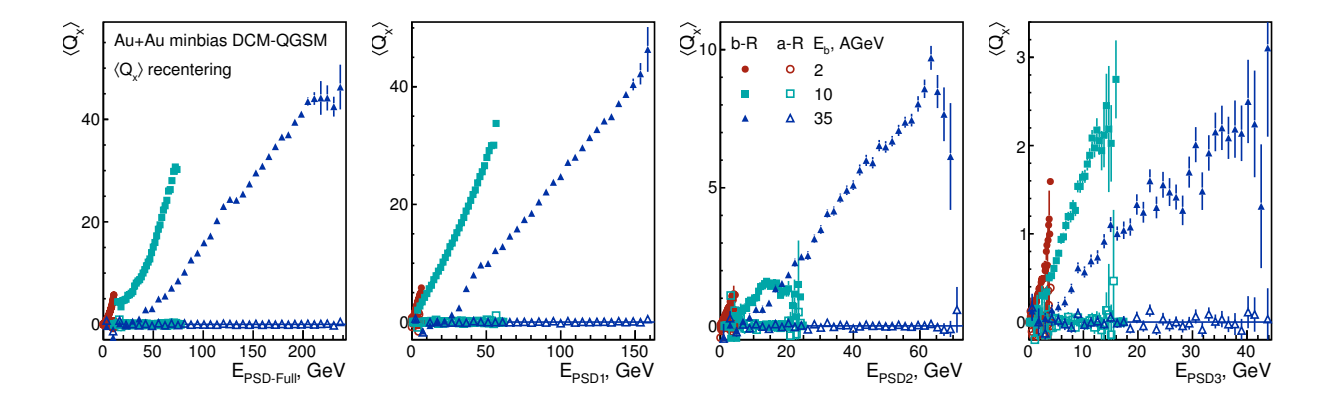


Fig. 11: Event averaged x component of the **Q**-vector, $\langle Q_x \rangle$, for different PSD subevents versus energy of the corresponding PSD subevents before (solid symbols) and after (open symbols) the **Q**-vector recentering procedure is applied. The panels (from left to right) show results using (a) full PSD information, (b) PSD1, (c) PSD2, and (d) PSD3 subevents. Different colors show results for $E_b = 2$, 10, and 35 AGeV. The PSD is positioned at 8 (15) m from the target at $E_b = 2$ and 10 (35) AGeV.

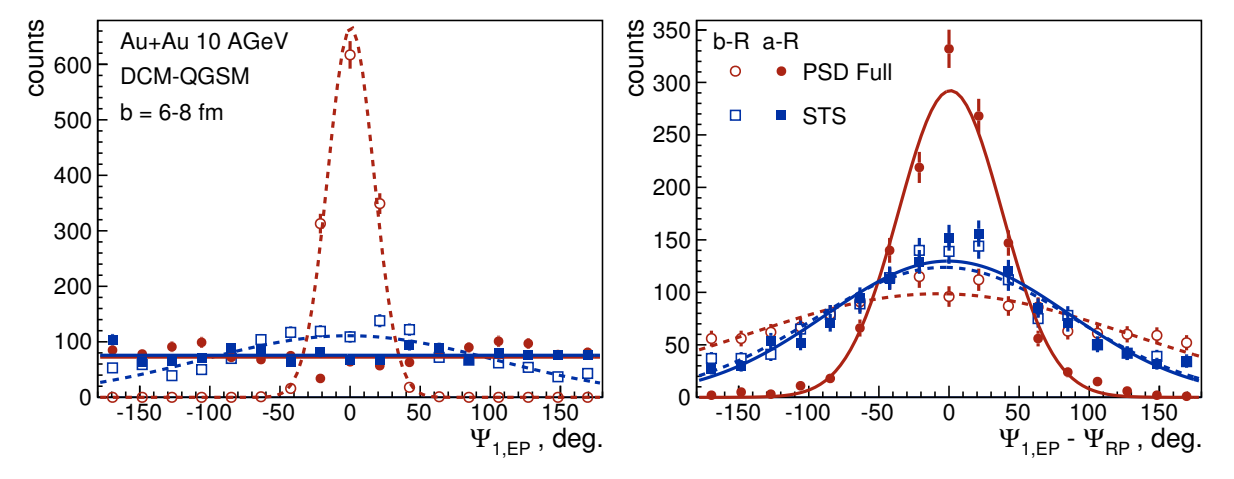


Fig. 12: Distribution of the first harmonic event plane angle, $\Psi_{1,EP}$, calculated with the full PSD and STS information for Au+Au collisions at $E_b = 10$ AGeV simulated with the DCM-QGSM model for b = 6 - 8 fm. The open (solid) symbols represent results before (after) the event plane recentering is applied (for performance of the recentering procedure see also Fig. 11). (left) $\Psi_{1,EP}$ distribution. Fits are shown to illustrate the performance of the recentering procedure. (right) Distribution of the difference between $\Psi_{1,EP}$ and the reaction plane angle, Ψ_{RP} . The width of Gaussian fits in the right panel (solid lines) illustrates the reaction plane resolution, $\sigma(\Psi_{1,EP} - \Psi_{RP})$, of the PSD and STS event planes. In this specific example the resolution of the PSD is about 36 degrees which is much better than that of STS (about 86 degrees).

5.5.2 Event plane resolution

Figure 13(left) shows the PSD event plane resolution, $\sigma(\Psi_{1,EP} - \Psi_{RP})$, for semi-central (20-50%) Au+Au collisions at E_b =2, 4, 6, 10, 15, 25, and 35 AGeV as a function of the PSD distance from the target in the range² between 8 m and 15 m. The PSD event plane resolution varies in the range of 30 – 40 degrees depending on the distance from the target and the collision energy, except of the lowest E_b of 2 AGeV for which the resolution is 40-60 degree. Results in Fig. 13(left) suggest that the optimal PSD location for SIS100 energies ($E_b = 2 - 10$ AGeV) is 8 m from the target. For SIS300 energies ($E_b \ge 15$ AGeV) the resolution is rather independent of the PSD distance to the target, but to use the advantage of the PSD subevents it is better to position the detector farther from the target. Figure 13(right) illustrates the effect of the magnetic field on the event plane resolution for the lowest beam energy $E_b = 2$ AGeV where distortion is expected to be the strongest. Simulations show no strong variation of the resolution after the recentering procedure is applied. Simulation results below are produced with the PSD positioned at 8 (15) m for SIS100 (SIS300) energies.

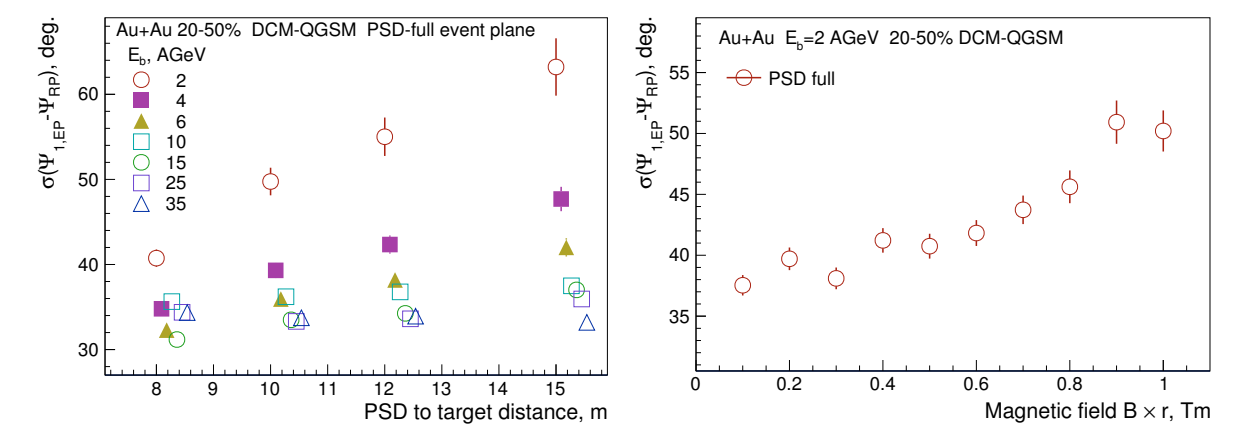


Fig. 13: First order reaction plane resolution, $\sigma(\Psi_{1,EP} - \Psi_{RP})$, for semi-central (20-50%) Au+Au collisions. (left) Results for E_b =2, 4, 6, 10, 15, 25, and 35 AGeV as a function of the PSD distance from the target in the range between 8 and 15 m. For better visibility the points are slightly shifted horizontally. (right) Effect of the magnetic field on the event plane resolution at the E_b = 2 AGeV. The PSD is located 8 m from the target.

Figure 14 presents the PSD performance for (left) the event plane resolution $\sigma(\Psi_{1,EP} - \Psi_{RP})$ and (right) the resolution correction factor, $R_{1,EP} = \langle \cos(\Psi_{1,EP} - \Psi_{RP}) \rangle$, for directed flow v_1 as a function of the collision centrality. The centrality is estimated from the STS multiplicity. The event plane resolution is as good as 25-40 degrees for mid-central collisions. The degradation of the resolution observed for central and peripheral collisions is a combined effect of the weakening of v_1 and the reduction of the fragment multiplicity in the PSD acceptance.

The reaction plane correction factors $R_{1,EP} = \langle \cos(\Psi_{1,EP} - \Psi_{RP}) \rangle$ and $R_{2,EP} = \langle \cos 2(\Psi_{1,EP} - \Psi_{RP}) \rangle$ required in Eq. 3 for the directed and elliptic flow measurement are shown in Fig. 15 as a function of the collision energy. The correction factors at $E_b = 10$ AGeV (and thus the PSD reaction plane resolution) well compare to that of the target (TCal) and participant (PCal) calorimeters used for v_1 and v_2 measurements in Au+Au collisions by the E877 experiment at AGS, which had a maximum of about $R_{1,EP} = 0.8$ ($R_{2,EP} = 0.4$) in mid-central collisions (see Fig. 5 in [36]). The results for the correction factors $R_{1,EP}$ and $R_{2,EP}$ for different PSD subevents vs. collision energy illustrate their usability for the data based estimation of the correction factor with three detector subevents technique [35].

²The minimum (maximum) distance of 8 (15) m from the target is constrained by the TOF detector (beam dump) location.

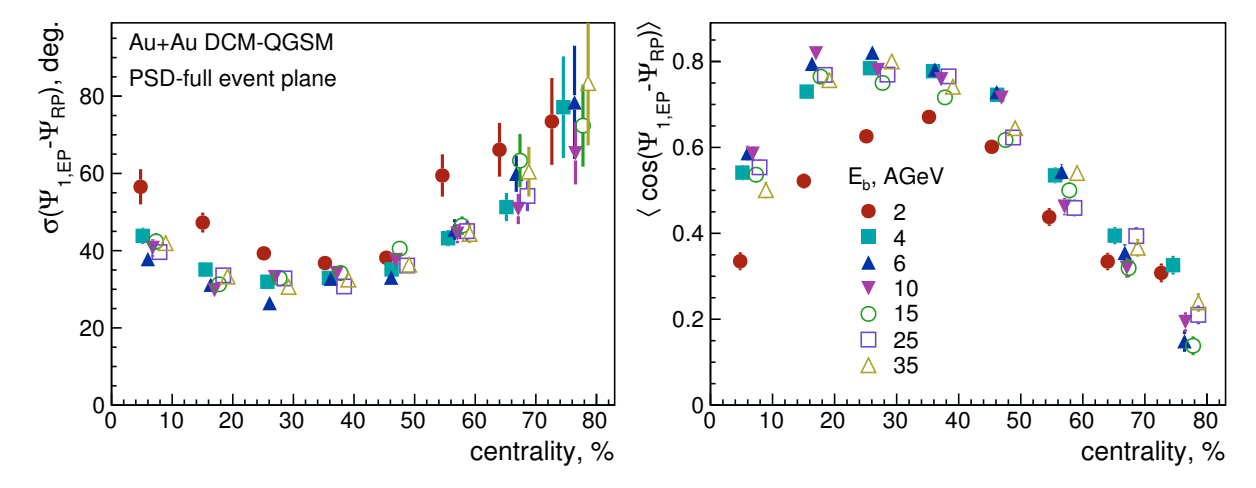


Fig. 14: (left) First order reaction plane resolution, $\sigma(\Psi_{1,EP} - \Psi_{RP})$ and (right) resolution correction factor, $R_{1,EP} = \langle \cos(\Psi_{1,EP} - \Psi_{RP}) \rangle$, plotted as a function of the centrality estimated with the STS detector for Au+Au collisions at E_b =2, 4, 6, 10, 15, 25, and 35 AGeV. The PSD is located at 8 m from the target for energies up to 10 A GeV, and at 15 m for higher energies. For better visibility the points are slightly shifted horizontally.

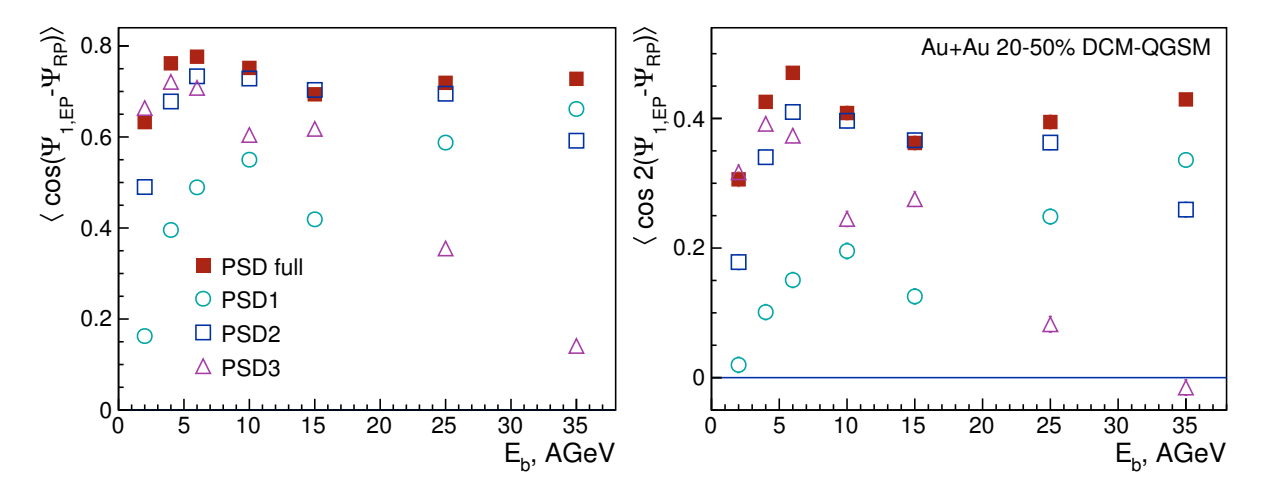


Fig. 15: First (left) and second (right) order reaction plane resolution correction factors, $\langle \cos(\Psi_{1,EP} - \Psi_{RP}) \rangle$ and $\langle \cos 2(\Psi_{1,EP} - \Psi_{RP}) \rangle$, as a function of the kinetic beam energy E_b for semi-central (20-50%) Au+Au collisions. To demonstrate the usability of the PSD for the data-driven event plane resolution determination a set of correction factors estimated with full PSD information and using three PSD subevents is shown. The PSD is located at 8 m from the target for energies up to 10 A GeV, and at 15 m for higher energies.

5.5.3 Comparison with other CBM detector subsystems

Fig. 16(right) shows the reaction plane resolution of the PSD as a function of beam energy calculated with the UrQMD event generator and the DCM-QGSM with an alternative GEANT4 physics lists QGSP_BIC_HP. All results are compatible with the default calculations using DCM-QGSM with FTFP_BERT physics list for GEANT4.

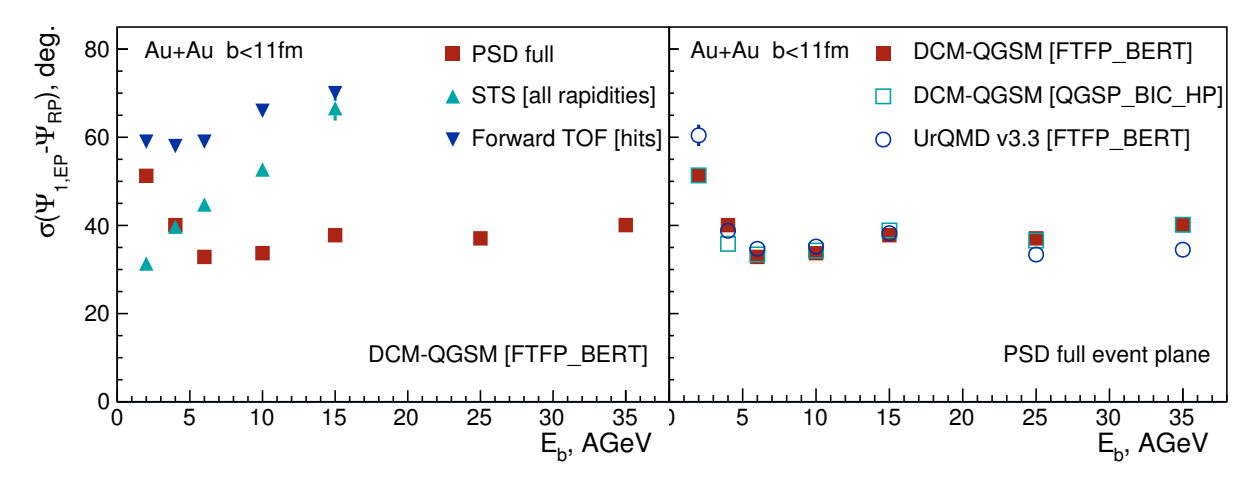


Fig. 16: Reaction plane resolution as a function of the beam energy in Au+Au collisions for impact parameter b < 11 fm. (left) Comparison between simulations with the DCM-QGSM event generator configured with two different physics lists (FTFP_BERT and QGSP_BIC_HP) and the UrQMD model. The PSD is located at 8 (15) m from the target at SIS100 (SIS300) energies. (right) Comparison between the event plane resolution of the PSD, STS, and forward TOF detectors simulated with the DCM-QGSM event generator. The results in both panels are obtained with x - y symmetric layout of the PSD modules in the transverse plane (which is different from the rest of results presented in this chapter), but this should not affect the conclusions made in Sec. 5.5.3.

The resolution of the reaction plane has been also determined for the STS and a forward TOF detectors. Results are shown in Fig. 16(left). For the STS, the charged particles in the detector acceptance were required to have at least 4 in the silicon tacking stations. The event plane resolution of the forward TOF wall is much worse compared to that of the PSD. This is mainly due to the lack of TOF sensitivity to neutral particles, which is a significant fraction of the spectators (see Fig. 8). The STS shows rather good resolutions up to $E_b \sim 4$ AGeV. Its performance degrades at higher energies due to the decreasing STS acceptance for particles produced with large v_1 at forward rapidity.

5.5.4 Elliptic flow performance

Figure 17 shows the proton v_2 in Au+Au collisions at $E_b = 10$ AGeV for b = 6 - 8 fm simulated with the UrQMD event generator. The results estimated in the data-driven analysis using PSD subevents for the event plane determination are in a good agreement with calculations based on Monte-Carlo truth information. The difference in the statistical error bars is due to finite event plane resolution of the PSD.

The results shown in Fig. 17 can be used to make projections of the statistical error bars for a given sample of Au+Au collisions for rarely produced particles. Below we provide such an estimate for the Λ and Ω^- hyperons. The Λ and Ω^- particles in Au+Au collisions at $E_b=10$ AGeV were extracted from the same UrQMD configuration as used in proton v_2 calculations. A KF-particle finder [37] was used to reconstruct particle tracks simulated with GEANT3 model of the CBM experiment via their topological weak decay channels, $\Lambda \to p + \pi^-$ and $\Omega^- \to \Lambda + K^- \to (p + \pi^-) + K^-$. Details of this analysis can be found in [38]. The acceptance of the CBM experiment for mid-central (b=5-8 fm) Au+Au collisions is illustrated in Fig. 18, which shows uncorrected double differential yield per event of proton, Λ , and

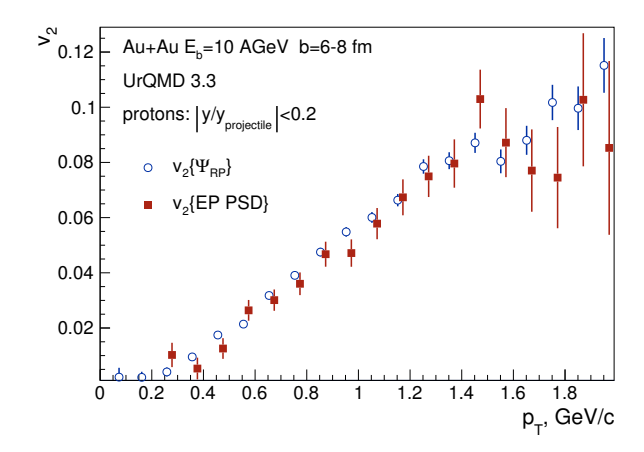


Fig. 17: Proton v_2 versus p_T reconstructed with the PSD event plane for one million Au+Au collisions generated with the UrQMD model. The proton v_2 calculated using the reaction plane orientation from Monte-Carlo, $v_2 \{ \Psi_{RP} \}$, is compared with its estimate, $v_2 \{ EP PSD \}$, based on the blind (real-data-like) analysis using only simulated detector signals and the PSD event plane. Protons were selected around midrapidity: $|y/y_{projectile}| < 0.2$.

 Ω^- vs. $p_{\rm T}$ and rapidity. Figure 19(left) compares the shape of the $p_{\rm T}$ yield of proton, Λ , and Ω^- reconstructed using CBM sub-detectors for $|y/y_{\rm projectile}| < 0.2$. Within statistical errors the shapes are rather similar except of $p_{\rm T} < 0.5$ GeV/c. For the v_2 error projections we can assume a common shape of the $p_{\rm T}$ yield and use the scaling factors shown in the legend of Fig. 19(left) as an estimate of the relative yields between proton, Λ , and Ω^- .

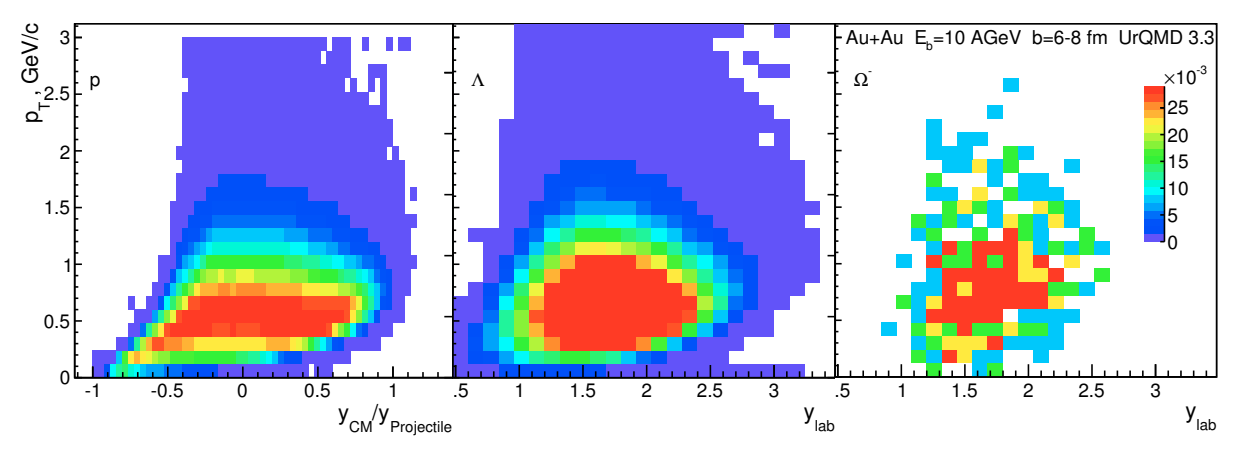


Fig. 18: Proton (Λ and Ω^-) double differential yield per event vs. p_T and center of mass rapidity normalized to $y_{\text{projectile}} = 1.57$ (lab rapidity, y_{lab}). Panels (from left to right) show yield of proton, Λ, and Ω^- . Results are for Au+Au collisions at $E_b = 10$ AGeV with b = 6 - 8 fm simulated with the UrQMD v3.3 event generator.

We used the following equation for error projections based on proton v_2 simulations with one million Au+Au collisions shown in Fig. 17 (projected relative error vs. p_T is denoted as $r\Delta_{v_2,X}(p_T)$):

$$r\Delta_{\nu_2,X}(p_{\rm T}) = \frac{\Delta_{\nu_2,p}(p_{\rm T})}{\nu_2^p(p_{\rm T})} \times \sqrt{\frac{Y_X(p_{\rm T}) \times N_{ev}^X}{Y_p(p_{\rm T}) \times N_{ev}^p}} \ . \tag{8}$$

Here:

- $\Delta_{v_2,p}/v_2^p(p_T)$ is the relative statistical error of the proton v_2 at a given p_T (taken from Fig. 17);

- $-N_{ev}^{p}$ is the number of events used for v_2 calculations (one million);
- $-Y_p(p_T)$ is the reconstructed proton yield per event vs. p_T (open squares in Fig. 19(left));
- $-N_{ev}^X$ is the number of events expected for particle X (proton, Λ , or Ω) projection;
- $-Y_X(p_T)$ is the reconstructed X particle yield (proton, Λ , or Ω) per event vs. p_T from Fig. 19(left).

Equation 8 assumes that v_2 of particle X (Λ and Ω) is similar to proton v_2 at the same p_T (e.g. radial flow will affect this assumption). We also neglect the uncertainties due to combinatorial background in the reconstruction of the Λ and Ω^- yields from the corresponding invariant mass distributions. According to our simulations, the typical signal to background ratio for Λ (Ω^-) in Au+Au collisions at $E_b = 10$ AGeV is about 20% (50%).

Figure 19(right) shows projections for relative statistical errors on v_2 for Ω^- (proton and Λ) for a sample of 10^{11} (10^{10}) minimum bias Au+Au collisions at $E_b=10$ AGeV which is equivalent to about two months of CBM experiment operation at 1 MHz (100 kHz) interaction rate. These results demonstrate that by using the PSD detector for the event plane determination, v_2 of Ω (Λ and proton) particles can be measured with precision of about 20-40% (0.3-1%) in the transverse momentum range between $p_T=0.5-2 \text{ GeV/}c$ after a few months of CBM experiment operation at 1 MHz (100 kHz) interaction rate.

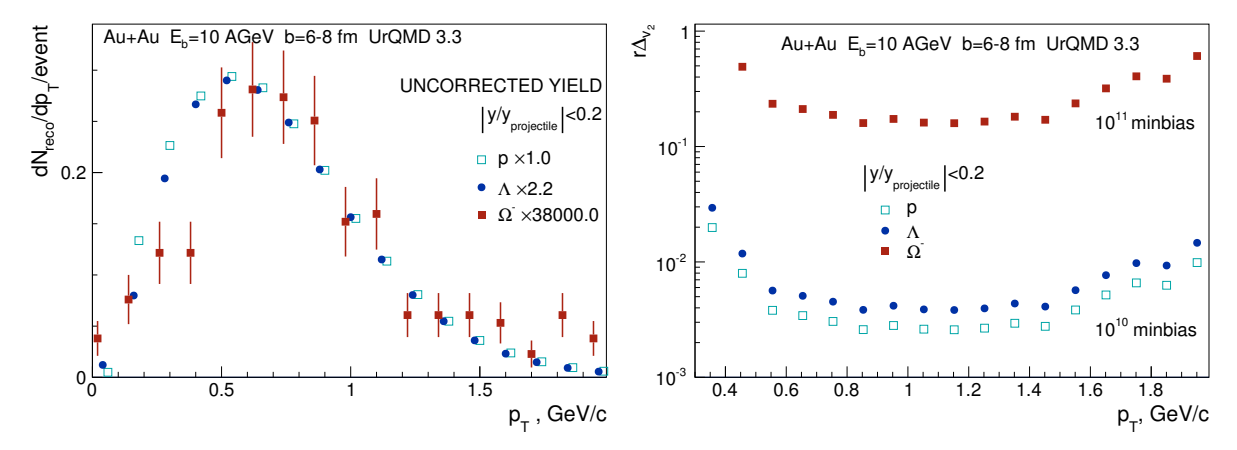


Fig. 19: (left) Proton, Λ, and Ω p_T -yield per event. Particles were selected around midrapidity: $|y/y_{\text{projectile}}| < 0.2$. Points are slightly shifted horizontally for visibility. (right) Relative statistical errors for v_2 of Ω (Λ and proton) in mid-central Au+Au collisions (b = 6 - 8 fm) projected for 10^{11} (10^{10}) minimum bias Au+Au collisions.

6 PSD components

6.1 Module structure

To study the reliability of the proposed PSD concept an intensive R&D work has been performed in the recent years on the technical design of lead-scintillator sandwich calorimeters. Within this activity, small modules with the transverse size $10 \times 10 \text{ cm}^2$ and large modules with the transverse size $20 \times 20 \text{ cm}^2$ have been built. Detailed studies of the calorimeter module response in the hadron energy range from a few GeV up to 160 GeV have been performed. In addition, a mechanically stable construction for the sandwich-like modules with thin walls needed for a hermetical calorimeter has been developed. Another goal was the development of a method for the light readout from the scintillator tiles that provides good efficiency and uniformity of light collection. The proposed scheme of the PSD module and the light readout is shown in Fig. 20. Each module of the hadron calorimeter consists of 60 lead-scintillator tile sandwiches with lead and scintillator tiles of 16 and 4 mm thickness, respectively. The sampling ratio of 4:1 satisfies the compensation condition.

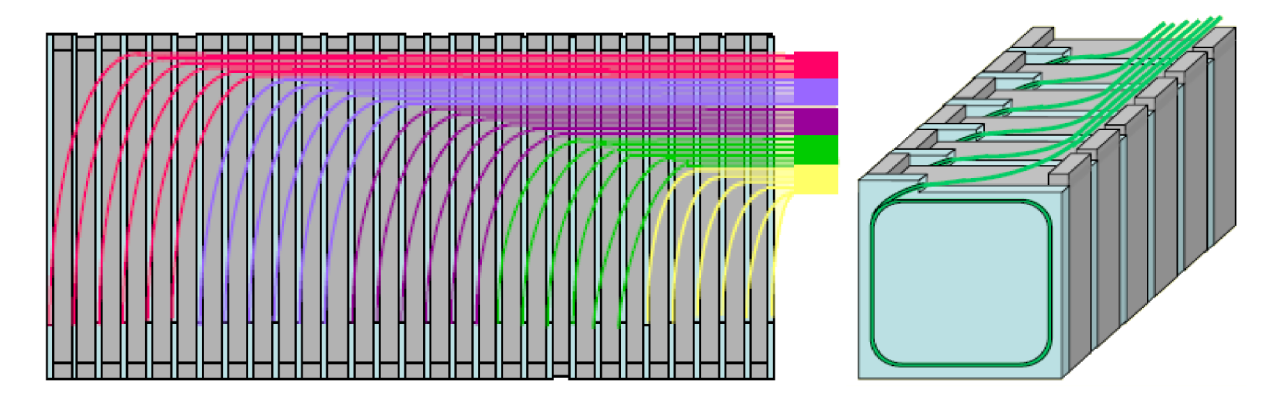


Fig. 20: Design of the PSD module and light readout from scintillator tiles in PSD module. Left - front view, right-top view (only half-length of the module is shown). Fibers from each consecutive 6 tiles are collected together and read out by a single MAPD.

The light readout is provided by WLS-fibers embedded in round grooves in scintillator plates that ensure a high efficiency and uniformity of light collection over the scintillator tile within a very few percent. The WLS-fibers from each 6 consecutive scintillator tiles are collected together and viewed by a single photodetector at the end of the module. The longitudinal segmentation in 10 sections ensures the uniformity of the light collection along the module. The individual calibration of longitudinal sections is essential for monitoring the drop in light yield caused by the radiation dose absorbed in scintillator tiles during the CBM operation with high intensity ion beams. Longitudinal segmentation of the calorimeter provides also a unique opportunity to improve the energy resolution based on the measurement of the longitudinal hadron shower profile with the off-line compensating algorithm. For example, the WA1 collaboration improved the energy resolution of an iron/scintillator calorimeter by about 30% with the deposited energy weighting procedure [39]. Taking into account a very similar longitudinal segmentation of the PSD and the WA1 calorimeter, one can expect similar effects for the PSD energy resolution. The development of such an off-line compensating algorithm is a challenging task for the improvement of PSD performance.

The readout of the longitudinal segmentation of the calorimeter modules requires 10 compact photodetectors coupled to the end of WLS-fibers at the rear side of the module. The use of micropixel avalanche photodiodes (MAPDs) or silicon photomultipliers (SiPMs) seems to be an optimal choice due to their remarkable properties like high internal gain, compactness, low cost and immunity to the nuclear counter

effect.

6.1.1 Mechanical design

All 60 layers of lead-scintillator sandwiches in each module are packed into a box made of 0.5 mm stainless sheet and tied together in one block with a length of about 120 cm (about 6 nuclear interaction lengths) by a 0.5 mm stainless steel tape. This tape and the lateral sides of the box are spot-welded together. The WLS-fibers from each of 60 scintillator tiles are stretched in a 3 mm air gap at the top side of the module. Each WLS-fiber is covered by a thin black pipe for light isolation and mechanical protection. Each 6 consecutive WLS-fibers from one section are collected in one optical connector at the end of module and polished to ensure the optical contact with the MAPD. Additionally to the six WLS-fibers one clear fiber from the monitoring system is glued into the same optical connector. The other ends of the 10 clear fibers are connected together and illuminated by a light emitting diode (LED). Such a simple system allows constant monitoring of the readout elements. The entire structure is covered by another stainless box, and both boxes are spot-welded providing a mechanically stable module. The weight of each small module with transverse size 10×10 cm² is about 125 kg. The main sequence of the module assembling is demonstrated in Fig. 21. Nine modules of this type have been constructed during the first R&Ds studies.



Fig. 21: Main assembling sequence of a small module. All layers of the lead-scintillator tiles are in the stainless box (left upper) and each WLS-fiber is placed in a thin black pipe for the light isolation and the mechanical protection (right upper). Then, the WLS-fibers are stretched in a 3 mm air gap at the top side of the module (left down). Six consecutive WLS-fibers and one clear fiber are glued inside the optical connector and polished (right down).

A set of 28 large modules with the transverse sizes $20 \times 20 \text{ cm}^2$ and weight of about 500 kg have been

constructed for the NA61 experiment at CERN. Technical drawings of the module construction are available. One of the modules has been used for beam tests in the energy range 2-6 GeV relevant for the CBM operation. A picture of an assembled large module without upper cover box is shown in Fig. 22. This large module is the main element of the PSD for the CBM experiment. In total, 45 large modules are required for the CBM calorimeter.



Fig. 22: Photo of an assembled large module.

6.1.2 Scintillator tiles, wave-length shifting fibers, and lead plates

The basic parts of the module are the scintillator tiles with WLS-fibers and the lead plates. The scintillator tiles with 4 mm thickness were made of polystyrene based scintillator produced in Kharkov (Ukraine). They have 1.1 mm depth groove at the surface of the scintillator plate (Fig. 23), where the WLS-fiber is glued by the optical glue Bicron-600. Each scintillator tile is covered by a white reflector (TYVEK paper) to improve the light collection. The shape of the grooves provides parallel exit of WLS-fiber from the groove relative to the upper side of the scintillator.

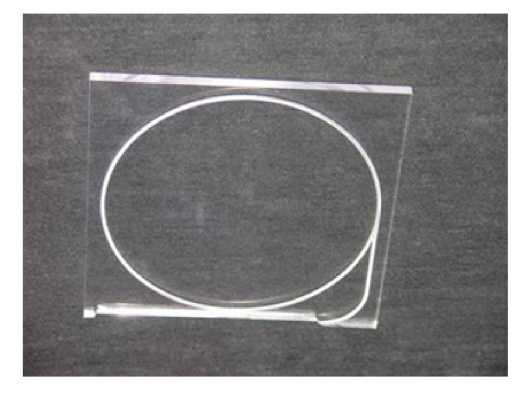


Fig. 23: Photo of a scintillator tile.

The WLS-fibers Y-11(200) with double cladding and a diameter of 1 mm produced by Kuraray Co. were used for the PSD prototype assembling. The light attenuation length of this fiber is about 4.5 m [40]. The lead plates are of 16 mm thickness, and are of the same shape as the scintillator plates. The lead contains about 3% of antimony to increase its hardness.

The radiation dose at SIS100 (SIS300) energies reaches about 300 (700) Gy near the beam hole (see Sec. 7.4) which does not change significantly the properties of scintillators and WLS-fibers. The detailed studies of the radiation hardness of the similar elements for calorimeters were performed at the LHCb experiment [41]. The degradation of scintillator tiles and WLS-fibers was examined for different doses both for electromagnetic and hadron calorimeters. The dimensions of the scintillator tiles in LHCb hadron calorimeter are very similar to that of CBM PSD. The WLS-fibers of the LCHb calorimeter make optical contact only with the lateral side of the tiles, while the PSD fibers are embedded into the scintillator. Consequently, the transparency degradation of the scintillator is rather critical for the LHCb calorimeter, but not for the CBM PSD. The relative light yield of the LHCb tiles reduced by 25% after 2.5 kGy irradiation, and then slowly degrades by another 20% for irradiation up to 14 kGy.

Taking into account the considerations discussed above one can conclude that the effect of the radiation dose on the PSD calorimeter is not significant. The transverse and longitudinal uniformity of the PSD light collection does not degrade due to the modular structure and the longitudinal segmentation. Permanent amplitude calibration allows the correction of the light yield drop without the degradation of the energy resolution.

6.1.3 Light readout with micropixel avalanche photodiodes

An important decision in the development of the PSD is the choice of the photodetectors to read out the WLS-fibers. These photodetectors must be rather compact such that a set 10 pieces fits on the $20 \times 20 \text{ cm}^2$ rear side of the module. Immunity to the nuclear counter effect and the acceptable cost are also key requirements for these readout elements.

The avalanche photodiodes (APDs) are successfully used in the electromagnetic calorimeters and have a well defined and reliable parameters. At the same time, the low (50-100) gain of the APD requires a sophisticated amplifier and limits its capability to detect low intensity light at the level of ten photons. The light yield of hadron calorimeters is an order of magnitude smaller than the one of electromagnetic calorimeters. This limitation is essentially critical for the calibration of the calorimeter by minimum ionizing particles with the low energy deposition.

Avalanche photodiodes with micropixel structure are of special interest because of their remarkable properties [42, 43]. micropixel avalanche photodiodes (MAPDs or G-APDs) are rather new devices that are under intensive developed and used in modern research projects [44–47]. Each pixel in MAPD might be regarded as an individual photodiode creating the avalanche in a limited Geiger mode with an internal gain up to 106. The MAPDs have a very small size for the scale of a few millimeters. The pixel structure of the MAPDs eliminates the nuclear counting effect and makes then sensitive to single photoelectrons with excellent amplitude resolution even for a signal of a few photoelectrons. To summarize, the main advantages of the G-APDs are very compact size, low bias voltage, gain comparable to PMT, relatively low price, insensitivity to magnetic field and absence of the nuclear counter effect.

A sketche of two different G-APD types is shown in Fig. 24. The main feature of the first type is that groups of p-n cells (pixels) are connected to metal electrodes via individual surface resistors (see Fig. 24 (left)). The standard MAPD technology with individual surface resistors has a strict limit on number of pixels/mm² due to the dead areas around each individual pixel. This limitation is relevant for calorimeter design, as it limits its dynamical range. Monte-Carlo simulations described below show that the detected energy in single section of the PSD module may reach a few GeV. Taking into account the light yield of 2-3 photoelectrons per MeV, the maximum signal in one section would consist of

a few thousands photoelectrons. This is true if the number of fired pixels (photoelectrons) would be proportional to the number of initial photons. In reality, the limited number of pixels, N_{total} , leads to the nonlinear dependence of the number of fired pixels, N_{fired} on the number of photons, $N_{photons}$:

$$N_{fired} = N_{total} (1 - \exp\{-N_{photons} \times PDE/N_{total}\}). \tag{9}$$

Using this formula one can estimate the minimum number of pixels needed for the desired energy range. To ensure a linear MAPD response for the case of $3 \times \text{mm}^2$ MAPD the pixel density must be up to $10000/\text{mm}^2$. The G-APDs with surface resistors have a pixel density of about $1000/\text{mm}^2$ which is certainly not sufficient. In order to increase the dynamical range one has to use MAPDs with higher pixel density. Such MAPDs have been developed based on the deep micro-well technology where the pixels

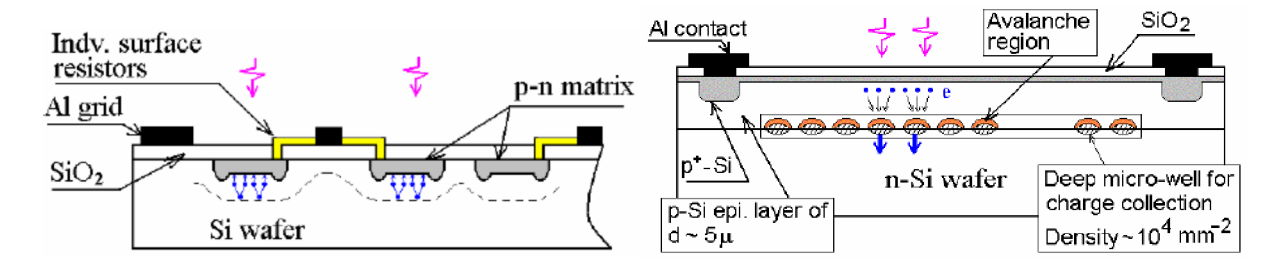


Fig. 24: Different structures of the G-APDs with (left) individual surface resistors and about 1000/mm² cells (pixels), and (right) deep micro-wells with the pixel density of 15000/mm².

are placed inside the wafer (Fig. 24, right). These MAPDs with pixel density up to 20000/mm² were initially developed by JINR (Dubna, Russia) in collaboration with the Mikron Company (Zelenograd, Russia). This technology was successfully applied by Zecotek Co. [48] and in other R&D projects [49, 50].

6.2 Readout electronics

The PSD detector is based on a lead-scintillator sandwich structure. A particle traversing a lead-scintillator sandwich structure of the PSD module deposits in the scintillator an energy of about 5 MeV per MIP. The generated scintillation light is guided via wavelength shifting fibers to a light read-out device (MAPDs) for further signal processing. The measured gain of the MAPDs is about 5×10^4 , which requires an additional signal amplification by a factor of about 50. The rapid progress in MAPDs development with respect to gain, linearity and time resolution gives hope for a higher gain in the near future. The signal properties of the MAPDs are similar to the ones for scintillators, and can be characterized by a rise time of about 10 ns, and a signal width of about 60 ns. To fulfill the requirements of the physics program an overall detector time resolution of about 1 ns is requested. Thus, electronics with an intrinsic time resolution of a few 100 ps-200 ps should be provided.

The energy deposited in the PSD has to be measured with a resolution of about $50\%/\sqrt{E(\text{GeV})}$. To fulfill these requirements an intrinsic energy resolution of the electronics better than 1% is sufficient. There is no space limitation for the readout electronics and the total number of detector channels is relatively small (about 500) which allows to use for readout scheme commercially available components. Recent technological progress in Field Programmable Gate Array (FPGA) makes possibiple to realize the signal discrimination, charge and time digitization all inside FPGAs. These capabilities have been demonstrated in prototype devices [51].

The readout concept proposed for the PSD detector is schematically shown in Fig. 25. The main com-

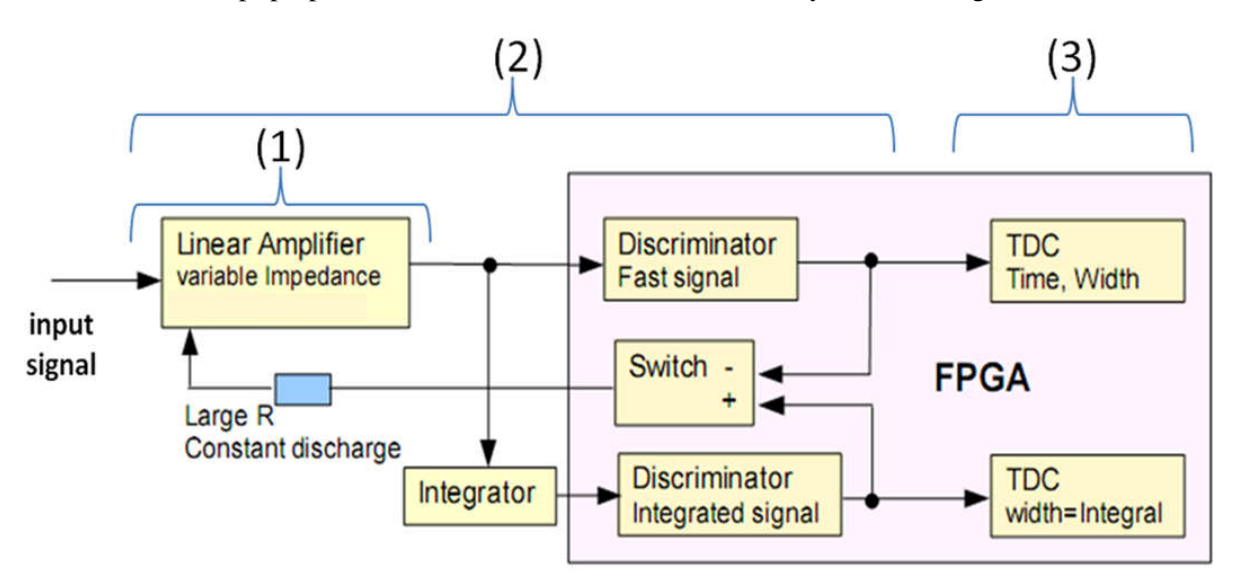


Fig. 25: A sketch of the readout system for the PSD detector. Signals after amplification (1) are processed in the charge digitization system (2) followed by the time digitization circuit (3) which consists of two branches, one for fast timing and the second one for a pulse-width measurement which encodes the charge (two TDC channels are needed for one detector input channel).

ponents of the system are: (1) an amplifier with amplification factor of about 50, (2) the charge and (3) time digitization circuits implemented inside the FPGA. Two multi-hit high resolution TDC channels are needed for one detector channel.

6.2.1 Amplifier

The amplifier has to deal with relatively small input signals from MAPDs and should have a gain of about 50. Peaks time of about 6-8 ns and 50 Ohm input impedance should ensure good intrinsic time

resolution of the read-out system.

6.2.2 Charge digitization

The charge digitization circuit is based on a modified Wilkinson ADC. An amplified inverted signal, integrated by means of employing a capacitor, is injected at the input via a discriminator-driven switch. The integrator discharges linearly using a current source. In this way a fast crossing of the threshold can be achieved with better charge precision compared to a RC-discharge method. Discharging the integrator by applying a constant current over a time interval until the pulse charge is fully compensated serves as an automatic baseline-restorer. It is important to keep the baseline rather constant. After discharging the integrator, the device is immediately ready to process the next signal.

A prototype board with 4 channels which employed only discrete components has been developed. Figure 26 shows the board and the response of the system to the two different input signals. The signal of

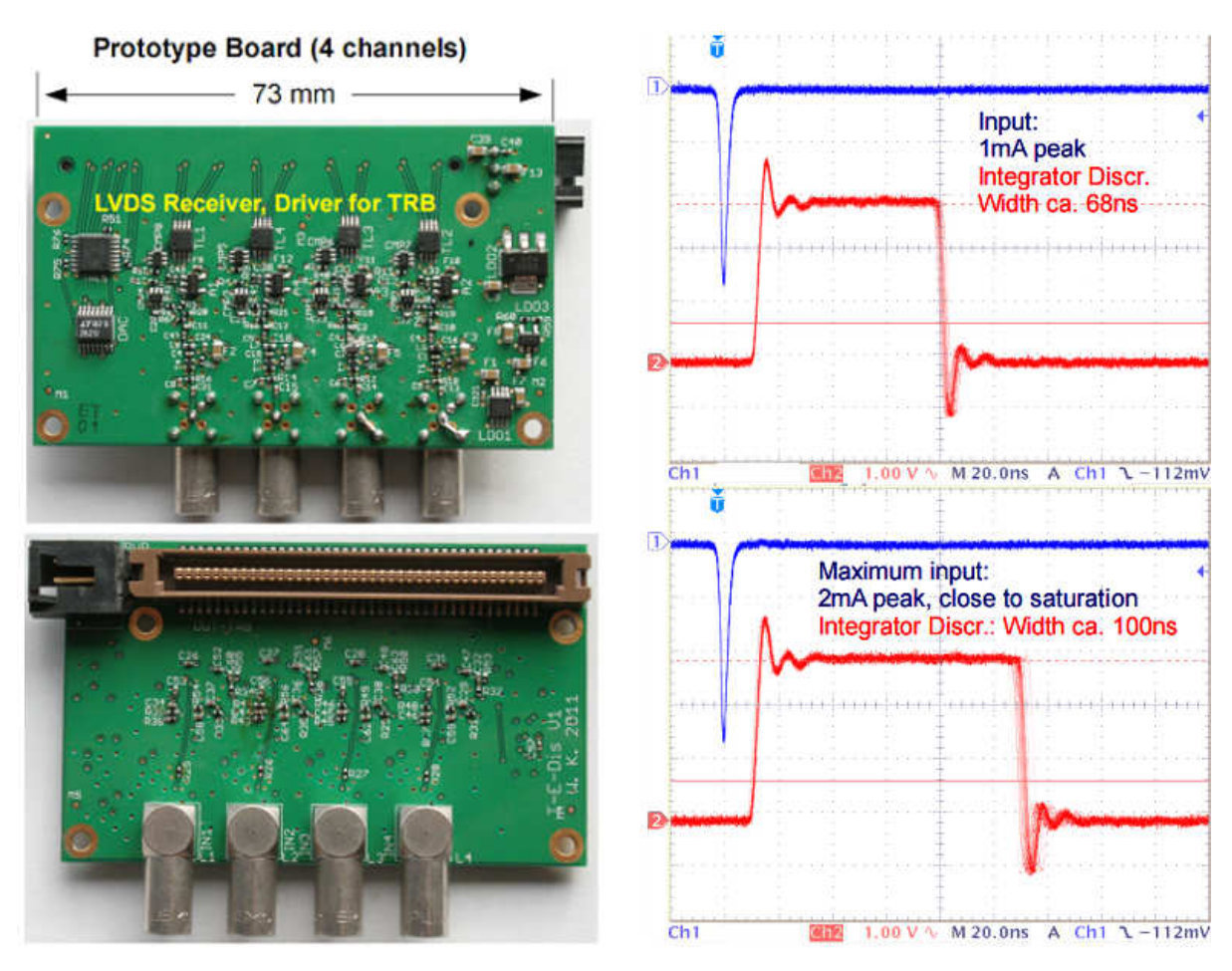


Fig. 26: (left) An image of the front (lower panel) and back (upper panel) sides of the prototype board. (right) The pulse width of 1 (2) mA signal is seen as \sim 68 (100) ns (see upper and lower panels).

about 1 (2) mA is seen as a peak with a width about 68 (100) ns. The chosen parameters of the integration circuit constrain the rate capabilities of a single channel. By selecting the integration time the parameter signals can be integrated in time shorter than 200 ns. This gives the rate capability for single channel of about 1 MHz which fits the PSD detector requirements.

6.2.3 Time-to-digital converter

The last element of the readout system is a fast, multi-hit TDC. The PSD solution is based on the newly developed Time Digitalization in FPGAs. A prototype TDC board which implements a Tapped Delay Line method equipped on several FPGA chips has been built [52]. An excellent performance of the TDC with time resolution of 17 ps RMS has been demonstrated. Based on this, a versatile digital readout board has been developed [53]. The main functionality of the board is the high resolution TDC realized in FPGAs. The board is also equipped with high bandwidth DAQ functionality with data transfer capabilities up to several hundred MByte/s. It can handle up to 256 detector channels which makes it perfectly suited for the PSD detector.

A prototype system of the charge digitization has been tested with pulser signals with rising (falling) times about 1.5 (2.5) ns and read out by multi-hit TDCs. Results of the test are shown in Fig. 27. A large

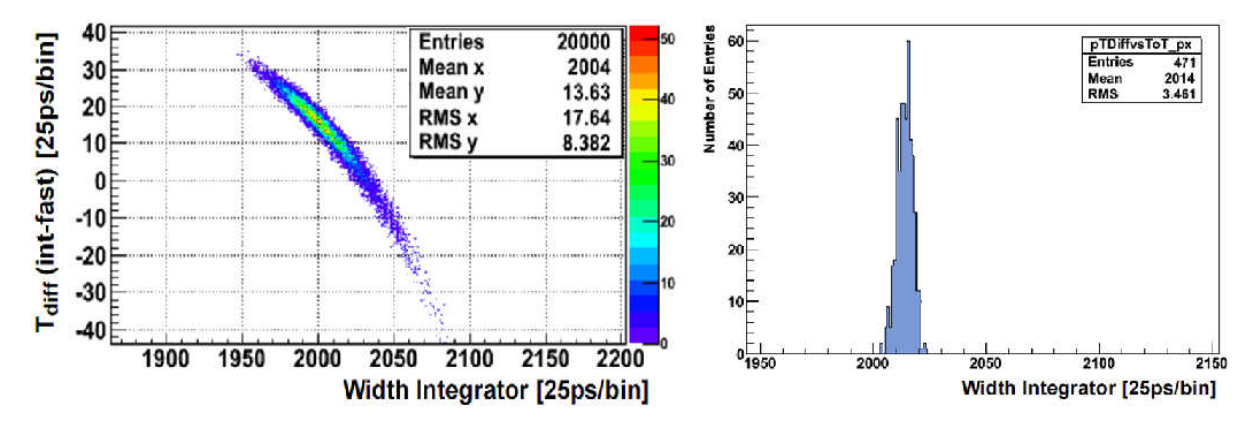


Fig. 27: Test results of the charge digitization circuit prototype built on discrete elements. (left) The measured width of the pulse signal in a multi-hit TDC. (right) The intrinsic charge resolution of 0.17% is achieved after applying the walk correction procedure.

jitter of the integrator width (charge) has been observed due to high gain of the system for low frequency noise. This effect is seen in Fig. 25(left). The effect can be easily measured and corrected for, as shown in Fig. 27. After walk correction a charge resolution of about 0.17% has been achieved. This value is by far better than needed for the PSD application and validates the use of FPGA-based read-out electronics for the PSD detector.

All components shown in Fig. 25, i.e. discriminators, a switch and TDCs, will be implemented in a FPGA which includes storage pipes for interfacing the readout to a common or a standalone data acquisition system.

6.3 Energy calibration techniques

The energy calibration of the hadron calorimeters represents a difficult task due to complexity of the shower development in several detector modules consisting of a number of independent cells. Not only the analog signal response from each cell has to be calibrated, but also the shower reconstruction has to be well understood to achieve a decent absolute energy calibration. Several methods mentioned below in combination with a simulation of the full process are needed. At the same time, the time stability of the calibration has to be monitored during the experiment, as the analog signal readout devices (in our case APDs) as well as digitization devices (ADCs) are both sensitive to the changes of temperature and other parameters. The proposed calibration methods are discussed in detail e.g. in [54].

There are several ways how to monitor the calorimeter response which are described below.

6.3.1 Radioactive source

This is a usual way of the hadron calorimeter calibration. A radioactive source (e.g. ⁶⁰Co) is moved using a remote control system along all detector parts, and the response is measured. This is not very suitable for the PSD detector, as most of modules are not accessible. Still it can be used for part of the detector, and compared with other methods.

6.3.2 LED light

The advantage of the LED light is that it can be easily tuned by width and intensity of the electrical pulse. The width of the pulse can be chosen to be close to the width of the light pulse produced by shower (about 10 ns) and the intensity in the suitable range to cover the dynamic range of the shower response in the cell. As shown in [55], very good resolution of SiPMs and linearity at low light intensities enable to resolve single photon peaks and provide a unique opportunity to calibrate SiPM gain by a fit with a linear combination of Gaussian functions. We will apply this method to our case of the MAPD readout.

6.3.3 Cosmic muons

Cosmic muons are a natural choice for the hadron calorimeter calibration, and they are used in all installed setups. In the case of the PSD, a dedicated cosmic trigger system will be constructed. The most suitable setup is shown in Fig. 28. It consists of an array of 20 scintillator plates, 10 placed horizontally

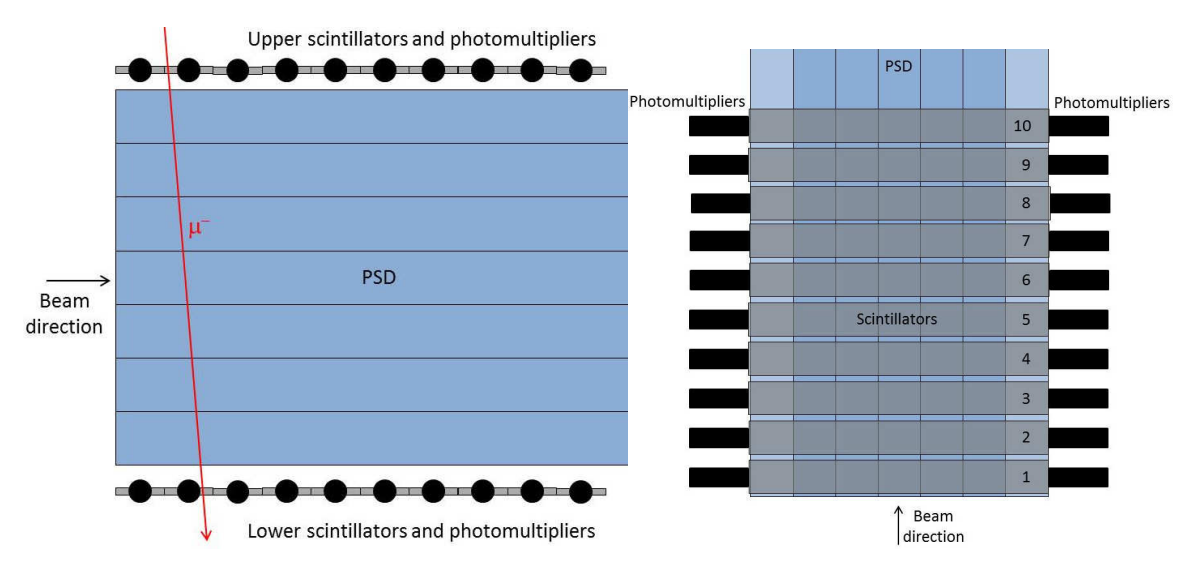


Fig. 28: The schematic setup of the cosmics trigger scintillator array. Left: side view, Right: top view.

above and 10 below the PSD detector. The dimensions of each plate will correspond to the size of one PSD module: 140×12 cm with thickness of 2 cm. Each plate will be read-out by 2 PMTs, one on each side of the plate. After processing the signal from PMTs through the discriminator, a simple trigger logic will provide overlap coincidence of 4 signals from PMTs corresponding to the plate positioned above and below the PSD, determining the vertical direction of cosmic muons. Logic OR of such 10 signals will be a resulting trigger signal.

Due to a rather large distance of the top and the bottom plates (about 1.5 m) the trigger count rate will be rather small of the order of 1 Hz. Therefore, a long acquisition time of the order of days will be needed. On the other hand, the data will be very clean and noiseless. The response to the cosmic muons (passing in vertical direction) corresponds to one to few MIPs from target (passing PSD in horizontal plane), and it is suitable to a relative calibration of all PSD sections.

For the tests of the calibration system, a special prototype of the PSD module was assembled. It consist of only one section of the PSD module described in Chapter 6.1, i.e. a 12 cm long sandwich consisting of 6 layers of scintillator and lead. The advantage of the prototype is its flexibility, it can be easily moved and/or rotated, thanks to its relatively low weight of about 60 kg. The prototype is shown in Fig. 29.



Fig. 29: Prototype of one section of the PSD module.

For the measurement of cosmic muons, the simple setup was arranged with two trigger scintillators of suitable size placed above and below the active section, see Fig. 30. The coincidence signal from two scintillators provided a trigger signal for DAQ, with frequency of about 10 counts per min. A Voltcraft PPS-12008 power supply was used as a HV supply for the MAPD optical sensor. The signal from the MAPD was processed by a fast amplifier described in Sec. 6.2.1, and the resulting pulse-height distribution was collected by a Yokogawa DL9240L oscilloscope.

At the described conditions, the cosmic muons penetrate the PSD scintillators with a path length in the range of 16-200 mm (depending on their declination), which results in a rather wide ADC spectrum, see Fig. 31.

To simulate various gains of the APD and the FE module, we measured the response to cosmic muons at four different HV settings of 89.4 V, 90.0 V, 90.8 V and 91.0 V. The measurement time was several hours for each setting. The resulting pulse-height distributions are displayed in Fig. 31. In addition, the similar measurement of cosmic muons was done with the PSD module at "vertical" position, when muons penetrate approximately a constant path of 24 mm (same as detected spectators in the real CBM experiments), see Fig. 32.

From the comparison of the results of the measurements with the PSD module at "horizontal" and "vertical" positions (see Fig. 33(left)), one can deduce that the averaged mean path at the described setup is

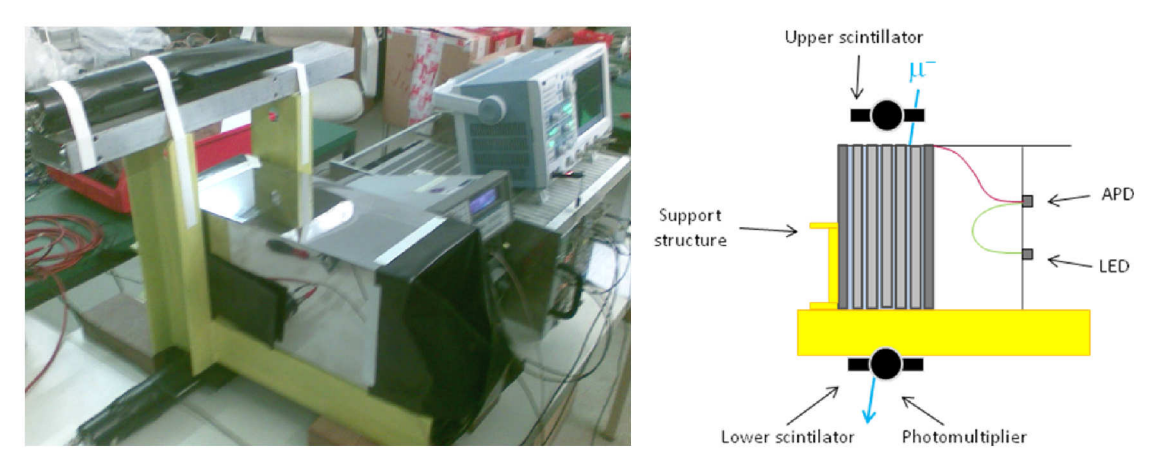


Fig. 30: Horizontal cosmic setup.

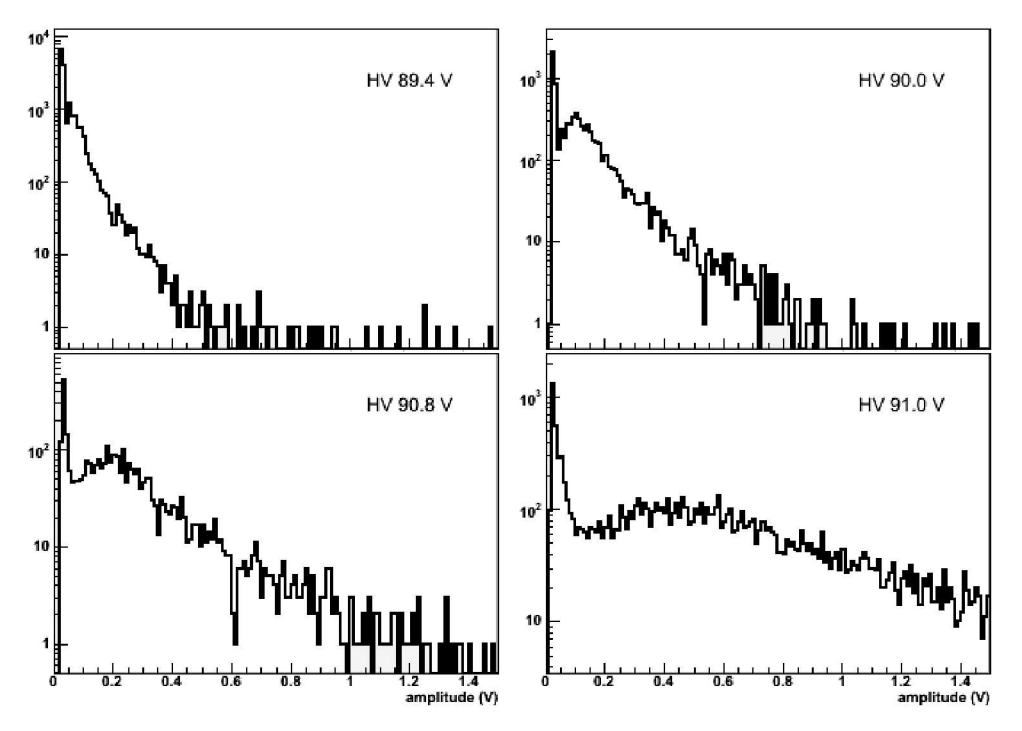


Fig. 31: Measured pulse-height distributions for cosmics muons at 4 different HV settings.

about 20 mm.

Then a simple minimizing method to determine the relative difference of the read-out gain based on the MINUIT-ROOT software was applied. The pulse-height distribution from one run, in our case the run at 90.0 V, was selected as a reference. The measured pulse-height values from a different run were multiplied by a constant factor k, then they were filled into a histogram with the same binning and size as data from the reference run, and finally the histogram was renormalized by the second factor (to account for different accumulated statistics). The result of minimization for all three sets of data ended successfully with $\chi^2/\text{n.d.f.}$ close to 1. The scaled distributions are shown in Fig. 33(right), with the resulting scaling factors k shown in the legend. The errors of the k factor determination i.e. precision of this calibration method are 2-3%.

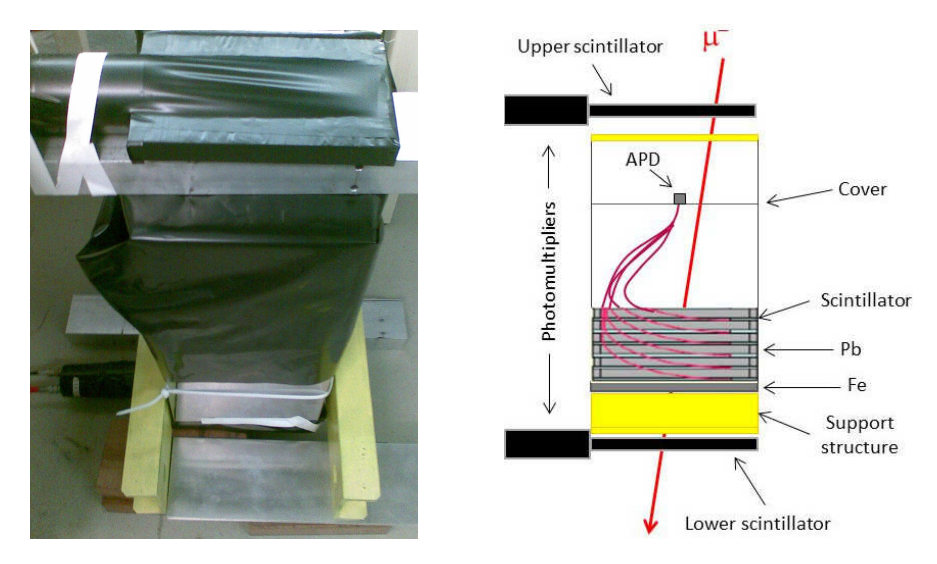


Fig. 32: Vertical cosmic setup.

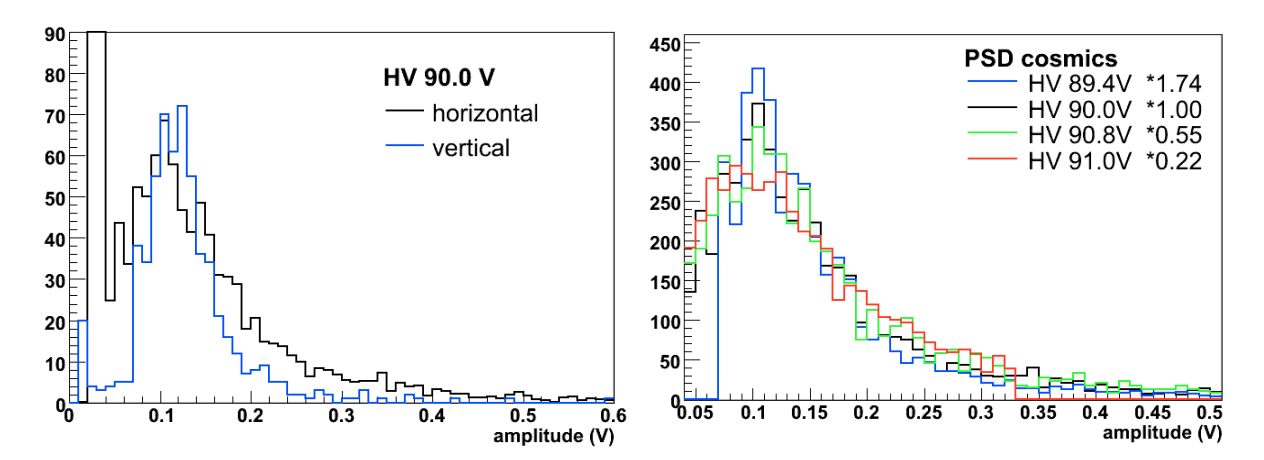


Fig. 33: (left) Measured pulse-height distributions for cosmics muons at two different setups (see text for details). (right) Pulse-height distributions for cosmics muons at 4 different HV settings, scaled to the same gain as the data at 90.0 V.

6.3.4 Secondary decay muons

Muons from secondary decays of pions produced in the primary reaction will penetrate the detector. Similar as in case of cosmic muons, these data cannot be used to study the absolute energy scale calibration because their energy is not accurately known, but can be efficiently used for the relative calibration and test of the stability. For the muon triggering we propose to use the PSD response in the PSD cells most distant from target, and/or ratio of the responses from several cells. The preliminary calibration using other methods is needed. This method is unfortunately usable only for modules which are more distant from the beam pipe where the occupancy due to projectile spectators is rather low.

6.4 Control and cooling systems

The gain of the PSD photodetectors (MAPDs) is very sensitive to both the applied bias voltage and the environmental temperature. Therefore, a serious attention must be paid to the stability of MAPD gains. For this purpose a PSD control and cooling system was developed. The gain monitoring system includes the controlled power supply for MAPDs and the generator of stabilized light pulses. For each MAPD the voltage is provided by the individual photodiode power unit mounted on the printed circuit board near the photodetectors and managed by a separately placed common controller. The power supply provides voltage in the range 60-70 V with accuracy about 10 mV. The maximum current through each MAPD is $30 \mu A$.

For the continuous monitoring of the photodiode gains a LED generator of stabilized light pulses has been designed. It includes a pulse generator, a LED driver, a built-in PIN-photodiode, a QDC and a microcontroller (see Fig. 34). The main part of the LED light is transferred through the optical clear fibers to 10 individual MAPDs in the module, while a small part of the LED light is detected by a PIN-photodiode and digitized by a QDC. To ensure the stability of the light pulse the QDC value is permanently compared with the reference number. In case of a deviation between the QDC and the reference values the microcontroller changes the LED driver amplitude in a proper way. The available stabilized light pulser allows the long-term monitoring of the MAPD amplitudes, and, consequently, the MAPD gain variations.

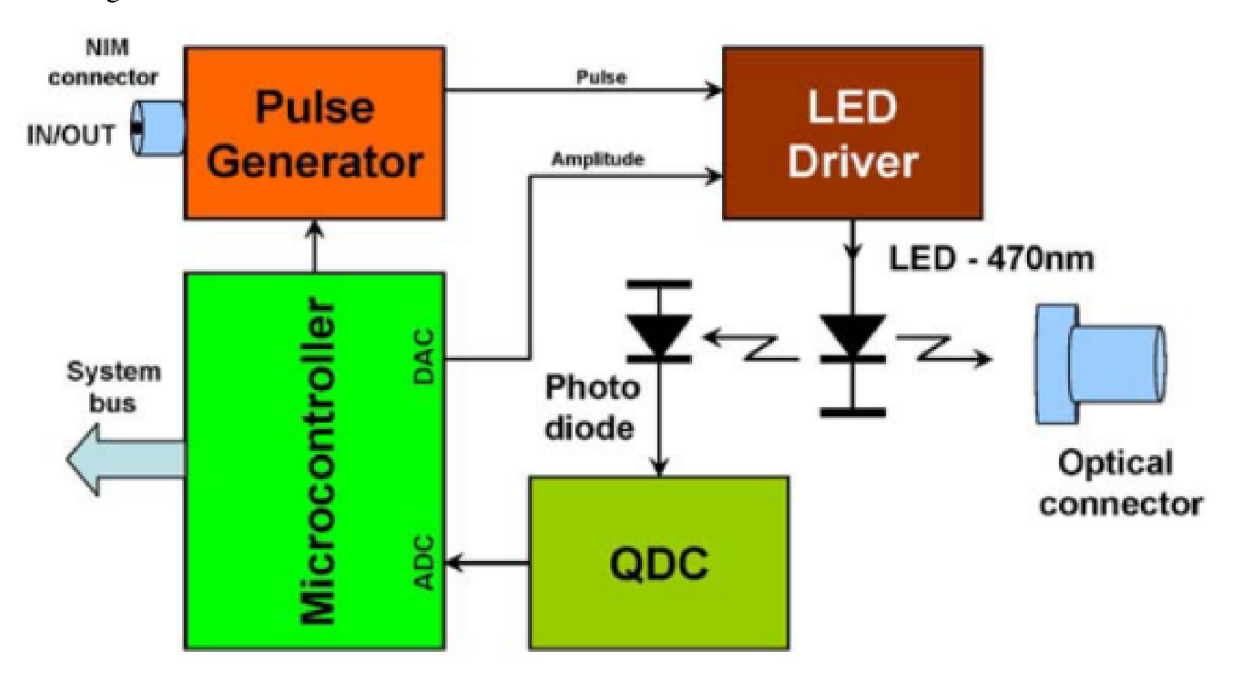


Fig. 34: Schematic diagram of the stabilized light source.

Special attention should be paid to the MAPDs temperature stabilization, because, as mentioned in Chapter 6, the test MAPDs used for the prototype calorimeter have a gain temperature coefficient of about $4\%/^{\circ}C$. (Note, that recent SiPMs samples have a coefficient below $1\%/^{\circ}C$.) Obviously, the temperature of the photodiodes in each module must be stabilized and controlled with an accuracy of about 0.1 degree. To fulfill this requirement the cooling system based on Peltier elements has been developed. The cooling scheme is shown in Fig. 35. The photodiodes of one module are mounted on the aluminum plate that provides the common thermal contact for all 10 photodiodes in the module. This plate is cooled by a Peltier element with a size of $30\times30~\text{mm}^2$. One side of the Peltier element is glued by heat conducting adhesive to the small copper plate which is connected by short copper rods (diameter 6 mm) to the other large copper plate glued to the aluminum plate. This copper rod passes through the holes in the

centers of the electronic boards. The large copper plate is placed in the gap between the two rows of photodiodes mounted on the aluminum plate. All open surfaces of aluminum and copper plates, as well as the copper rod are carefully thermally insulated by armaflex. The temperature of the aluminum plate with the attached photodiodes is measured by the temperature sensor, placed on the same plate. Another temperature sensor is mounted on the heat sink, which is glued to the other (hot) side of the Peltier element. For more efficient cooling compressed air is blown onto the sink. The current through the Peltier element and the temperature values provided by 2 t-sensors are read out by a TEC-controller [56].

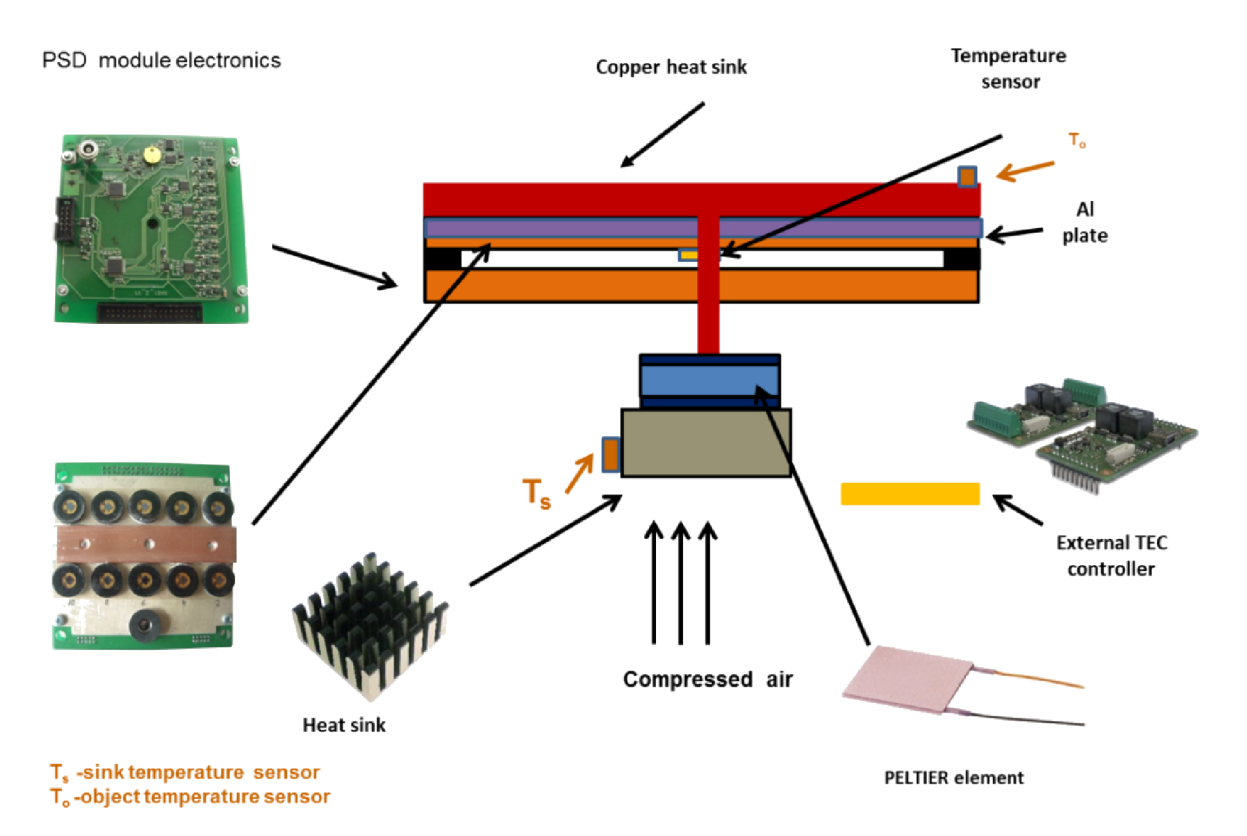


Fig. 35: Schematic view of the assembled electronics and cooling system based on the Peltier element.

A photo of the assembled electronics with cooling and temperature stabilization system is shown in Fig. 36(left). The panel with the installed TEC controller is shown in Fig. 36(middle). The location of 10 photodiodes mounted on an aluminum plate is shown in Fig. 36(right). The copper plate is adhered to an aluminum plate between two rows of photodiodes. All the exposed parts are isolated by armaflex.

The control electronics with the cooling system is placed in the calorimeter module to provide the optical contact of MAPDs mounted on the aluminum plate to the respective optical connectors. The Fig. 37 demonstrates some results of test measurements of long-term stability of the cooling system. The left panel of Fig. 37 shows the change of room temperature as a function of time (during 24 hours of continuous measurements). The room temperature varies during the measurement between 19.5 and 20.5 degrees. The temperature of the aluminum plate with the photodiodes was set to $17^{\circ}C$ by the TEC controller. The variation of the temperature recorded during 24 hours by the t-sensor on the aluminum plate is shown in the right panel of Fig. 37. It is seen that the average temperature is 17 degrees, and the width is less than 0.1 degrees.

The data demonstrate that the cooling system provides the requested long-term temperature stabilization of photodiodes. The methods are developed for the cooling and control systems of the PSD calorimeter in the CBM experiment.

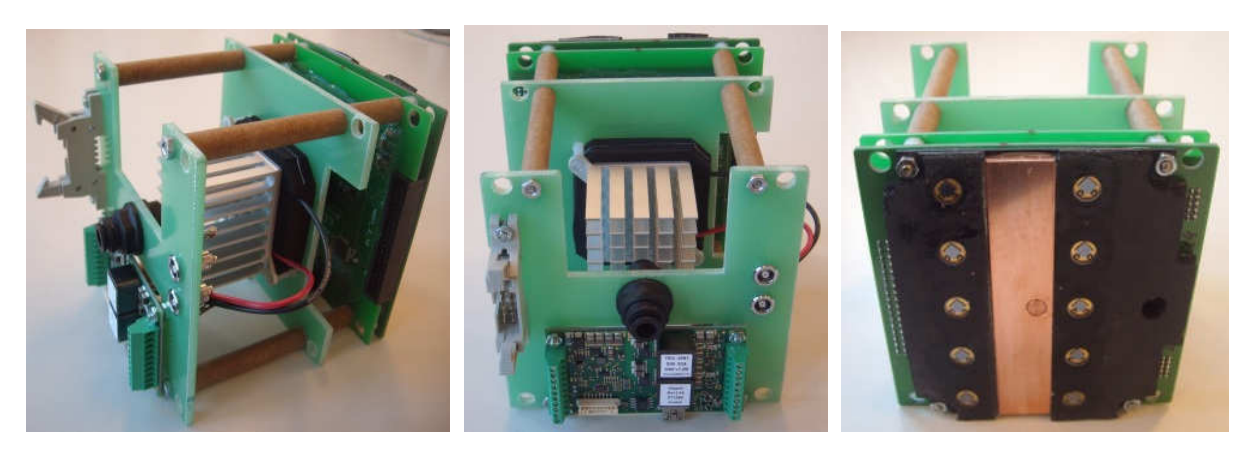


Fig. 36: (Left) An image of the assembled prototype electronics, cooling and temperature stabilization system for one calorimeter module. (center) An image of TEC controller on the panel. (right) A view of the front aluminum plate with 10 MAPDs. The copper plate is visible in the middle of two MAPDs rows.

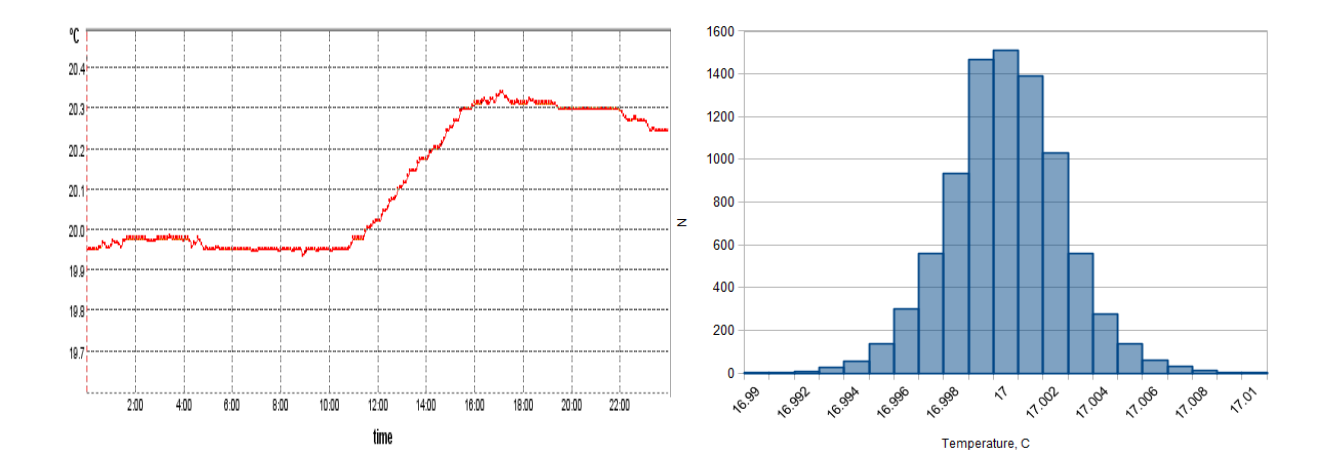


Fig. 37: Left panel: the room temperature as a function of time (during 24 hours of continuous measurements). Right panel: the temperature variation measured by the t-sensor on the aluminum plate.

6.5 Mechanical support

The PSD calibration with beam particles (protons and muons) requires the positioning of each individual module at the beam axis. Therefore, the movable platform is necessary to move the 22 t calorimeter in the transverse directions with precision of a few millimeters. In this case the vacuum pipe inside the calorimeter should be disconnected from the beam pipe during the calibration. The platform could be similar to one used in NA61 experiment (see Fig. 58(right) of Sec. 7.2). The platform remote control system must be elaborated to perform the PSD movement from the counting room without beam interruption.

7 PSD components R&D

7.1 Module prototype tests

Several beam tests of small and large modules have been performed at the CERN H2 and T10 beam lines since 2007. The response of various prototype calorimeter modules, and of an array of 3×3 small modules (supermodule) has been studied using proton and pion beams at energies from 2 GeV-158 GeV. The obtained results are discussed in this section.

7.1.1 Small module response

The first beam test of a small prototype PSD module with MAPDs readout was performed at the SPS H2 beam line at CERN in 2007. Special FEE electronics for beam tests has been developed. The electronic board is shown in the Fig. 38, it includes a HV-divider for 10 MAPDs and 10 amplifiers.

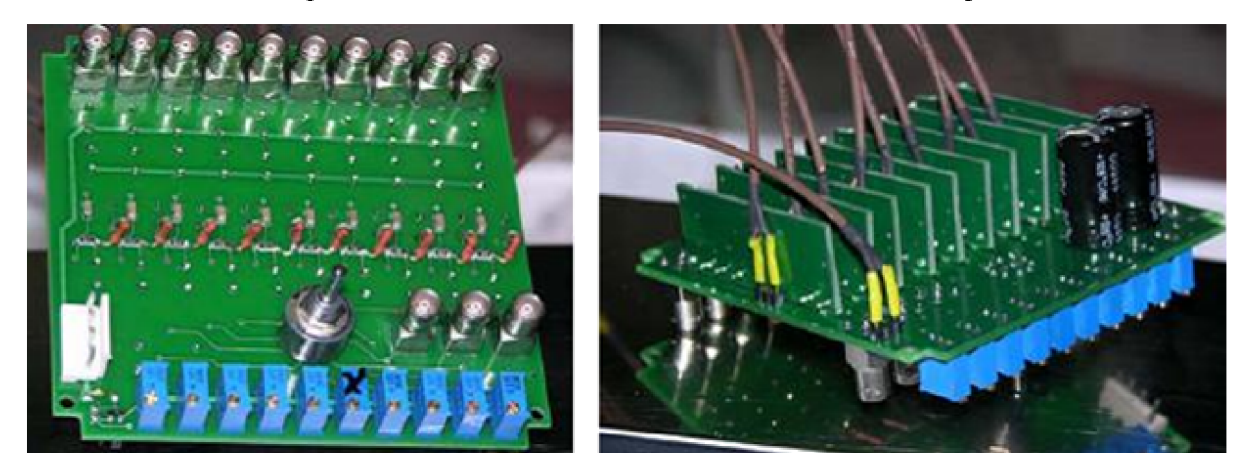


Fig. 38: Top and rear side view of the electronic board of the module.

The circuit scheme is shown in Fig. 39. The common high voltage +150 V (Fig. 39, left) is applied to a current divider via a transistor-based protection scheme. The current divider uses 10 trimmer resistors

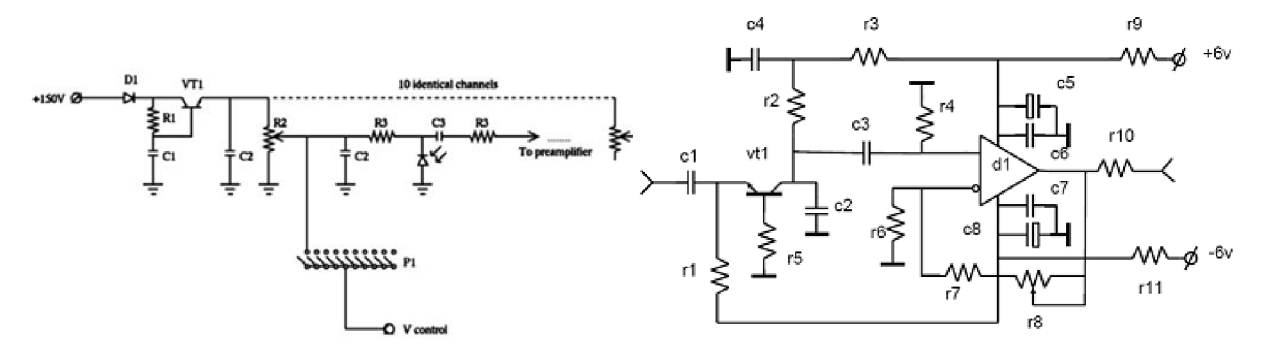


Fig. 39: Scheme of the front-end electronics for the test of the PSD modules. (left) HV divider for MAPDs. (right) The amplifier.

R2 connected in parallel for the individual adjustment of the bias voltage at MAPDs. This voltage is applied through the R3 resistor to the cathode of the MAPD. The gains of the diodes were equalized within 50% by setting the MAPD's noise levels at the same level. A more accurate adjustment of the gains with a precision of 10-20% was performed during the calibration of the modules with a muon beam. Depending on the MAPD sample, the bias voltage ranges from +125 V to +145 V. The signal from the

diode output enters the amplifier through the capacitor C3. In case of abrupt switch on/off of the input voltage (+150V), the protection smooths the rapid voltage change avoiding a possible voltage shock of the amplifier. The control of the bias voltage is performed with the help of the P1 switch connected to the LEMO connector, where the voltage can be measured by the voltmeter.

The MAPD signals need an additional amplification by a factor of 40 because of the relatively low MAPD gain of about 5×10^4 . A set of 10 independent current amplifiers is mounted at the inner side of the electronic board. The amplifier input impedance is about 55 Ohm. The bandwidth is 35 MHz. The dynamical range of the amplifier is about 5 mV - 3.5 V. The size of the electronic board is 95 mm² which is well matched to the rear side of PSD module. The signal amplitudes after amplification have been readout with 10-bits standard LeCroy 2249A ADC modules.

During the beam test the calibration of all 10 readout channels was performed with the muon beam at an energy of 75 GeV. The typical ADC spectrum (after pedestal subtraction) obtained from muons in one section is shown in Fig. 40. The peak of the ADC spectrum corresponds to the light yield of about 10

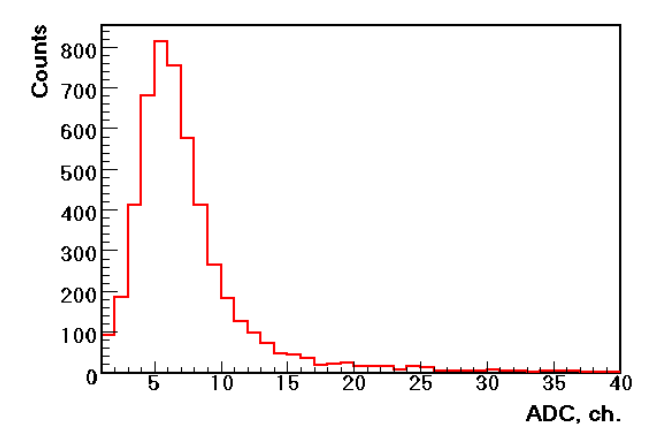


Fig. 40: ADC spectrum from muon signals in one section of the PSD module.

photoelectrons per MIP or 2 photoelectrons per MeV. The obtained light yield is higher by one order of magnitude compared to the previous generation of hadron calorimeters without WLS-fiber readout.

After the calibration, the energy deposition from the pions with an initial energy 150 GeV was measured in each of the 10 sections which reflect the longitudinal profile of the hadron shower. Fig. 41 shows the energy deposition in different sections of the PSD module. The shapes of the measured energy distributions are in good agreement with the MC predictions.

In Fig. 42 the total deposited energy in a PSD module is shown for a few pion beam energies. The energy depositions in all sections were summed up with the appropriate normalization coefficients obtained from the calibration with muon beam. The experimental distributions (solid lines) are slightly wider than the MC predictions (dashed lines). During this test the beam profile in front of the module was not controlled, and the spread of the beam position may be responsible for this discrepancy. At least, the observed small offset of the 50 GeV peak might be explained only by the shift of the beam spot with respect to the module center.

During this beam test the readout electronics performed excellently. No problem with the module operation occurred. The light yield was high enough to perform the energy calibration of the PSD calorimeter with minimum ionizing particles and cosmic muons.

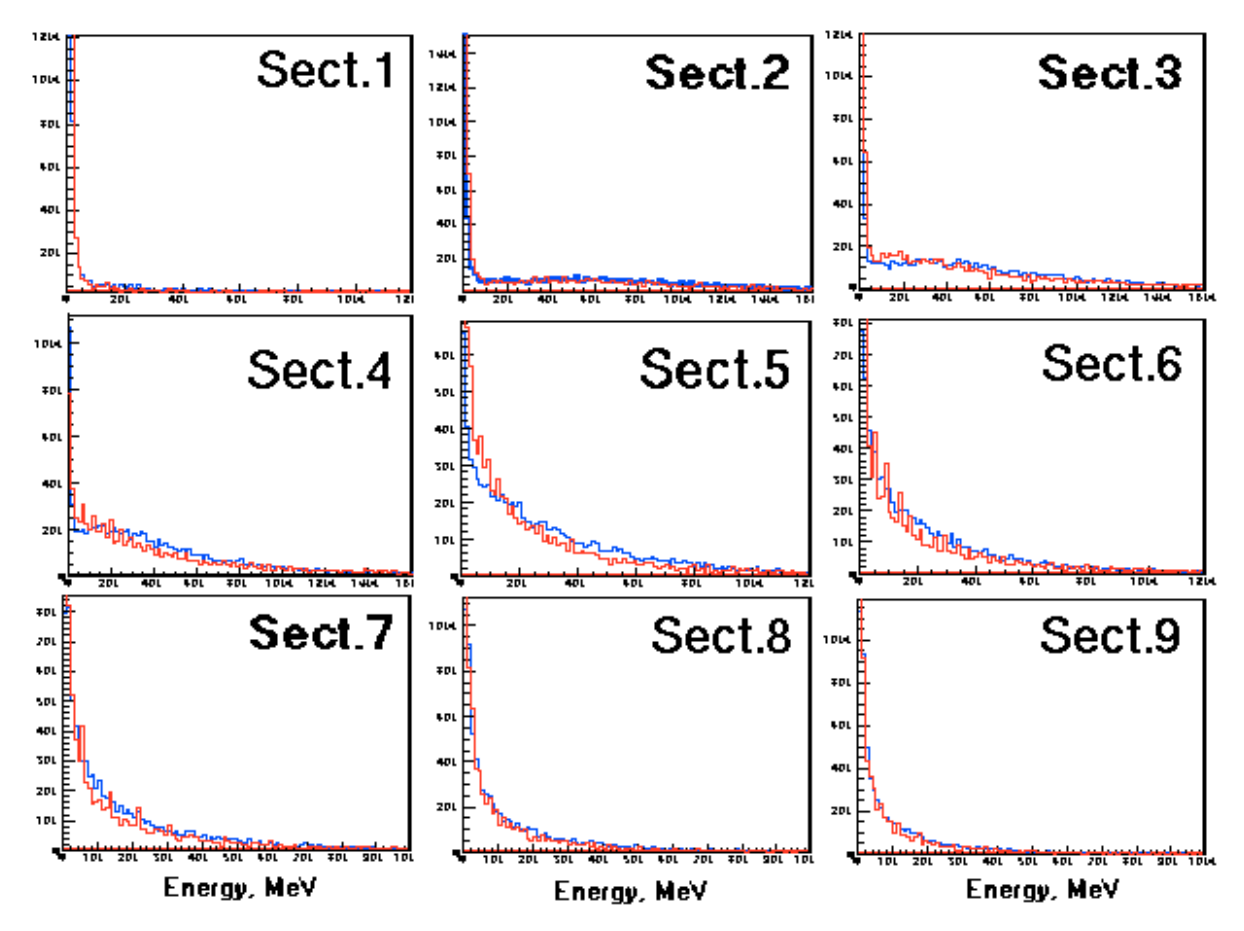


Fig. 41: The energy spectra in different sections of PSD module. Red line-experimental distribution for 150 GeV pions, blue line-Monte Carlo simulations for 150 GeV pions.

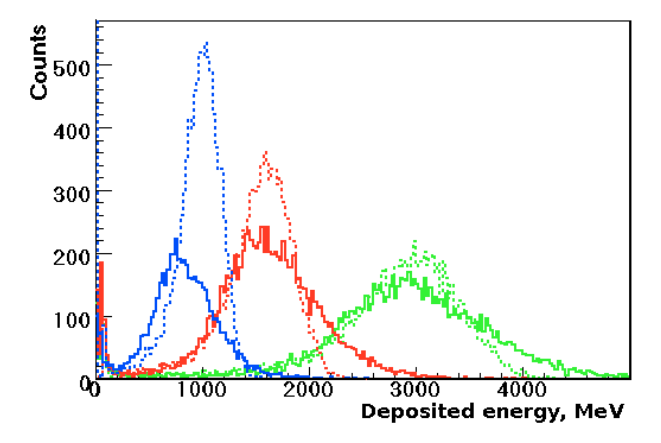


Fig. 42: Sum spectra of deposited energies in PSD module for different pion beam energies: 150 GeV (green), 80 GeV (red), 50 GeV (blue). Solid line - experimental distributions, dashed line - MC predictions.

7.1.2 Supermodule response to high energy pions

The next step of the PSD R&D was the experimental study of the most important parameters of the calorimeters such as energy resolution, linearity of the response and longitudinal shower distributions. These properties have been studied with the new 3×3 array (supermodule) of the PSD modules. All 9 small modules with transverse size 10×10 cm² were constructed at INR (Moscow) and assembled in a 3×3 array (Fig. 43, right) to transport it to CERN. The yellow frame was used to protect supermodule from the damage during the transportation.





Fig. 43: Fully assembled module (left) and assembled supermodule (right) before the transportation to CERN.

The supermodule was installed on a movable platform at the SPS H2 beam line (Fig. 44). All 9 modules were equipped with the same FEE and readout electronics as in the first beam test. The test of the PSD supermodule was performed with muon and hadron beams.



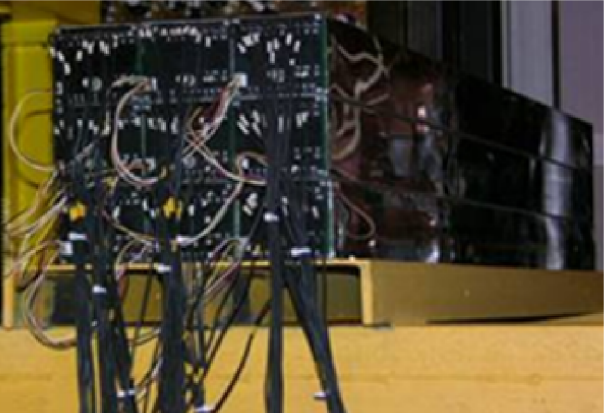


Fig. 44: The position of the PSD supermodule at the SPS H2 beam line.

The large light yield of the scintillator tiles read out by MAPD's allows the detection of low amplitude signals, and the use of the muon beam for the energy calibration of longitudinal sections in the calorimeter. As shown in Fig. 45, the 5 MeV peaks in one module section are nicely separated from the pedestals. To obtain a full set of calibration coefficients, the muon beam scan was performed for all 9 modules. After that the central module of the calorimeter was irradiated by a pion beam at four different energies: 20, 30, 40 and 158 GeV. Unfortunately, at this beam test we did not use the beam definition counter in front of the supermodule. Therefore, the beam position was controlled indirectly by comparing the energy deposition in the peripheral modules. Of course, this method has a rather limited accuracy.

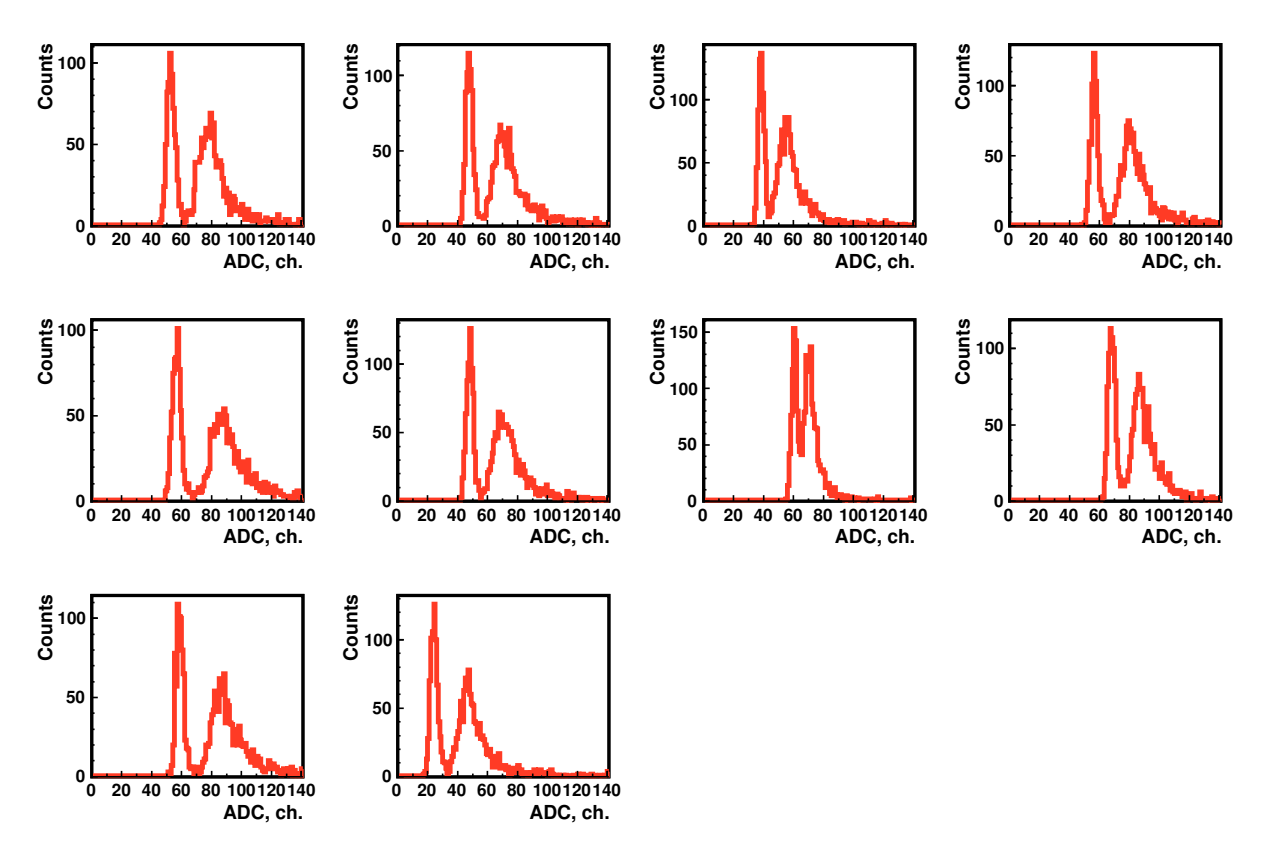


Fig. 45: Amplitude spectra for all 10 sections in one module obtained at 75 GeV muon beam. (left) Peaks are pedestals. (right) Peaks correspond to muon energy deposition of about 5 MeV in each section.

The total energy deposition of pions over all 9 modules for different beam energies is shown in Fig. 46 together with the simulation results. The experimental data (blue histograms) and the simulated spectra (red histograms) are in rather good agreement for all measured energies.

The linearity of the calorimeter response to the hadrons with different energies is shown in Fig. 47 (right). Plotted is the mean value of the deposited energies (see Fig. 46) as function of beam energy. Fig. 47 (left) presents the energy resolution as function of beam energy. From the fit to 5 points one can extract the stochastic term of about 55%, and the constant term of 3.6%. This constant term is due to the lateral shower leakage and only partially fulfilled compensation condition. For a fully compensated calorimeter the constant term must be zero.

The first section of the module has a material budget corresponding to about 17 radiation lengths. Therefore, practically the full electromagnetic shower from positrons, which are a contamination of the 30 GeV pion beam, is deposited in this section as shown in Fig. 48(left). The energy depositions in the full module from hadrons and positrons are compared in the right panel of Fig. 48. The measured energy deposition is about 15-20% higher for positrons than for hadrons.

Both observations (non-zero constant term in energy resolution and higher energy deposition for positrons) indicate that the condition of full compensation in the prototype calorimeter is not fulfilled. The ratio lead-scintillator = 4/1 might not be the fully compensating condition, and should be changed for the full-size calorimeter. A detailed study of compensation for lead-scintillator calorimeters in [14] indicates that full compensation may be achieved at the ratio lead-scintillator = 4.55/1. For 16 mm thick lead tiles this would correspond to 3.5 mm thick scintillator tiles.

On the other hand, the calorimeter prototype with $30 \times 30 \text{ cm}^2$ front size is relatively small, and might not contain the entire hadron shower, resulting in a non-negligible lateral shower leakage. The comparison

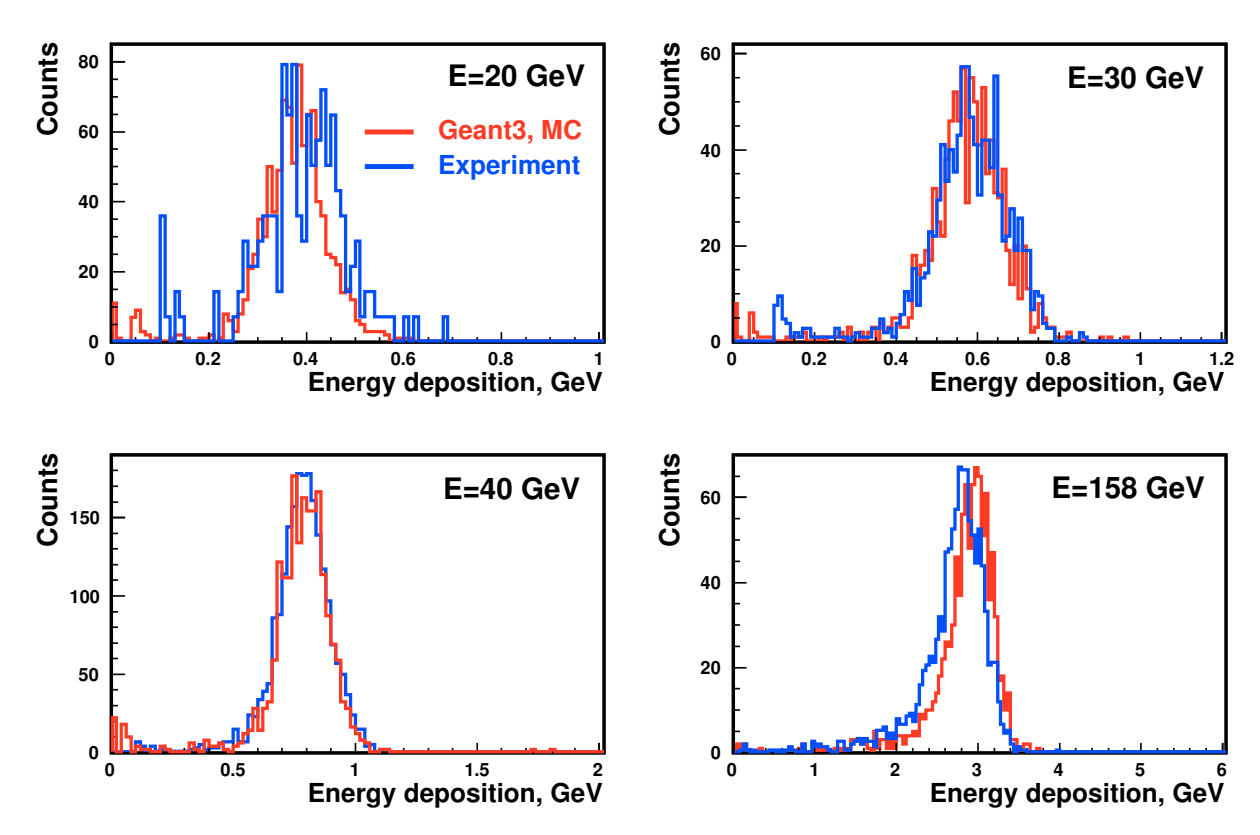


Fig. 46: Energy deposition of pions with different beam energies summed up over all 9 modules of the calorimeter. Blue lines are experimental data; red lines are distributions from GEANT3 MC simulations.

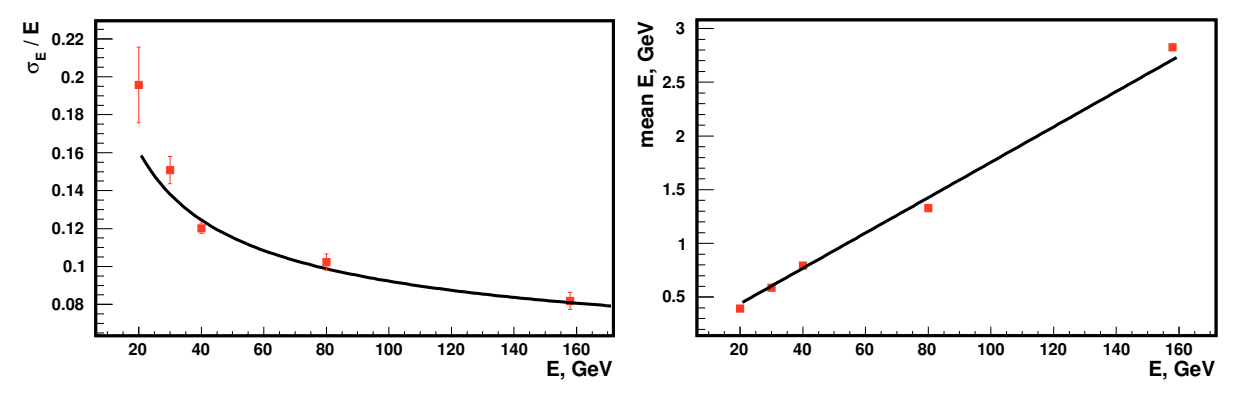


Fig. 47: (left) PSD energy resolution as function of beam energy. (right) Mean energy deposition in the calorimeter as function of beam energy.

of MC simulations for energy deposition in a 3×3 array to the full PSD configuration confirms that about 16% of the hadron shower escapes from the PSD supermodule. This number is rather consistent with the observed discrepancy in e/h energy depositions. The influence of the shower leakage on the energy resolution was investigated in [49,50], where the third term (together with stochastic and constant ones) in the parameterization of resolution was added:

$$\frac{\sigma_E}{E} = \sqrt{\frac{a^2}{E} + \frac{c^2}{\sqrt{E}}} + b \tag{10}$$

Here a, b, and c are stochastic, constant, and leakage terms, respectively. A fit of this formula to the experimental points as shown in Fig. 49 results in a stochastic term of 53.5%, and in a constant term of

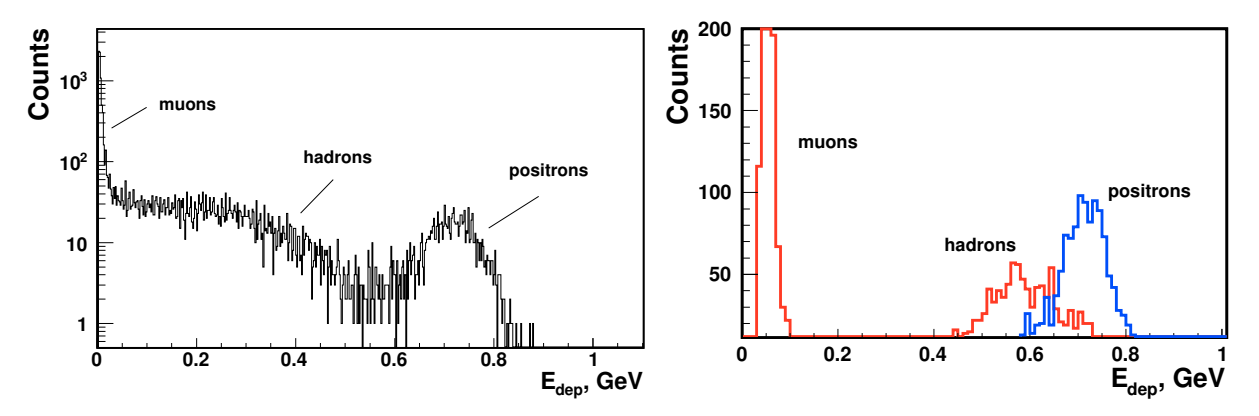


Fig. 48: (left) The energy spectrum in the first section of the central module for a beam energy of 30 GeV. A significant contamination of positrons in the hadron beam is observed. (right) Eenergy deposition for hadrons and positrons at 30 GeV.

1.9% at a fixed leakage term of 16%. A calorimeter with a constant term less than 2% might be regarded as "almost" compensating. It is worthwhile to mention that the constant term only affects the detection of single particles with high energy.

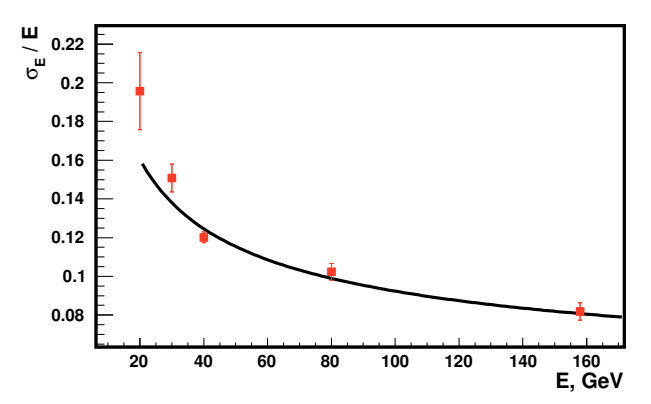


Fig. 49: Parameterization of the measured energy resolution with three terms: stochastic, constant and shower leakage. For shower leakage term of 16%, the constant term is equal 1.9%.

The purpose of the PSD is the measurement of a group of particles (projectiles) with similar energies. In this case the final energy resolution for *N* particles will be defined as the energy resolution of a single particle divided by the square root of the number of particles:

$$\frac{\sigma_E}{E}\Big|_{Nparticles} = \frac{1}{\sqrt{N}} \frac{\sigma_E}{E}\Big|_{1particles}$$
(11)

Obviously, the influence of the constant term is negligible in case of detection of a few particles. Note, that the existence of constant term in the energy resolution is a general problem for most of the calorimeters. The best lead-scintillator prototype calorimeter developed for the JLC project has a constant term of 1% [16]. The lead-scintillator calorimeter has a constant term of 2.5% and of 1% before and after light attenuation correction, respectively [41]. A similar calorimeter developed by the RD1 collaboration has a constant term of 1.8%.

In Fig. 50 the linearity and the energy resolution are plotted for the central single module of the PSD. In this case we consider one PSD module as an independent small-size calorimeter. A resolution of about 95% (stochastic term) is obtained. Note, that the MC simulation predicts a resolution of less than 80%.

The discrepancy is obviously explained by the definite size of the beam spot and its position at the front of the central module. One can conclude that a single module can be considered also as a calorimeter with moderate resolution. Such consideration might be helpful in some applications, for example for the determination of the reaction plane.

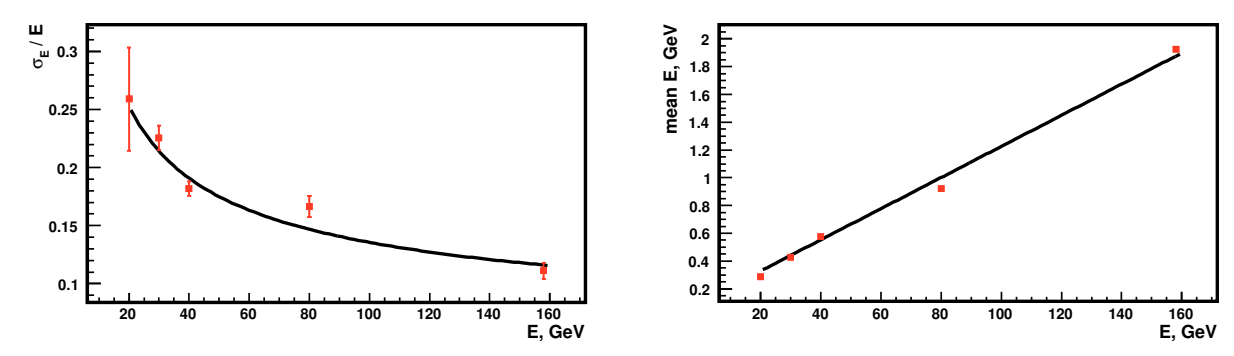


Fig. 50: Energy resolution (left) and mean energy deposition (right) of the central module as a function of the beam energy.

7.1.3 Supermodule response to low energy pions

To check the performance of the PSD supermodule for low pion energies a beam test has been performed at the T10 PS beam line at CERN in 2010. The energy resolution was determined for a few pion energies: 2 GeV, 4 GeV, 5 GeV and 6 GeV. The distributions obtained for the energy deposition are shown in Fig. 51, and are compared to results of MC simulations. The experimental and simulated data agree well, except for the lowest energy of 2 GeV where the experimental spectrum is narrower comparing to the simulated one. The reason for this effect might be a contamination of muons in the pion beam at this low energy.

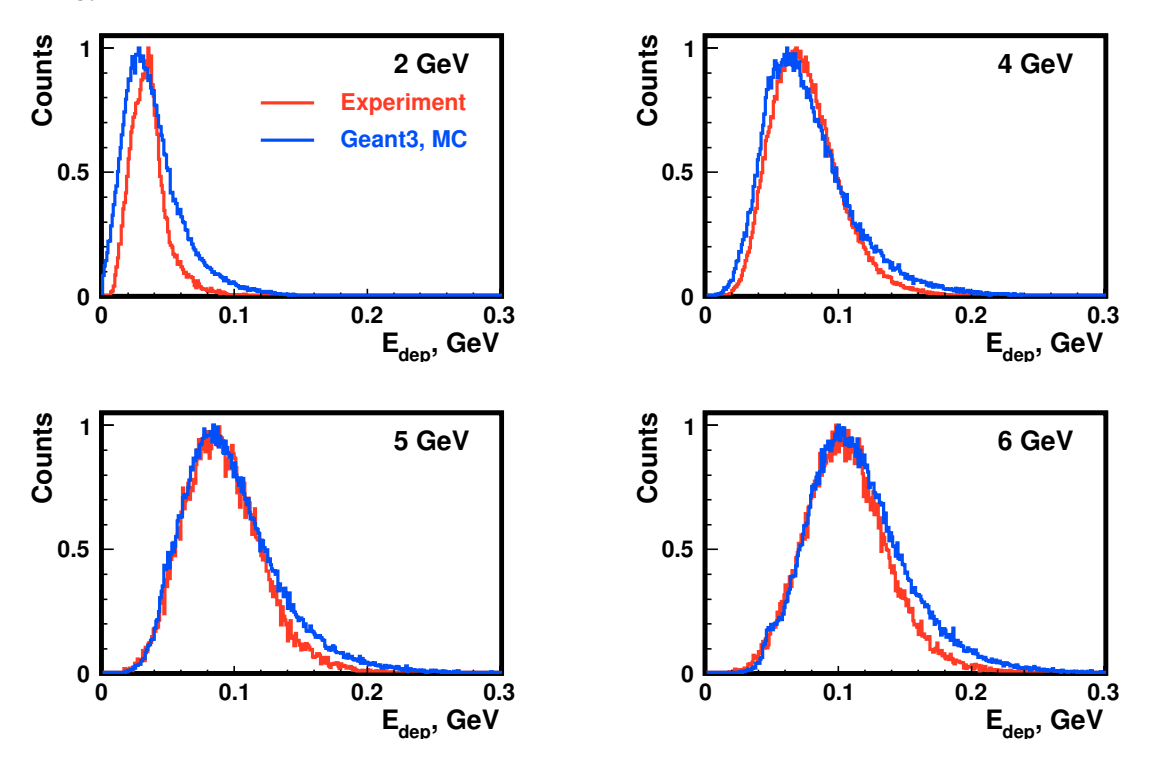


Fig. 51: Energy deposition for pions for different beam energies summed up over all 9 modules of the calorimeter. Red lines are experimental data; blue lines are distributions from GEANT4 MC simulations.

The experimental data obtained at low energies were combined with the previous results obtained at higher energies to get the performance of the PSD over the full pion energy range from 2-158 GeV. The experimental resolutions at different beam energies are plotted in Fig. 52. These experimental points were fitted again by the three term curve with stochastic, constant and shower leakage components. The fit gives the following results: the shower leakage term contributes by 16%, the constant term by 2.0% and the stochastic term by 55%. These numbers are in very good agreement with the previous data obtained at high energies only.

7.1.4 Large module response to low energy protons

The use of the CBM PSD at SIS100 energies requires an additional study of the calorimeter response for hadron energies below 10 GeV. In this region the response of the calorimeter should be different for pions and protons due to the limited hadron shower development for the proton energies below 5 GeV. This feature requires an additional experimental study at low proton energies. For this purpose, the large prototype PSD module with transverse size of $20\times20~\text{cm}^2$ has been tested at the T10 PS beam line at CERN in 2012. This beam line provides hadrons with momenta from 2-6 GeV/c. The setup is shown in Fig. 53.

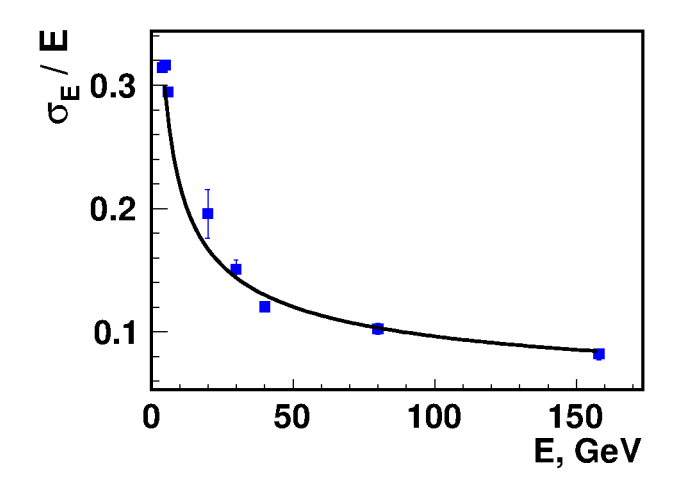


Fig. 52: The PSD energy resolution as function of the pion beam energy. The curve with a stochastic, a constant and a shower leakage term is fitted to the experimental points. The constant term is 2.0%, the stochastic term is 55% for a fixed shower leakage term equal to 16%.

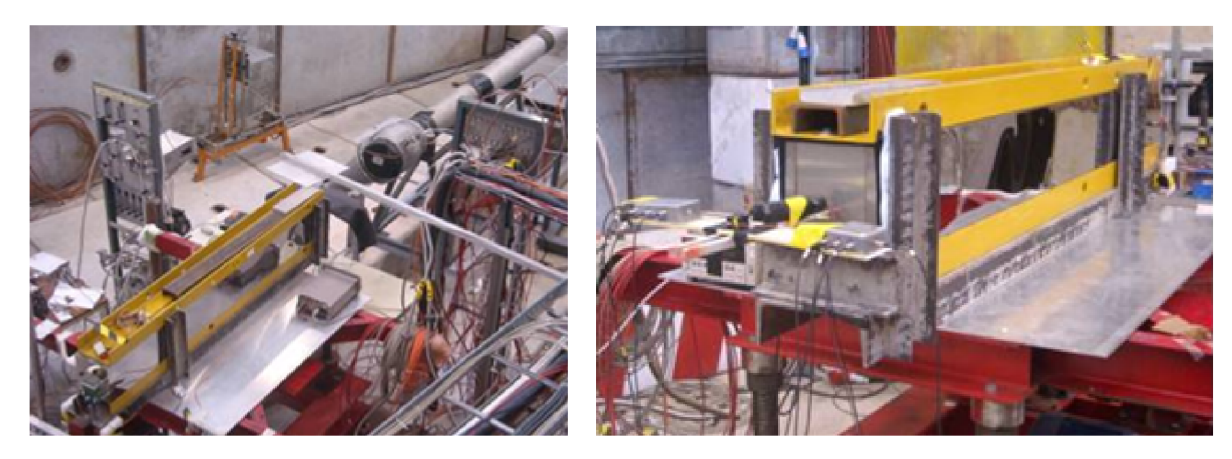


Fig. 53: Test setup with a large PSD module at the CERN T10 PS beam line.

The time of flight (TOF) method was used to separate the protons from pions in the secondary beam. Two scintillator detectors of size $20 \times 20 \text{ mm}^2$ measured the TOF of beam particles. One of these detectors was installed at the center of the front surface of the large module (Fig. 53, right), and another one was placed at a distance of about 15 meters upstream.

The two-dimensional energy versus TOF spectra for two incident particle momenta of 2 and 6 GeV/c are shown in Fig. 54. The time resolution of the scintillator detector was about 50 psec. Pions and protons could be well identified over the full momentum range from 2-6 GeV/c.

The muons in the T10 beam line have been used for the calibration of the calorimeter module. The distribution of energy deposited by muons for each of the 10 sections is shown in Fig. 55. A good separation of muon peaks from the pedestals was observed. A light yield of about 2 photoelectrons/MeV is estimated from the muon energy depositions.

A clear difference in the shower profile is observed for pions and protons at energies below 6 GeV. The sum of the energy depositions for protons and pions with an energy of about 2 GeV are shown in Fig. 56. Here the deposited energy distributions from protons are shown for ten cases: energy deposition in the first section, the sum of energy depositions in two first sections etc. up to the sum of energy depositions in all 10 sections. Two components in the energy deposition are clearly seen: the component from ionization

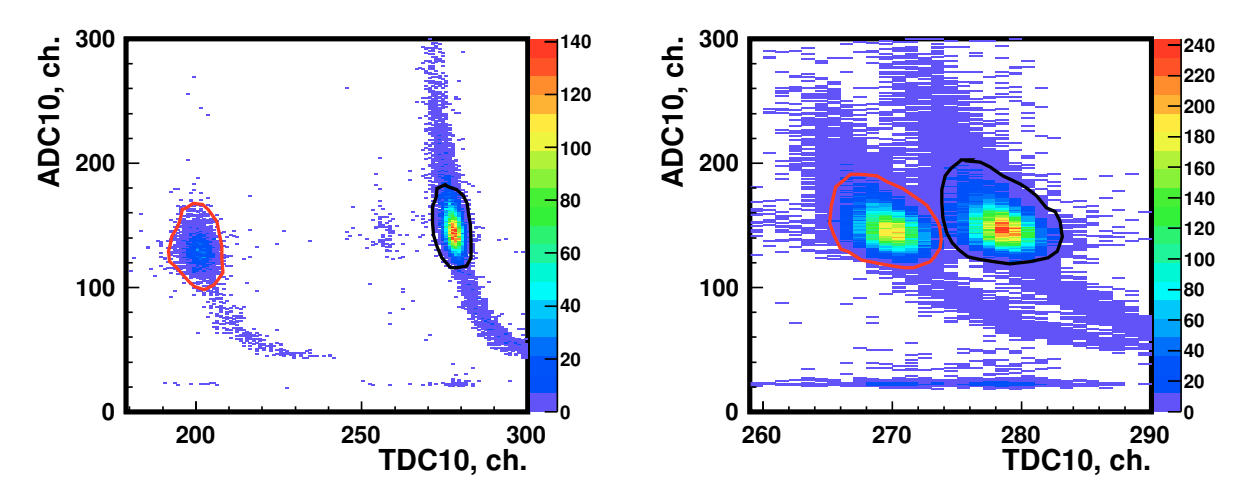


Fig. 54: Two dimensional plots dE-TOF for beam particles of 2 GeV/c (left) and 6 GeV/c (right).

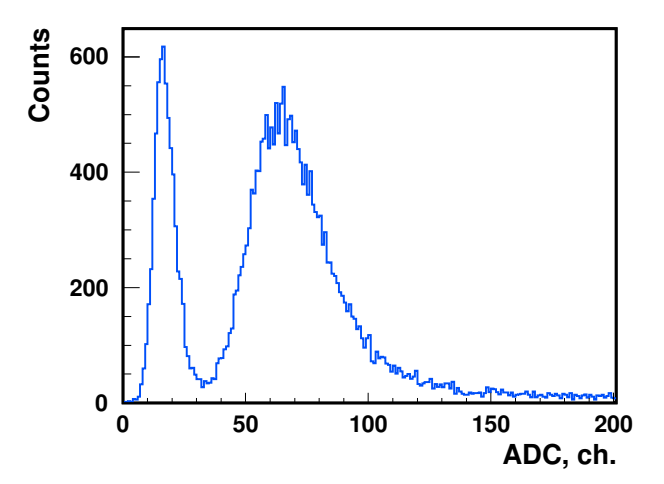


Fig. 55: Muon energy deposition in one of the module sections.

losses of primary hadrons, and that from the hadronic shower. According to the measurements, the first mechanism prevails for 2 GeV/c protons. Starting from 3 GeV/c clear contributions from the hadronic shower is visible also. At higher energies of protons and pions, the contribution from the hadron shower increases, and, moreover, it is larger for pions than for protons.

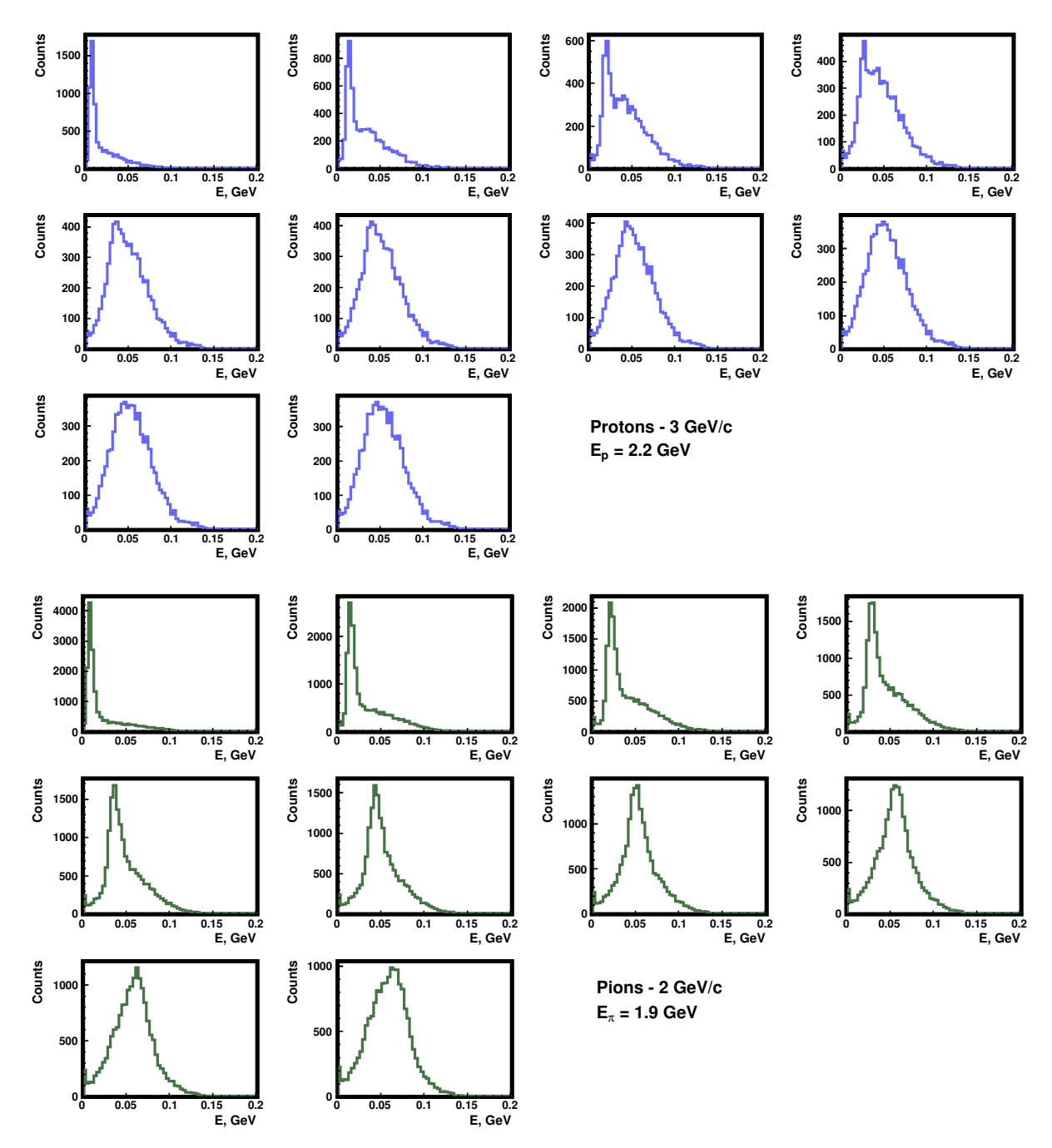


Fig. 56: Sum of energy depositions in module sections for protons and pions at an energy of about 2 GeV.

The energy resolution and the linearity of the large module for protons with momenta from 3-6 GeV/c are shown in Fig. 57. These parameters are in good agreement with the previous measurements with the PSD supermodule at higher energies.

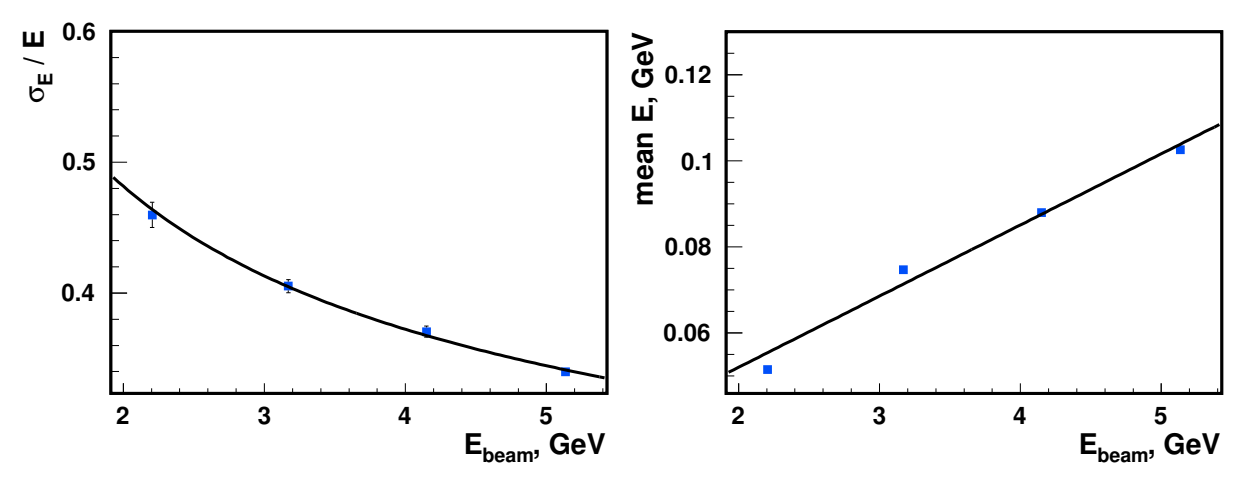


Fig. 57: Energy resolution (left) and linearity response (right) for large module measured for proton momenta from 3-6 GeV/c.

The R&D studies of the prototypes described above demonstrated the reliability of the proposed concept and the technical design of the lead-scintillator sandwich calorimeter for CBM. These tests confirm that the proposed design of the modules and the selected scheme of light readout provides an energy resolution of $\sigma_E/E < 60\%/\sqrt{E(\text{GeV})}$ as well as a good linearity of the PSD response.

7.2 Performance of the NA61 calorimeter

Recently, a hadron calorimeter similar to the PSD consisting of small and large individual modules has been constructed for the NA61 experiment at CERN. The response of the calorimeter was intensively studied with proton and muon beams. Moreover, in the end of 2011 a large part of this calorimeter was used in the first Be-Be physics run at Be beam energies of 40, 75 and 150 AGeV. In the end of 2012 and beginning 2013 the full calorimeter has been used for the second part of Be-Be run at Be beam energies of 13, 20 and 30 AGeV. In the following the main characteristics of the NA61 calorimeter and the difference with respect to the CBM PSD are shortly described.

A schematic view of the NA61 calorimeter is shown in Fig. 58 (left). It consists of 16 small modules

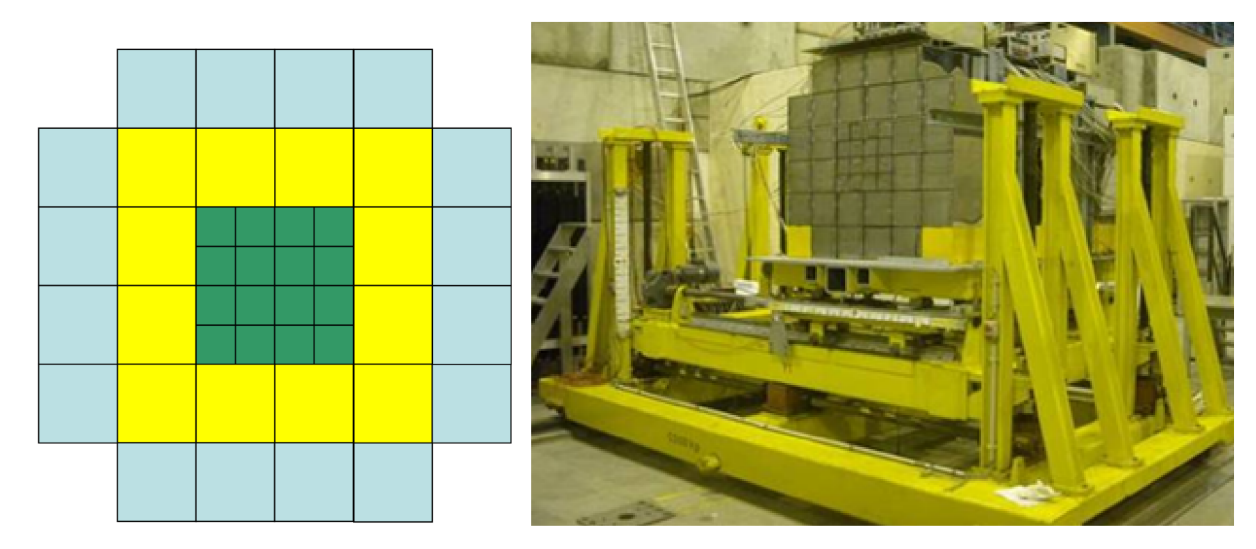


Fig. 58: Schematic view (left) and fully assembled calorimeter (right) at the NA61 experiment at CERN.

with transverse size of $10 \times 10 \text{ cm}^2$ and 28 large modules with transverse size of $20 \times 20 \text{ cm}^2$. The design of the modules is identical to the ones proposed for the CBM. The NA61 calorimeter has no beam hole in the center (in contrary to the CBM PSD) since the beam intensity at NA61 does not exceed 2×10^5 ions/sec. Due to the absence of the beam hole, the precision in the determination of number of projectile spectators will be higher than for CBM because there the heavy fragments pass through the beam hole and can't be measured. MAPD-3A photodiodes are used as photodetectors in NA61. A photo of the NA61 calorimeter is shown in Fig. 58 (right). The NA61 calorimeter is installed at a movable platform which is able vary the position of the 17 tons calorimeter with respect to the target depending on the ion beam energy. The platform also provides a transverse displacement of the detector which is needed for the calibration of individual modules with a muon beam.

The calibration of the modules was performed by 100 GeV muons. After that scanning of the calorimeter modules with a proton beam with momentum 158 GeV/c was performed. Blue and red curves in 59 correspond to different methods of reconstruction of proton energy. The blue line corresponds to the energy sum in all modules, while the red one is for the corresponding clusters of the modules. In the last case only the module irradiated by the proton beam (center of cluster) and the surrounding modules were used in the energy reconstruction. The mean values of the reconstructed energies are very close to the real beam energy in both cases.

The energy resolution of the modules after scanning with 158 GeV/c protons is presented in Fig. 60. The small variations in the energy resolution could be explained by the precision of the energy calibration. These results obtained with the NA61 calorimeter are in full agreement with the previous prototype tests and with the MC simulations for the PSD.

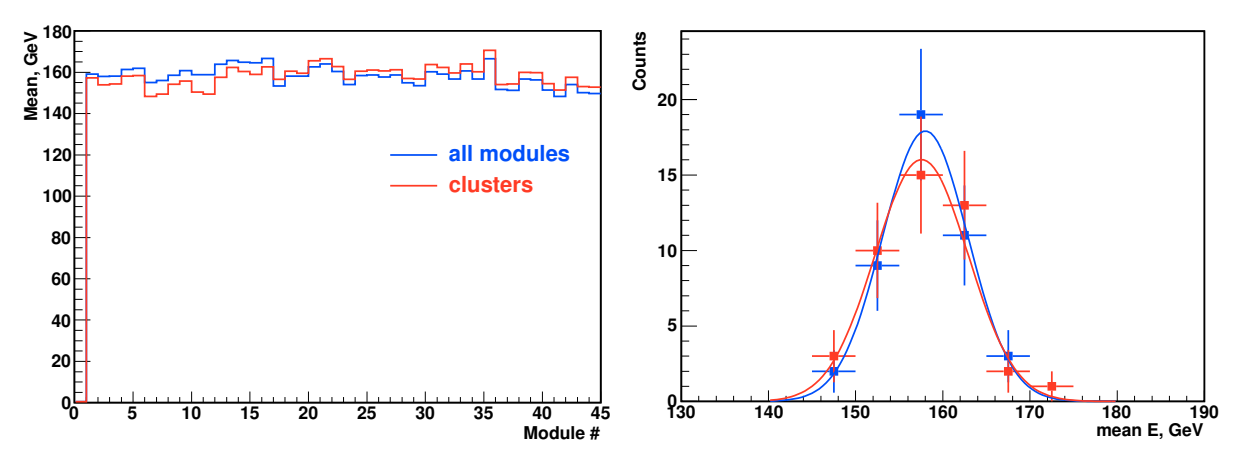


Fig. 59: Mean values of the reconstructed energy of 158 GeV/c protons in the PSD modules (left), and the distributions of mean values in modules (right).

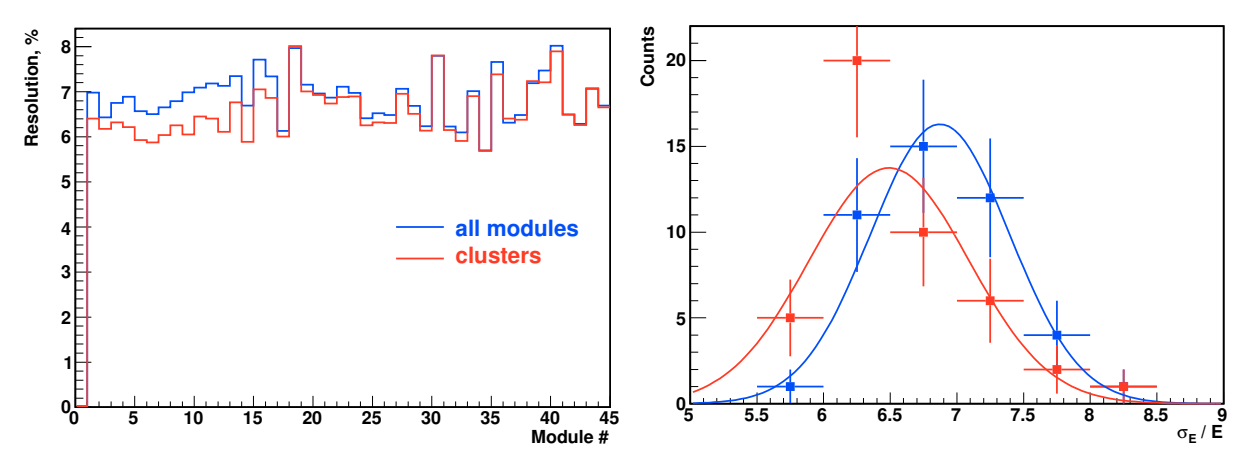


Fig. 60: Energy resolution for 158 GeV/c protons (left), and distributions of resolution for different modules (right).

The first NA61 physics run with Be-Be has been performed using Be⁷ incident ions with energies of 40, 75 and 150 AGeV selected from a fragmented ion beam. Beryllium beam ions were created by the fragmentation of an incident lead beam on Be target. Be⁷ ions from the fragmented beam have been selected by two beam detectors, Cherenkov (Z-detector) and TOF (A-detector), installed in H2 beam line [57]. Fig. 61(left) depicts a two dimensional plot of the energy loss in the scintillator detector (A-detector) installed at distance 140 m upstream the Be target versus the amplitude from the quartz Cherenkov detector (Z-detector) installed near the target. The Be⁷ ions with incident ion momentum of 75 AGeV/c are clearly identified. The amplitude spectra from the A-detector for a beam energy of 75 AGeV is shown at Fig. 61(right).

Fig. 62 depicts the correlation of the energy deposition of the fragmented beam in the calorimeter versus the amplitude of the Cherenkov detector (left), and the corresponding energy deposition in the PSD (right) for the beam energy 75 AGeV. The beam fragments are clearly identified in the calorimeter. The same distributions, but for a beam energy of 13 AGeV, are shown in Fig. 63.

The energy spectra measured by the calorimeter for $Be^7 + Be^9$ reaction at beam energies of 40A GeV, 75 AGeV and 150 AGeV are shown in Fig. 64. The spectra are shown for the beam trigger (blue) and the interaction trigger (red).

The experience in the operation of the NA61 hadron calorimeter during forthcoming beam runs will be

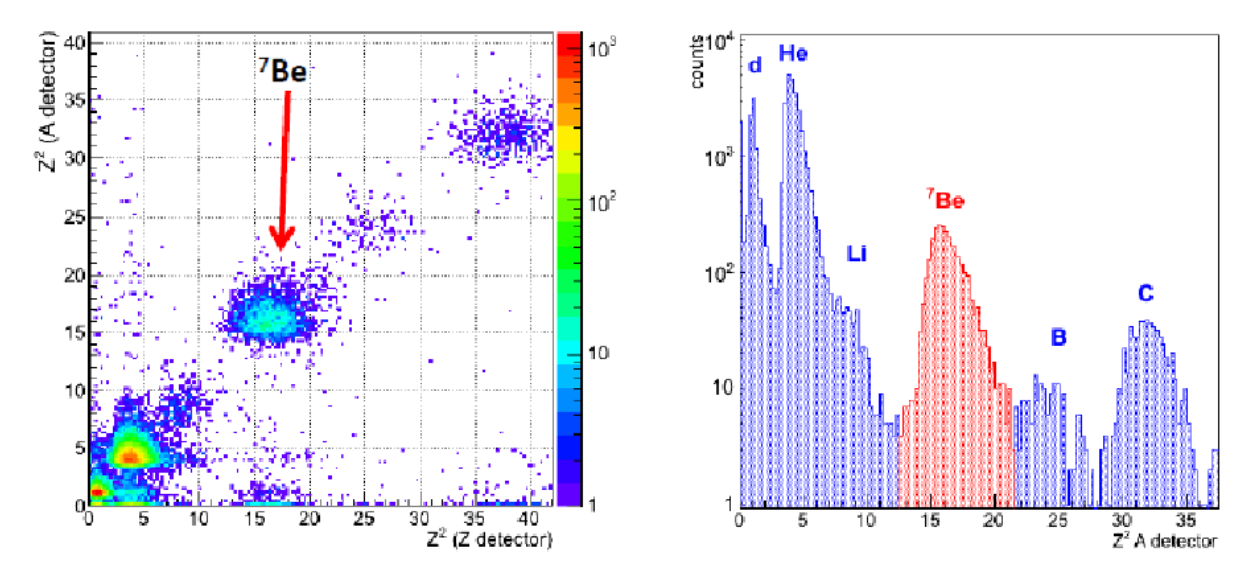


Fig. 61: Two-dimensional plot of Z^2 measured by the A-detector versus the amplitude of the Z-detector (left), and the amplitude spectra from the A-detector for a beam energy of 75 AGeV (right).

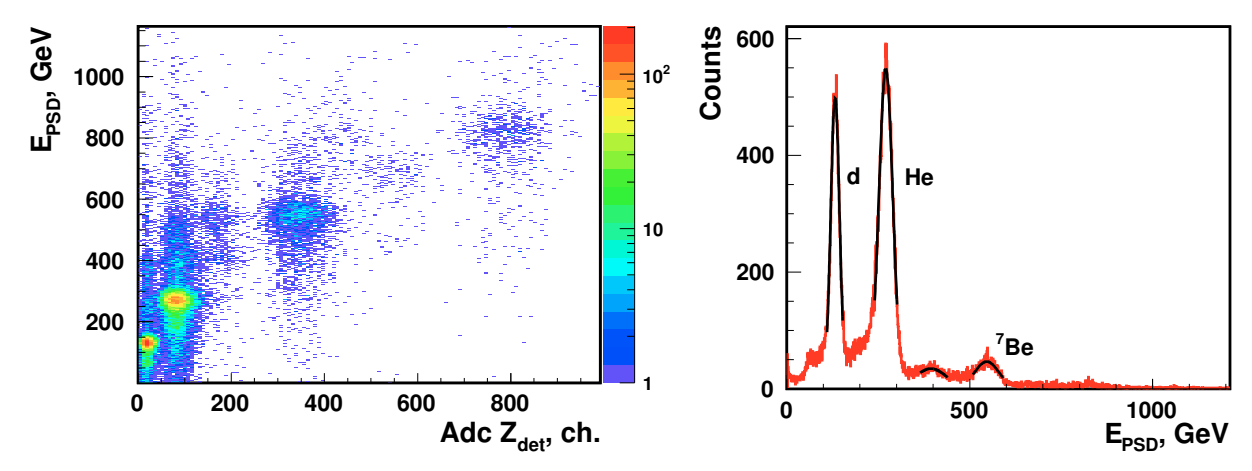


Fig. 62: Two-dimensional plot of energy deposition measured in the calorimeter versus amplitude of *Z*-detector (left), and the measured energy deposition in the calorimeter for the beam energy of 75 AGeV (right).

very useful for the construction of the CBM PSD.

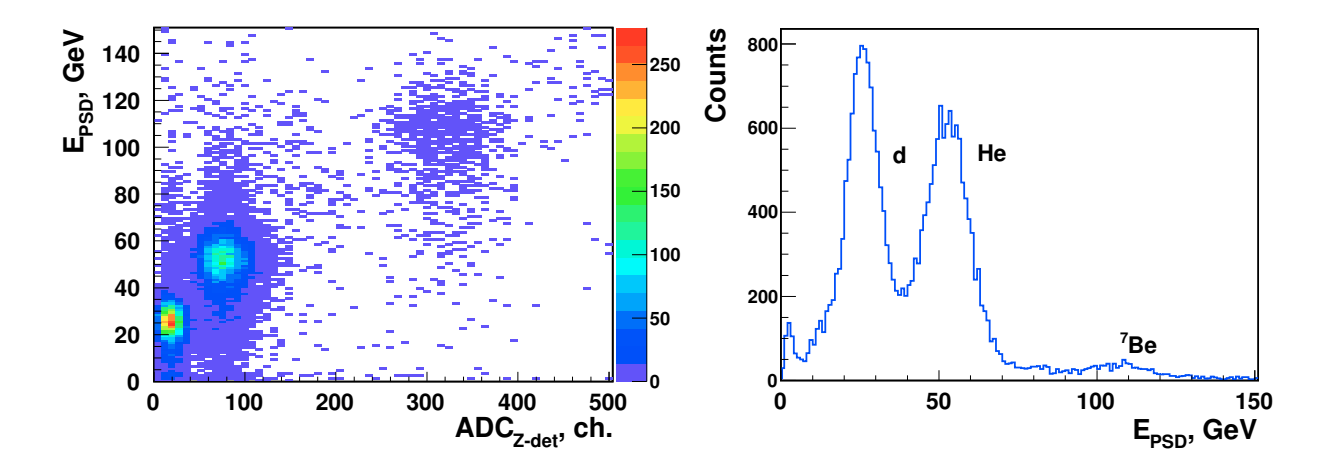


Fig. 63: Two-dimensional plot of the energy deposition measured in the calorimeter versus the amplitude of Z-detector (left), and the measured energy deposition in the calorimeter for the beam energy of 13 AGeV (right).

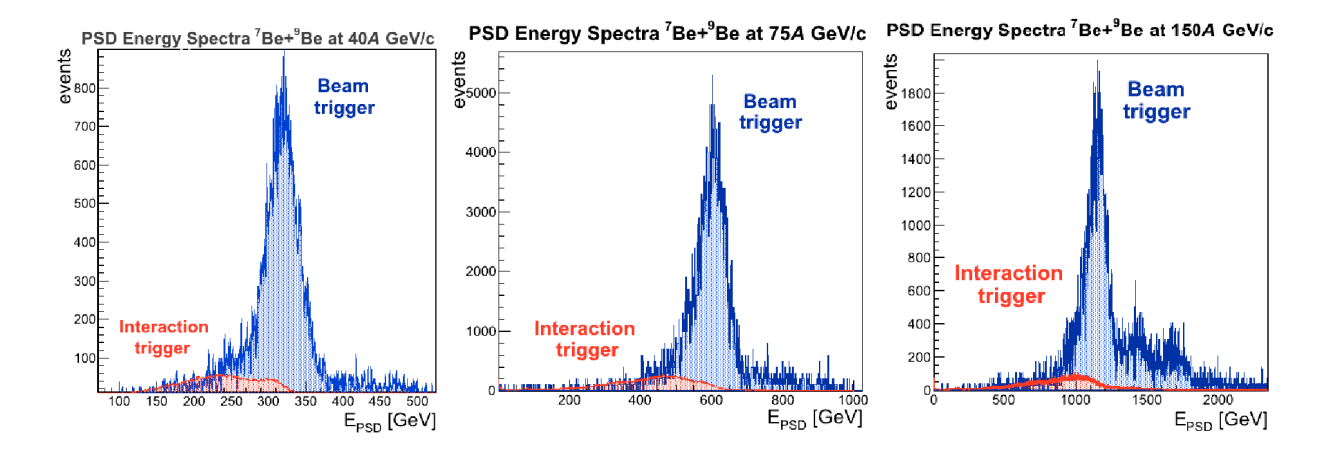


Fig. 64: PSD energy spectra for $Be^7 + Be^9$ reaction measured for beam momenta of 40A GeV/c, 75A GeV/c and 150 AGeV/c (from left to right). The spectra are shown as for the beam trigger (blue) and the interaction trigger (red).

7.3 Test of avalanche diodes

There are a few commercial types of G-APDs produced by several companies. A few types of G-APDs produced by a CPTA Co., Moscow and Zecotek Co. have been tested with a few scintillator tiles produced at INR (Moscow). The photo of one such tile together with three tested MAPDs is presented in Fig. 65.

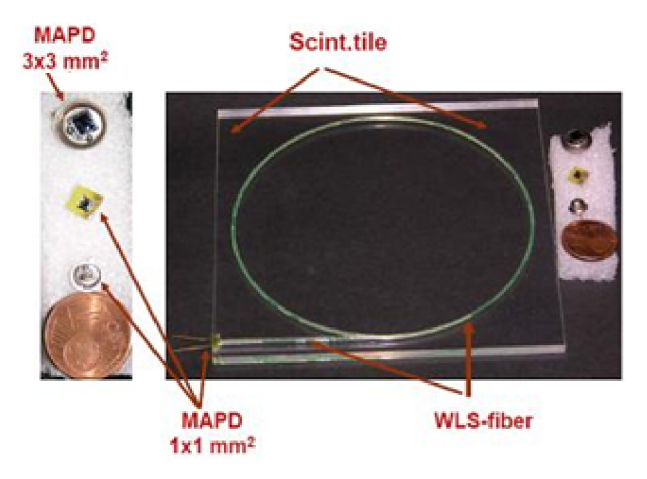


Fig. 65: The photo of one scintillator tile produced and tested at INR. A few samples of used MAPDs are shown.

The main task was to study the light yield produced by minimum ionizing particles (MIPs) and the uniformity of the light collection along the scintillator tile + WLS fiber + MAPD unit. G-APDs with individual surface resistors measure the light yield in absolute units (number of photoelectrons, p.e) due to its perfect single electron resolution that allows to calculate the absolute light yield as number of the peaks corresponding to 1 p.e., 2 p.e., 3 p.e., etc. signals. Such peaks (Fig. 66, left) are obtained by illuminating the G-APD with low intensity pulses from LED. Also, the ADC spectrum from MIPs which crossed the tile is shown (Fig. 66, right). The obtained light yield of about 15-20 photoelectrons/MeV is rather high. These results were obtained with a 576 pixel G-APD produced by CPTA Co. (Moscow).

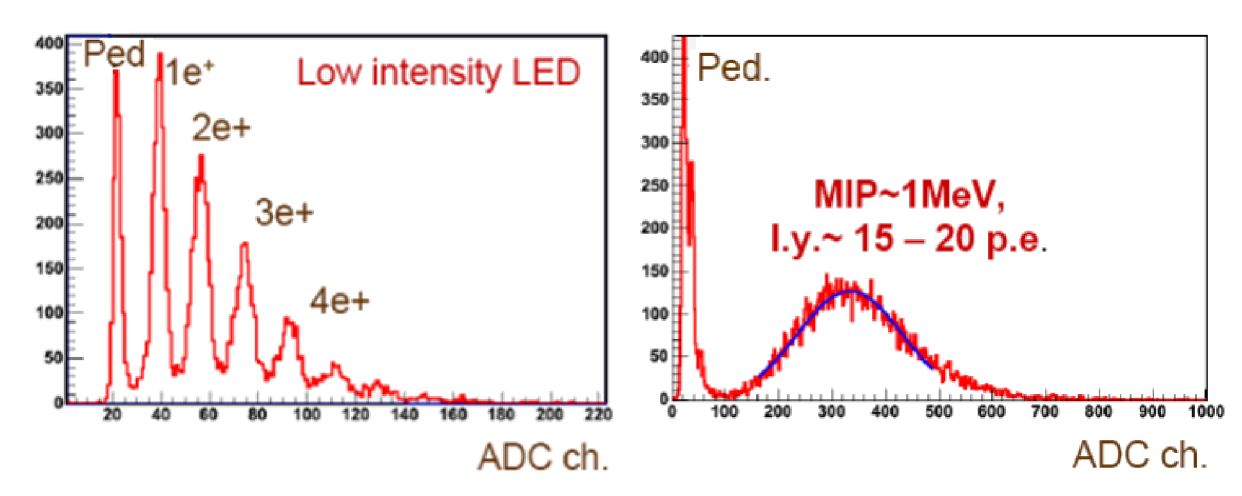


Fig. 66: (left) The single electron peaks obtained from low intensity LED illuminating the G-APD with 576 pixels from CPTA Co. (Moscow). (right) The ADC spectrum from minimum ionizing particles (cosmic rays) crossing the scintillator tile. A light yield of about 15-20 photoelectrons is achieved.

The results for the $1 \times 1 \text{ mm}^2$ and $3 \times 3 \text{ mm}^2$ MAPD samples produced by Zecotek Co. are slightly worse because of lower photon detection efficiency. A light yield of about 10 photoelectrons/MeV was obtained for the scintillator tiles with short WLS-fibers (Fig. 67).

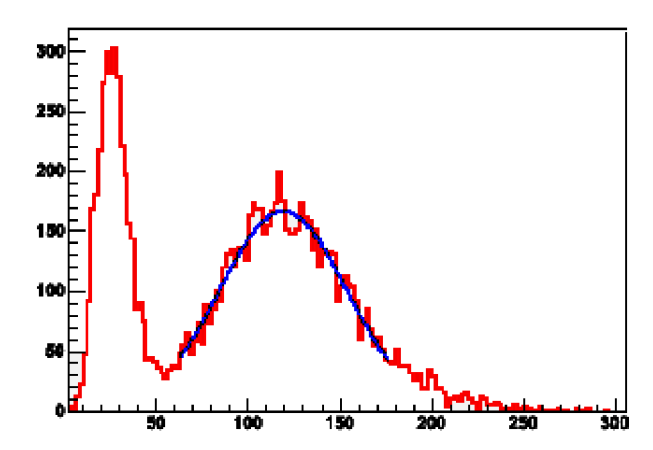


Fig. 67: ADC spectrum from minimum ionizing particles (cosmic rays) crossing the scintillator tile read out by a MAPD from Zecotec Co. Here a MAPD with 10⁴ pixels/mm² has been used.

For the PSD we will use MAPDs with an active area 3×3 mm² and a pixel density of about 10^4 /mm² produced by Zecotek as photon detectors. Their photon detection efficiency is about 15-20% at 500-550 nm (Fig. 68) which is well matched to the emission spectrum of WLS-fibers. The photon detection efficiency has three contributions: the quantum efficiency which is about 70-90% for normal APDs; a geometrical factor that reflects the fraction of the active area respective whole APD square, and the probability to initiate the Geiger discharge. The working voltage ranges from 60 V to 90 V depending on the type of MAPD. The gain of these MAPDs is about 5×10^4 , and an additional amplifier for the amplification of the signal by a factor of a few tens is requested.

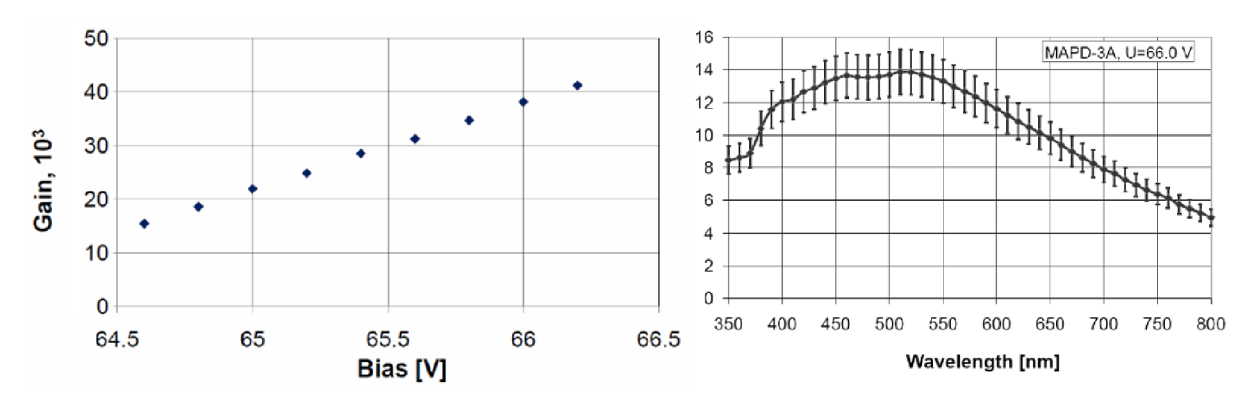


Fig. 68: The photon detection efficiency of MAPD (Zecotek) with pixel density $10^4/\text{mm}^2$ and active area 3×3 mm² as a function of bias voltage (left), and as a function of light wavelength (right) [58].

The MAPDs from Zecotek Co. have a micro-well structure and a large pixel density up to $40000/\text{mm}^2$. Such huge pixel density ensures the linearity of the response for the signals up to 15000 photoelectrons that is rather safe for CBM energies. The linearity was measured by illuminating the selected $3 \times 3 \text{ mm}^2$ MAPD by a light emitting diode with a variable light intensity. In case of a linear response the square of the signal width (square of sigma) must be equal to the signal amplitude, if both parameters are measured as a number of the photoelectrons. As seen in Fig. 69, the linearity is preserved up to 10^4 photons that it sufficient for the energy deposits in the PSD.

The rate capability of MAPDs is limited by the recovery time of a few microseconds of the individual pixels. The MAPD-3A which has a large dynamical range still works at counting rates of about 10⁵ Hz without significant amplitude reduction. This is illustrated in Fig. 70 for an average light signal of about 1500 photoelectrons. At a frequency of 10⁵ Hz the MAPD amplitude drops by about 5%.

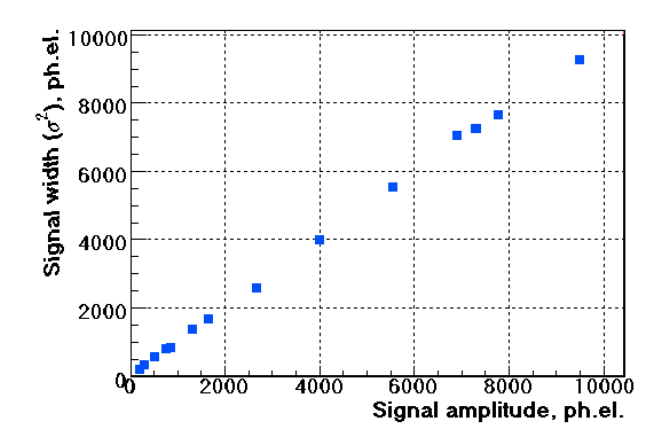


Fig. 69: The signal width for a 3×3 mm² MAPD irradiated by a LED as function of the signal amplitude. The Y-axis is the square of sigma of the signal distribution expressed in the number of the photoelectrons.

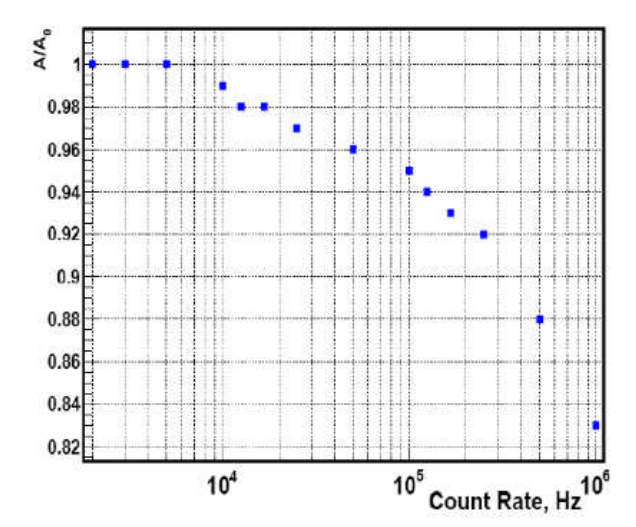


Fig. 70: The MAPD amplitude as function of frequency. The initial MAPD amplitude is about 1500 photoelectrons corresponding to about 750 MeV of deposited energy.

As will be shown in the next Chapter, in fully assembled PSD modules with MAPD-3A readout the light yield equals to 2 photoelectrons per 1 MeV of deposited visible energy. 1500 photoelectrons detected by a single photodiode correspond to 750 MeV deposited energy in one PSD module section. Thus the MAPD-3A performance fits the dynamical range at SIS100 energies. The extension to SIS300 energies requires a factor of 4 larger dynamical range for a few modules close to the beam hole. One solution is to reduce the bias voltages at the MAPD-3A photon detectors which would result in smaller light yields of the PSD modules.

The linearity of these photodiodes is preserved up to 15000 photoelectrons, and the limited dynamical range is caused only by the recovery time (up to a few microseconds) of the pixels. The long recovery time is also a problem for the CMS experiment at CERN which plans to use G-APDs for the upgrade of the hadron calorimeter. At present, several companies (Zecotek, Hamamatsu, KETEK, FBK at al.) concentrate on the development of new fast types of G-APDs for the calorimetrical application. Hamamatsu Co. already announced new types of multi-pixel G-APDs with recovery times of about 100 ns. Fast photodiodes with high pixel density will allow to extend the dynamical range by up to one order of magnitude without reduction of the light yield.

An important property of the MAPD-3A is its sensitivity to the temperature. The dependence of the gain of Zecotek MAPDs on temperature is about $4\%/C^{\circ}$. In order to ensure a constant MAPD gain the temperature has to be stabilized.

7.3.1 Radiation induced degradation of micropixel avalanche photodiodes

One of the most critical effects is the MAPD degradation caused by the neutron flux at the rear side of PSD calorimeter. Intensive radiation tests of MAPDs were performed by the CMS collaboration at CERN, where the same photodetectors are considered to be used in the future upgrade of the hadron calorimeter. The CMS collaboration has performed radiation tests of MAPDs with a γ -source up to a dose of 10 kGy without detectable degradation of their performance. The ionizing dose at the rear side of the PSD modules is much lower, and, therefore, no radiation damage of the MAPDs is expected.

According to FLUKA simulation maximum neutron flux at SIS 100 mm might achieve 3×10^{12} neutrons/cm² near the PSD beam hole with diameter 6 cm after 2 month of CBM run at 10 AGeV Au beam and beam intensity 10^8 ions/sec (see Fig. 74 in Sec. 7.4). At 35 AGeV the neutron flux near the beam axis is about 5×10^{12} . Neutron flux drops significantly with radius and is few times less for most of the calorimeter modules. The intensive studies of MAPD degradation under the neutron irradiation were performed by CMS collaboration up to the neutron flux 1×10^{13} neutrons/cm². A few parameters of MAPD-3A as gain, PDE, dark current were measured at different neutron doses. The dependence of MAPD-3A gain on the bias voltage is presented in Fig. 71(left). As seen, the gain drops for about 50% at the dose of 3×10^{12} n/cm². After that the gain degradation is very slow up to dose 10^{13} n/cm².

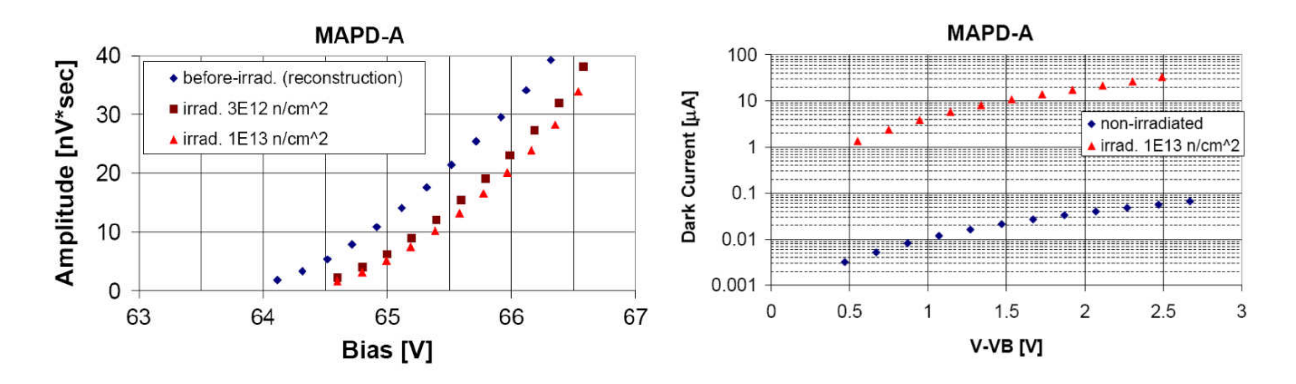


Fig. 71: (left) The gain of MAPD-3A as function of the bias voltage for different neutron fluxes [58]. (right) The MAPD-3A dark current as function of the difference between bias and break-through voltage before and after irradiation with a neutron flux of 10^{13} n/cm² [58].

The results of measurements of the dark current of MAPD-3A are shown in Fig. 71(right). The dark current increases up to a value of 30 μ A after a neutron dose of 10^{13} n/cm². However, even this value is not critical, but still enables a proper MAPD-3A performance. The drop of MAPDs gain can be taken into account by a careful control of MAPD amplitudes, and a permanent calibration of the PSD modules in case of a run at maximum intensity.

7.4 Detector radiation hardness

The high-intensity heavy-ion beams used in the CBM experiment pose a challenge on the radiation hardness of the hadron calorimeter. The possible degradation of the calorimeter performance after irradiation should be considered separately for PSD modules and photodetectors. The overall radiation dose deposited in the PSD and the neutron flux were simulated by FLUKA with the use of realistic CBM and the PSD geometry and material budget for SIS100 and SIS300 as shown in Fig. 72.

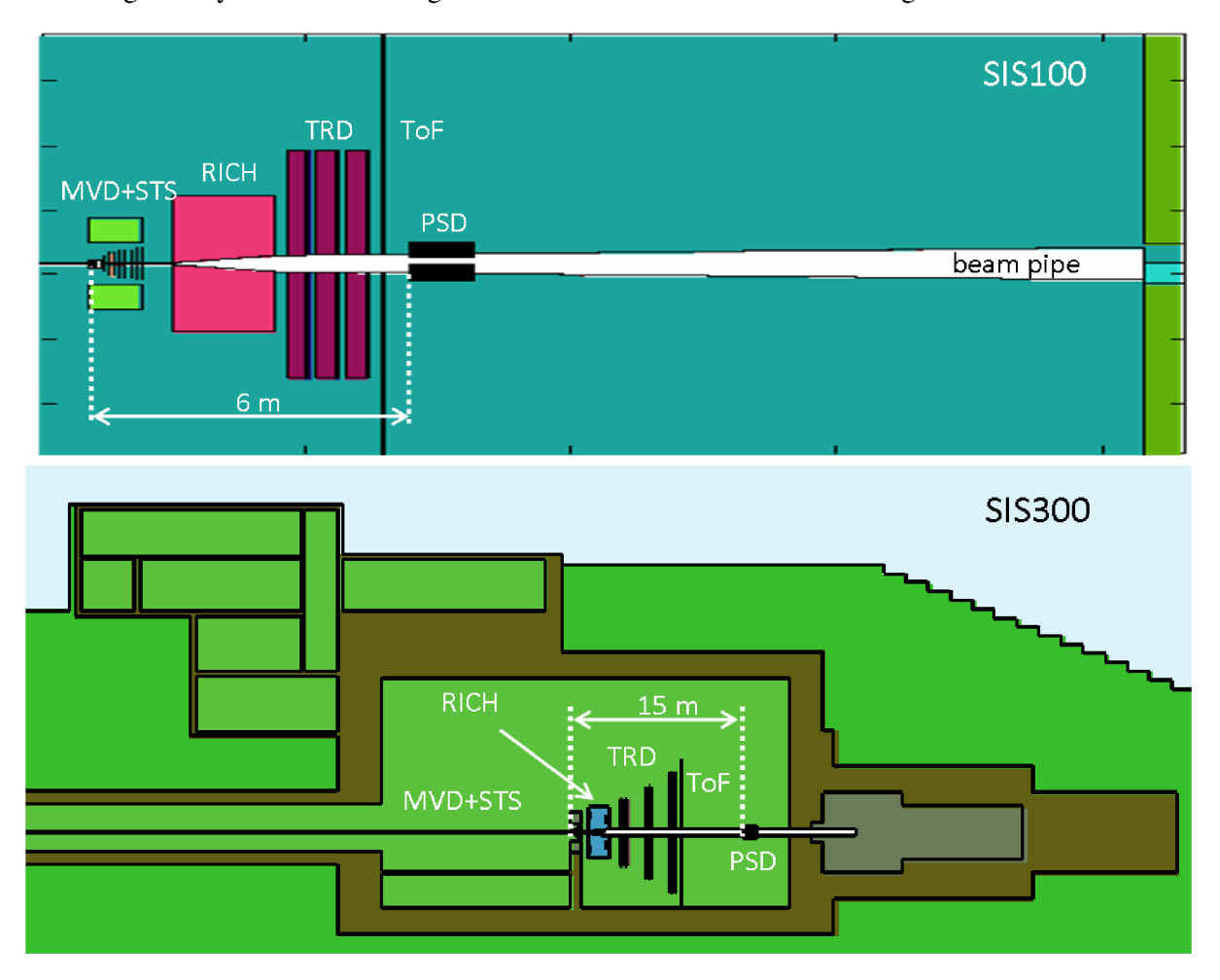


Fig. 72: The FLUKA geometry of the CBM experiment at SIS100 and SIS300.

Dose and neutron flux distributions were calculated for the PSD positioned at 8 m (SIS100) and 15 m (SIS300) from the target. The incident ion beam deflected by the CBM magnet passed through the hole with diameter 60 mm in the center module of the PSD. The dose and neutron flux have been calculated for the beam rate of 10⁸ ions per second (reaction rate of 10⁶ per second) for Au+Au reaction at 2, 10 AGeV and 35 AGeV. Calculations were done for 2 months of CBM beam run. The longitudinal dose distributions along the calorimeter modules at radius 10, 20 and 50 cm are shown in Fig. 73 for 2 AGeV (left), 10 AGeV (center) and 35 AGeV (right), respectively. As expected, dose distributions reflect the longitudinal profile of the hadronic shower in the calorimeter. As seen, the maximum radiation dose is about 700 Gy at 35 AGeV close to the beam hole and is not critical for scintillators.

The most critical effect is the photodetectors degradation caused by the neutron flux through the rear side of PSD calorimeter. According to FLUKA simulation (Fig. 74) this flux near the beam hole might achieve about 5×10^{12} neutrons/cm² for beam energy 35 AGeV after 2 months of CBM run at the beam rate of 10^8 ions per second. At SIS100 beam energies the neutron flux at rear side of the PSD is few

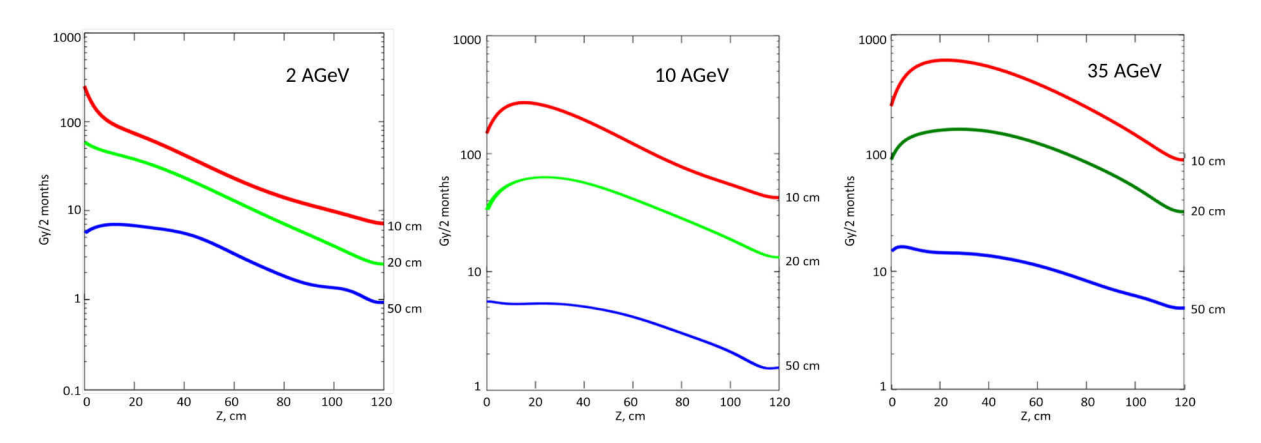


Fig. 73: The longitudinal distribution of the average dose along the PSD at 10,20 and 30 cm radius from beam axis for 2 and 10 AGeV beam energy and PSD at 8 m, (left and center plots, respectively) and for 35 AGeV beam, PSD at 15 m, (right plot) after 2 months of CBM run at the beam rate of 10^8 ions per second.

times less.

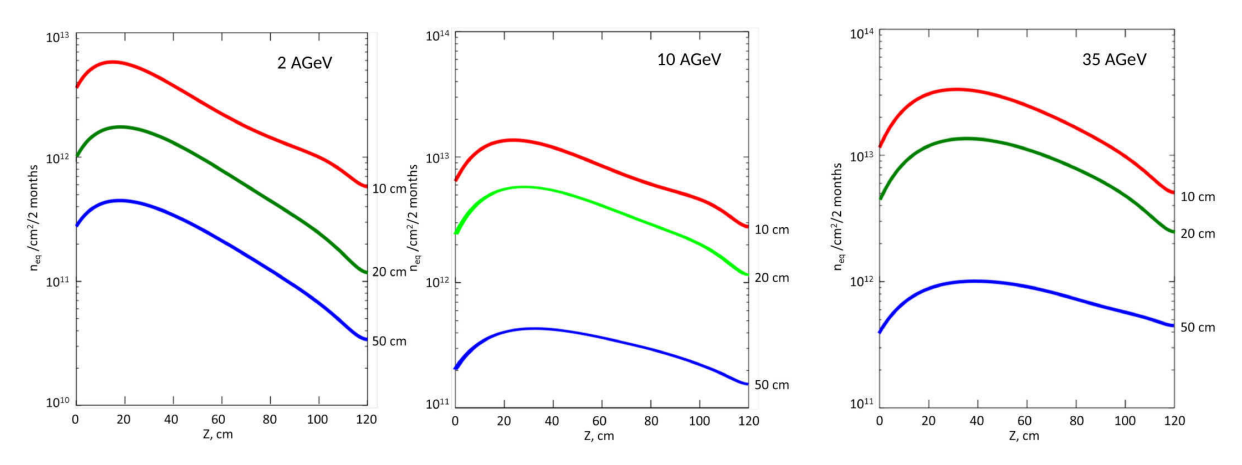


Fig. 74: Distributions of the neutron flux (cm²/s) through the PSD calorimeter at 2 AGeV (left), 10 AGeV (center) and 35 AGeV (right) Au beam energies after 2 months of CBM run at the beam rate of 10⁸ ions per second.

The corresponding reduction of the scintillator light yield and the MAPD degradation are not significant as discussed in Sec. 6.1.2 and Sec. 7.3.1.

8 Participating institutes

The institutes participating in the PSD project are located in Germany, Russia and Czech Republic. The coordination of the project is led by the INR, Moscow. The participating institutes and their responsibilities are shown in Table 2.

Institute	Responsibility
Institute for Nuclear Research of Russian	PSD simulation; development and construction of mod-
Academy of Science (INR), Moscow, Rus-	ules; module assembling and tests, development of ana-
sia	log FEE
Nuclear Physics Institute, Academy of	Development of the calibration system for the PSD,
Sciences of the Czech Republic, Řež,	module tests, simulation of the PSD performance with
Czech Republic	respect to flow determination. Construction of the PSD
	support structure and cooling system
Czech Technical University (CTU),	Development and tests of the light readout system for
Prague, Czech Republic	the PSD, module tests
Institut für Kernphysik, Technische Uni-	Development, construction and tests of digital electron-
versität Darmstadt, Darmstadt, Germany	ics for the PSD
GSI Helmholtz Center for Heavy Ion Re-	PSD integration into the CBM experiment
search GmbH, Darmstadt, Germany	

Table 2: Institutions participating in the construction of the PSD and their responsibilities.

References

[1] K. Fukushima and T. Hatsuda, *The phase diagram of dense QCD*, Rept.Prog.Phys. **74**, 014001 (2011), arXiv:1005.4814, doi:10.1088/0034-4885/74/1/014001.

- [2] W. Ehehalt and W. Cassing, *Relativistic transport approach for nucleus nucleus collisions from SIS to SPS energies*, Nucl.Phys. **A602**, 449 (1996), doi:10.1016/0375-9474(96)00097-8.
- [3] STAR Collaboration, A. Schmah, *Highlights of the Beam Energy Scan from STAR*, Central Eur.J.Phys. **10**, 1238 (2012), arXiv:1202.2389, doi:10.2478/s11534-012-0149-1.
- [4] NA61 Collaboration, A. Aduszkiewicz, NA61/SHINE at the CERN SPS: Plans, status and first results, Acta Phys.Polon. **B43**, 635 (2012), arXiv:1201.5879, doi:10.5506/APhysPolB.43.635.
- [5] FAIR, FAIR Baseline Technical Report 2006, www.fair-center.eu/fileadmin/fair/publications_FAIR/FAIR_BTR_6.pdf (2006).
- [6] B. Friman et al., The CBM physics book: Compressed baryonic matter in laboratory experiments, Lect.Notes Phys. 814, 1 (2011), doi:10.1007/978-3-642-13293-3.
- [7] CBM Collaboration, P. Senger and V. F. (Eds.), CBM Report 2013, http://www-alt.gsi.de/documents/DOC-2014-Mar-16-1.pdf (2012).
- [8] N. Herrmann, J. Wessels and T. Wienold, *Collective flow in heavy ion collisions*, Ann.Rev.Nucl.Part.Sci. **49**, 581 (1999), doi:10.1146/annurev.nucl.49.1.581.
- [9] R. Stock, Relativistic Heavy Ion Physics, (2010), doi:10.1007/978-3-642-01539-7.
- [10] J. M. Lattimer and M. Prakash, *Neutron Star Observations: Prognosis for Equation of State Constraints*, Phys.Rept. **442**, 109 (2007), arXiv:astro-ph/0612440, doi:10.1016/j.physrep. 2007.02.003.
- [11] R. Wigmans, On the Energy Resolution of Uranium and Other Hadron Calorimeters, Nucl.Instrum.Meth. A259, 389 (1987), doi:10.1016/0168-9002(87)90823-0.
- [12] S. Uozumi et al., Performance of a compensating lead / plastic-scintillator tile / fiber calorimeter, Nucl.Instrum.Meth. A487, 291 (2002), doi:10.1016/S0168-9002(01)00891-9.
- [13] G. A. Alekseev *et al.*, Study of the compensated lead hadron calorimeter on hadron, electron and lead-ion beams, Nucl.Instrum.Meth. **A461**, 381 (2001), doi:10.1016/S0168-9002(00) 01250-X.
- [14] JLC Calorimeter Group, Y. Fujii, *Performance of compensated tile-fiber hadron calorimeter*, Nucl.Instrum.Meth. **A453**, 237 (2000), doi:10.1016/S0168-9002(00)00638-0.
- [15] M. Golubeva et al., Forward hadron calorimeter for measurements of projectile spectators in heavy-ion experiment, Phys.Atom.Nucl. 75, 673 (2012), doi:10.1134/S1063778812060142.
- [16] A. Ivashkin et al., Hadron calorimeter with MAPD readout in the NA61/SHINE experiment, 1205.4864, arXiv:1205.4864.
- [17] M. Golubeva et al., Use of micro-pixel avalanche photodiodes for the readout of a lead/scintillator hadron calorimeter, Nucl.Instrum.Meth. A610, 366 (2009), doi:10.1016/j.nima.2009.05. 121.
- [18] V. Toneev and K. Gudima, *Particle emission in light and heavy ion reactions.*, Nucl.Phys. **A400**, 173C (1983), doi:10.1016/0375-9474(83)90433-5.
- [19] V. Toneev, N. Amelin, K. Gudima and S. Y. Sivoklokov, *Dynamics of relativistic heavy ion collisions*, Nucl.Phys. **A519**, 463C (1990), doi:10.1016/0375-9474 (90) 90649-7.
- [20] N. Amelin *et al.*, Transverse flow and collectivity in ultrarelativistic heavy ion collisions, Phys.Rev.Lett. **67**, 1523 (1991), doi:10.1103/PhysRevLett.67.1523.
- [21] A. B. et al., *MSDM Multy Stage Dynamical Model*, International Codes and Model Intercomparison for Intermediate Energy Activation Yields **NSC/DOC(97)-1**, NEA/P&T No 14 (1997).

- [22] S. Mashnik, A. Sierk, K. Gudima and M. Baznat, CEM03 and LAQGSM03: New modeling tools for nuclear applications, J.Phys.Conf.Ser. 41, 340 (2006), arXiv:nucl-th/0510070, doi: 10.1088/1742-6596/41/1/037.
- [23] S. G. Mashnik, K. Gudima, N. V. Mokhov and R. Prael, *LAQGSM03.03 Upgrade and its Validation*, 0709.1736, arXiv:0709.1736.
- [24] S. Mashnik et al., CEM03.03 and LAQGSM03.03 Event Generators for the MCNP6, MCNPX, and MARS15 Transport Codes, 0805.0751, arXiv:0805.0751.
- [25] A. Botvina et al., Production of hypernuclei in peripheral collisions of relativistic ions, Nucl.Phys. **A881**, 228 (2012), doi:10.1016/j.nuclphysa.2012.01.015.
- [26] J. Steinheimer et al., Hypernuclei, dibaryon and antinuclei production in high energy heavy ion collisions: Thermal production versus Coalescence, Phys.Lett. **B714**, 85 (2012), arXiv:1203. 2547, doi:10.1016/j.physletb.2012.06.069.
- [27] A. Botvina, K. Gudima and J. Pochodzalla, *Production of hypernuclei in peripheral relativistic ion collisions*, Phys.Rev. C88, 054605 (2013), arXiv:1307.5553, doi:10.1103/PhysRevC.88.054605.
- [28] A. V. Dementyev and N. M. Sobolevsky, *SHIELD*, a Monte Carlo Hadron Transport Code, http://www.inr.troitsk.ru/shield/introd-eng.html.
- [29] S. Bass et al., Microscopic models for ultrarelativistic heavy ion collisions, Prog.Part.Nucl.Phys. 41, 255 (1998), arXiv:nucl-th/9803035, doi:10.1016/S0146-6410(98)00058-1.
- [30] M. Bleicher et al., Relativistic hadron hadron collisions in the ultrarelativistic quantum molecular dynamics model, J.Phys. G25, 1859 (1999), arXiv:hep-ph/9909407, doi:10.1088/0954-3899/25/9/308.
- [31] E895 Collaboration, H. Liu et al., Sideward flow in Au + Au collisions between 2-A-GeV and 8-A-GeV, Phys.Rev.Lett. 84, 5488 (2000), arXiv:nucl-ex/0005005, doi:10.1103/PhysRevLett. 84.5488.
- [32] STAR Collaboration, L. Adamczyk et al., Beam-Energy Dependence of Directed Flow of Protons, Antiprotons and Pions in Au+Au Collisions, Phys.Rev.Lett. 112, 162301 (2014), arXiv: 1401.3043, doi:10.1103/PhysRevLett.112.162301(2014), 10.1103/PhysRevLett.112.162301.
- [33] CERN, GEANT, Detector Description and Simulation Tool, http://wwwasd.web.cern.ch/wwwasd/geant.
- [34] CBM Collaboration, J. e. a. Heuser, *Technical Design Report for the CBM Silicon Tracking System* (STS), http://repository.gsi.de/record/54798 **GSI-2013-05499** (2013).
- [35] A. M. Poskanzer and S. Voloshin, *Methods for analyzing anisotropic flow in relativistic nuclear collisions*, Phys.Rev. C58, 1671 (1998), arXiv:nucl-ex/9805001, doi:10.1103/PhysRevC. 58.1671.
- [36] E877 Collaboration, J. Barrette *et al.*, Energy and charged particle flow in a 10.8-A/GeV/c Au + Au collisions, Phys.Rev. C55, 1420 (1997), arXiv:nucl-ex/9610006, doi:10.1103/PhysRevC. 55.1420,10.1103/PhysRevC.56.2336.
- [37] I. Kisel, I. Kulakov and M. Zyzak, *Standalone first level event selection package for the CBM experiment*, IEEE Transactions on Nuclear Science **60**, 3703 (2013).
- [38] CBM Collaboration, I. Vassiliev et al., CBM annual report 2014, http://repository.gsi.de/record/54798 GSI-2013-05499 (2013).
- [39] H. Abramowicz et al., The Response and Resolution of an Iron Scintillator Calorimeter for Hadronic and Electromagnetic Showers Between 10-GeV and 140-GeV, Nucl.Instrum.Meth. 180, 429 (1981), doi:10.1016/0029-554X(81)90083-5.
- [40] K. C. Ltd., Scintillator Fiber Products, (1994).

[41] LHCb Collaboration, J. Alves, A. Augusto et al., The LHCb Detector at the LHC, JINST 3, S08005 (2008), doi:10.1088/1748-0221/3/08/S08005.

- [42] LHCb Collaboration, Z.Sadygov et al., Nucl.Instrum.Meth. 567, 70 (2006).
- [43] D. Renker, Geiger-mode avalanche photodiodes, history, properties and problems, Nucl.Instrum.Meth. A567, 48 (2006), doi:10.1016/j.nima.2006.05.060.
- [44] A. Akindinov et al., Scintillation counter with MRS APD light readout, Nucl.Instrum.Meth. A539, 172 (2005), arXiv:physics/0603224, doi:10.1016/j.nima.2004.10.026.
- [45] V. Andreev et al., A high granularity scintillator hadronic-calorimeter with SiPM readout for a linear collider detector, Nucl.Instrum.Meth. A540, 368 (2005), doi:10.1016/j.nima.2004. 12.002.
- [46] A. Stoykov *et al.*, Nuclear Instruments and Methods in Physics Research Section A: Accelerators, Spectrometers, Detectors and Associated Equipment **567**, 246 (2007).
- [47] I. B. et.al., Development of scintillation detectors based on avalanche microchannel photodiodes, Nuclear Instruments and Methods in Physics Research Section A: Accelerators, Spectrometers, Detectors and Associated Equipment 571, 317 (2007), Proceedings of the 1st International Conference on Molecular Imaging Technology EuroMedIm 2006, doi:http://dx.doi.org/10.1016/j.nima.2006.10.091.
- [48] Zecotek Photonics Inc., www.zecotek.com.
- [49] J. B. et al., *Test results of an electromagnetic calorimeter with 5 mm scintillating fibres readout*, Nuclear Instruments and Methods in Physics Research Section A: Accelerators, Spectrometers, Detectors and Associated Equipment **337**, 314 (1994).
- [50] D. Acosta et al., Electron, pion and multiparticle detection with a lead / scintillating fiber calorimeter, Nucl.Instrum.Meth. A308, 481 (1991), doi:10.1016/0168-9002(91)90062-U.
- [51] C. Ugur, W. Koening, J. Michel, M. Palka and M. Traxler, *Field programmable gate array based data digitisation with commercial elements*, JINST **8**, C01035 (2013), doi:10.1088/1748-0221/8/01/C01035.
- [52] E. Bayer and M. Traxler, A high-resolution (< 10 ps RMS) 32-Channel Time-to-Digital Converter (TDC) implemented in a Field Programmable Gate Array (FPGA), 17th IEEE-NPSS, Real Time Conference (RT), 24-28 May 2010 (2010).
- [53] M. T. et al., A compact system for high precision time measurements (<14 ps RMS) and integrated data acquisition for a large number of channels, JINST 6, C12004 (2011).
- [54] CMS Collaboration, S. Chatrchyan et al., Performance of the CMS Hadron Calorimeter with Cosmic Ray Muons and LHC Beam Data, JINST 5, T03012 (2010), arXiv:0911.4991, doi: 10.1088/1748-0221/5/03/T03012.
- [55] J. Cvach, *CALICE scintillator hadron calorimeter prototype commissioning and calibration*, Pramana **69**, 1031 (2007), doi:10.1007/s12043-007-0223-1.
- [56] Meerstetter Engineering GmbH, *TEC-1091: Miniature OEM Precision Peltier Temperature Controller*, http://meerstetter.ch/en/products/tec/item/43-tec-1091.
- [57] H. Gaillard *et al.*, *HiRadMat: A New Irradiation Facility for Material Testing at CERN*, Conf.Proc. **C110904**, 1665 (2011).
- [58] Y. Musienko, private communication.

The CBM Collaboration

- Aligarh, India, Department of Physics, Aligarh Muslim University

N. Ahmad, M.D. Azmi, M. Irfan, H. Jahan, M.M. Khan

- Beijing, China, Department of Engineering Physics, Tsinghua University

Jianping Cheng, Zhi Deng, Xinjie Huang, Jin Li, Yuanjing Li, Yulan Li, Yi Wang, Xianglei Zhu

- Bhubaneswar, India, Institute of Physics

D.P. Mahapatra, N.R. Panda, P.K. Sahu

 Bucharest, Romania, Horia Hulubei National Institute of Physics and Nuclear Engineering (IFIN-HH)

C. Andrei, D. Bartoş, I. Berceanu, A. Bercuci, G. Caragheorgheopol, V. Cătănescu, F. Constantin, A. Herghelegiu, M. Petriş, A. Petrovici, M. Petrovici, A. Pop, L. Radulescu, C. Schiaua, M.-G. Târzilă

- Bucharest, Romania, Atomic and Nuclear Physics Department, University of Bucharest
 - D. Argintaru, V. Baban, C. Beşliu, M. Cãlin, V. Covlea, T. Eşanu, A. Jipa, I. Lazanu, C. Ristea, O. Ristea, A. Scurtu
- Budapest, Hungary, Eötvös Loránd University (ELTE)

M. Csanád, Á. Fülöp, A. Kiss

 Budapest, Hungary, Institute for Particle and Nuclear Physics, Wigner Research Centre for Physics, Hungarian Academy of Sciences

T. Kiss, T. Tolyhi, Gy. Wolf

- Chandigarh, India, Department of Physics, Panjab University

M.M. Aggarwal, A.K. Bhati, M. Kaur

- Darmstadt, Germany, Facility for Antiproton and Ion Research in Europe GmbH (FAIR)
 J. Eschke¹, W.F.J. Müller¹
- Darmstadt, Germany, GSI Helmholtzzentrum für Schwerionenforschung GmbH (GSI)

A. Abuhoza^{9,2}, M. Al-Turany, A. Andronic, R. Averbeck, E. Badura, T. Balog, D. Bertini, O. Bertini, S. Chatterji, M.I. Ciobanu¹⁰, H. Deppe, D. Emschermann, H. Flemming, U. Frankenfeld, V. Friese, J. Frühauf, J. Hehner, J.M. Heuser, R. Holzmann, M. Ivanov, R. Karabowicz, M. Kiš, V. Kleipa, K. Koch, P. Koczoń, W. König, B.W. Kolb, D. Kresan, I. Kulakov, J. Kunkel, A. Lebedev³, J. Lehnert, Y. Leifels, S. Löchner, A.M. Marin Garcia, S. Masciocchi, D. Miskowiec, T. Morhardt, W. Niebur, J. Pietraszko, J. Sánchez Rosado, S. Schatral⁴, C.J. Schmidt, K. Schweda, S. Seddiki, I. Selyuzhenkov, A. Senger, P. Senger², C. Simons, I. Sorokin⁵, D. Soyk, C. Sturm, A. Toia², F. Uhlig, I. Vassiliev, R. Visinka, N. Winckler, P. Zumbruch, M. Zyzak

- Darmstadt, Germany, Institut f
 ür Kernphysik, Technische Universit
 ät Darmstadt
 - T. Galatyuk¹, A. Rost, F. Seck
- Dresden, Germany, Institut für Strahlenphysik, Helmholtz-Zentrum Dresden-Rossendorf (HZDR)

Xingming Fan, K. Heidel, B. Kämpfer¹¹, R. Kotte, A. Laso Garcia¹¹, L. Naumann, C. Wendisch, J. Wüstenfeld

Dubna, Russia, Laboratory of Information Technologies, Joint Institute for Nuclear Research (JINR-LIT)

T. Ablyazimov, P. Akishin, E. Akishina, T. Akishina, E. Alexandrov, I. Alexandrov, O. Derenovskaya, I. Filozova, Valery Ivanov, Victor Ivanov, P. Kisel, G. Kozlov, G. Ososkov, A. Raportirenko, P. Zrelov

Dubna, Russia, Veksler and Baldin Laboratory of High Energy Physics, Joint Institute for Nuclear Research (JINR-VBLHEP)

Yu. Anisimov, S. Avdeev, M. Baznat, A. Bychkov, V. Chepurnov, S. Chernenko, K. Davkov, V. Davkov, D. Dementiev, S. Dubnichka, A. Dubnichkova, O. Fateev, V. Golovatyuk, K. Gudima, Yu. Gusakov, A. Ierusalimov, E.-M. Ilgenfritz, V. Karnaukhov, G. Kekelidze, A. Khvorostukhin, V. Kirakosyan, P. Kurilkin, V. Ladygin, A. Malakhov, V. Mialkovski, Yu. Murin, S. Parzhitskiy, D. Peshekhonov, V. Peshekhonov, E. Plekhanov, S. Razin, A. Shabunov, N. Shumeiko, I. Tsakov, B. Yuldashev, Yu. Zanevsky, A. Zinchenko, V. Zryuev

Frankfurt, Germany, Frankfurt Institute for Advanced Studies, Goethe Universität Frankfurt (FIAS)

V. Akishina^{3,1}, M. Bach, J. de Cuveland, D. Eschweiler, S. Gorbunov, H. Hartmann, D. Hutter, E. Iakovleva, I. Kisel, M. Kretz, V. Lindenstruth¹, V. Vovchenko

- Frankfurt, Germany, Institut für Kernphysik, Goethe Universität Frankfurt

S. Amar-Youcef, H. Appelshäuser, A. Arend, T. Balle, C. Blume, H. Büsching, M. Deveaux, P. Dillenseger, D. Doering, I. Fröhlich, P. Ghosh¹, S. Gläßel, P. Klaus, M. Koziel, E. Krebs, G. Kretschmar, P. Larionov¹, Qiyan Li⁶, B. Linnik, H. Malygina^{5,1}, J. Markert, J. Michel, B. Milanović, C. Müntz, M. Penschuck, J. Pieper, P. Reichelt, F. Roether, P. Sitzmann, S. Strohauer, J. Stroth¹, M. Tanha, T. Tischler, M. Wiebusch

- Frankfurt, Germany, Institute for Computer Science, Goethe Universität Frankfurt

S. Böttger, T. Breitner, H. Engel, C. García Chávez, J. Gebelein, A. Gómez Ramírez, T. Janson, U. Kebschull, C. Lara, J. Lehrbach, J.A. Lucio Martínez, S. Manz, A. Oancea

- Gatchina, Russia, Petersburg Nuclear Physics Institute, NRC Kurchatov Institute (PNPI)

V. Baublis, V. Dobyrn, V. Golovtsov, Vladimir Ivanov, A. Khanzadeev, L. Kochenda, B. Komkov, P. Kravtsov, E. Kryshen, L. Kudin, N. Miftakhov, V. Nikulin, E. Rostchin, Yu. Ryabov, V. Samsonov, O. Tarassenkova, S. Volkov, E. Vznuzdaev, M. Vznuzdaev, M. Zhalov

- Gießen, Germany, Justus-Liebig-Universität Gießen

J. Bendarouach, C.A. Deveaux, M. Dürr, C. Höhne, S. Lebedev³, E. Lebedeva, T. Mahmoud

- Guwahati, India, Department of Physics, Gauhati University

B. Bhattacharjee, B. Debnath, K. Dey, R. Talukdar

Hefei, China, Department of Modern Physics, University of Science & Technology of China (USTC)

Ping Cao, Hongfang Chen, Huanhuan Fan⁷, Cheng Li, Ming Shao, Yongjie Sun, Zebo Tang, Yifei Zhang

- Heidelberg, Germany, Physikalisches Institut, Universität Heidelberg

I. Deppner, D. Gottschalk, N. Herrmann, Tae Im Kang, P.-A. Loizeau, C. Simon, Ya Peng Zhang

Heidelberg, Germany, Zentrales Institut für Technische Informatik, Universität Heidelberg, Standort Mannheim

U. Brüning, P. Fischer, C. Kreidl, M. Krieger, F. Lemke, I. Peric, D. Wohlfeld

- Indore, India, Indian Institute of Technology Indore

R. Sahoo

- Jaipur, India, Physics Department, University of Rajasthan

R. Raniwala, S. Raniwala

- Jammu, India, Department of Physics, University of Jammu

A. Bhasin, A. Gupta, S. Mahajan, B.V.K.S. Potukuchi, S.S. Sambyal, M.K. Sharma

- Karlsruhe, Germany, Karlsruhe Institute of Technology (KIT)

S. Bähr, M. Balzer, J. Becker, T. Blank, M. Dreschmann, L. Meder, J. Meyer, O. Sander, M. Weber

- Katowice, Poland, Institute of Physics, University of Silesia

A. Bubak, A. Grzeszczuk, E. Kaptur, S. Kowalski, K. Schmidt, W. Zipper

Kharagpur, India, Indian Institute of Technology Kharagpur

P. Banerjee, T.K. Bhattacharyya, A. Haldar, S. Haldar, A.K. Singh, I. Som

Kolkata, India, Department of Physics, Bose Institute

R. Adak, S. Das, S.K. Ghosh, S. Raha, R. Ray, S. Samanta

Kolkata, India, Department of Physics and Department of Electronic Science, University of Calcutta

S. Bandyopadhyay, A. Bhattacharyya, A. Chakrabarti, Sanatan Chattopadhyay, G. Gangopadhyay, S. Sau

- Kolkata, India, Variable Energy Cyclotron Centre (VECC)

Z. Ahammed, P.P. Bhaduri, Subhasis Chattopadhyay, M. Dey, A.K. Dubey, V. Jain, S.A. Khan,

S. Mandal, E. Nandy, T. Nayak, S. Pal, A. Roy, J. Saini, R.N. Singaraju, V. Singhal, Y.P. Viyogi

Kraków, Poland, AGH University of Science and Technology (AGH)

M. Baszczyk, A. Drozd, J. Gajda, P. Gryboś, K. Kasiński, R. Kłeczek, P. Kmon, W. Kucewicz, P. Maj, P. Otfinowski, J. Rauza, R. Szczygieł, M. Żoładź

Kraków, Poland, Marian Smoluchowski Institute of Physics, Jagiellonian University

M. Adamczyk, T. Barczyk, J. Brzychczyk, L. Dutka, Z. Majka, R. Najman, R. Płaneta, Z. Sosin, P. Staszel, A. Wieloch

Kviv, Ukraine, High Energy Physics Department, Kiev Institute for Nuclear Research (KINR)

M. Borysova, A. Kovalchuk, V. Kyva, V. Militsija, I. Panasenko, M. Pugach, V. Pugatch, D. Storozhyk

Kyiv, Ukraine, Department of Nuclear Physics, National Taras Shevchenko University of Kyiv

O. Bezshyyko, L. Golinka-Bezshyyko, I. Kadenko, Y. Onishchuk, V. Plujko

- Moscow, Russia, Institute for Nuclear Research (INR)

O. Andreeva, D. Finogeev, M. Golubeva, F. Guber, A. Ivashkin, O. Karavichev, T. Karavicheva, E. Karpechev, A. Kurepin, A. Maevskaya, O. Petukhov, I. Pshenichnov, A. Reshetin, A. Sadovsky, N. Topil'skaya, E. Usenko

Moscow, Russia, Institute for Theoretical and Experimental Physics (ITEP)

A. Akindinov, S. Belogurov, A. Chernogorov, D. Golubkov, F. Khasanov, S. Kiselev, A. Kolosova, I. Korolko, D. Malkevich, K. Mikhailov, A. Nedosekin, E. Ovcharenko, V. Plotnikov, M. Prokudin, I. Rostovtseva, A. Semennikov, R. Sultanov, Yu. Zaitsev

- Moscow, Russia, National Research Nuclear University MEPhI

E. Atkin, Yu. Bocharov, E. Malankin, O. Malyatina, D. Normanov, D. Osipov, A. Petrovskiy, V. Shumikhin, A. Simakov, M. Strikhanov

- Moscow, Russia, National Research Centre "Kurchatov Institute"

D. Blau, A. Kazantsev, V. Manko, I. Yushmanov

Moscow, Russia, Skobeltsyn Institute of Nuclear Physics, Lomonosov Moscow State University (SINP-MSU)

N. Baranova, D. Karmanov, M. Korolev, M. Merkin, V. Popov, A. Voronin

- Münster, Germany, Institut für Kernphysik, Westfälische Wilhelms Universität Münster

R. Berendes, C. Bergmann, N. Heine, Ch. Klein-Bösing, M. Kohn, W. Verhoeven, J.P. Wessels

- Obninsk, Russia, National Research Nuclear University

N. D'Ascenzo, A. Galkin, D. Ossetski, V. Saveliev

- Prague, Czech Republic, Czech Technical University (CTU)

V. Petráček, V. Pospisil, L. Škoda

- Protvino, Russia, Institute for High Energy Physics (IHEP)

S. Golovnya, S. Gorokhov, A. Kiryakov, I. Lobanov, E. Lobanova, V. Rykalin, S. Sadovsky, Yu. Tsyupa, A. Vorobiev

- Pusan, Korea, Pusan National University (PNU)

Kyung-Eon Choi, Jongsik Eum, Sanguk Won, Jun-Gyu Yi, In-Kwon Yoo

Řež, Czech Republic, Nuclear Physics Institute, Academy of Sciences of the Czech Republic

A. Kugler, V. Kushpil, V. Mikhaylov, O. Svoboda, P. Tlustý

- Split, Croatia, University of Split

M. Anđelić, I. Carević, M. Dželalija

- Srinagar, India, Department of Physics, University of Kashmir

F. Ahmad, S. Ahmad, S. Bashir, M.F. Mir, W. Raja

- St. Petersburg, Russia, Ioffe Physico-Technical Institute, Russian Academy of Sciences

V. Eremin, E. Verbitskaya

- St. Petersburg, Russia, V.G. Khlopin Radium Institute (KRI)

O. Batenkov, V. Jakovlev, V. Kalinin, A. Veshikov

- St. Petersburg, Russia, St. Petersburg State Polytechnic University (SPbSPU)
 - A. Berdnikov, Y. Berdnikov
- Strasbourg, France, Institut Pluridisciplinaire Hubert Curien (IPHC), IN2P3-CNRS and Université de Strasbourg
 - G. Claus, A. Dorokhov, M. Goffe, A. Himmi, K. Jaaskelainen, F. Rami, I. Valin, M. Winter
- Tübingen, Germany, Physikalisches Institut, Eberhard Karls Universität Tübingen
 E. Friske, B. Heß, E. Lavrik, A. Lymanets⁵, H.R. Schmidt, J. Wiechula
- Varanasi, India, Department of Physics, Banaras Hindu University
 A. Prakash, B.K. Singh, C.P. Singh
- Warsaw, Poland, Institute of Electronic Systems, Warsaw University of Technology
 A. Byszuk, G. Kasprowicz, J. Pluta, K. Poźniak⁸, R. Romaniuk, D. Wielanek, W. Zabołotny⁸
- Warsaw, Poland, Institute of Experimental Physics, University of Warsaw
 M. Kirejczyk, T. Matulewicz, K. Piasecki, J. Rożynek, B. Sikora, K. Siwek-Wilczyńska, I. Skwira-Chalot, J. Tarasiuk, A. Turowiecki, K. Wiśniewski
- Wuhan, China, College of Physical Science and Technology, Central China Normal University (CCNU)

Xu Cai, Guangming Huang, Feng Liu, Dong Wang, Yaping Wang, Changzhou Xiang, Nu Xu, Zhongbao Yin, Daicui Zhou

Wuppertal, Germany, Fachbereich Physik, Bergische Universität Wuppertal
 K.-H. Becker, K.-H. Kampert, J.M. Kopfer, C. Pauly, J. Pouryamout, S. Querchfeld, J. Rautenberg,
 S. Reinecke

Additional affiliations:

- ¹ GSI Helmholtzzentrum für Schwerionenforschung GmbH (GSI), Darmstadt, Germany
- ² Institut für Kernphysik, Goethe Universität Frankfurt, Frankfurt, Germany
- ³ Laboratory of Information Technologies, Joint Institute for Nuclear Research (JINR-LIT), Dubna, Russia
- ⁴ Zentrales Institut für Technische Informatik, Universität Heidelberg, Standort Mannheim, Heidelberg, Germany
- ⁵ High Energy Physics Department, Kiev Institute for Nuclear Research (KINR), Kyiv, Ukraine
- ⁶ College of Physical Science and Technology, Central China Normal University (CCNU), Wuhan, China
- ⁷ Physikalisches Institut, Universität Heidelberg, Heidelberg, Germany
- ⁸ Institute of Experimental Physics, University of Warsaw, Warsaw, Poland
- ⁹ also: King Abdulaziz City for Science and Technology (KACST), Riyadh, Saudi Arabia
- ¹⁰ also: Institute of Space Science, Bucharest, Romania
- ¹¹ also: Technische Universität Dresden, Dresden, Germany